Investigating Biomolecular Interactions using Terahertz Pulsed Spectroscopy

SUN, Yiwen

A Thesis Submitted in Partial Fulfillment
of the Requirements for the Degree of
Doctor of Philosophy
in
Electronic Engineering

The Chinese University of Hong Kong
August 2010

Abstract of thesis entitled:

Investigating Biomolecular Interactions using Terahertz Pulsed Spectroscopy

Submitted by **SUN, Yiwen**

Supervised by **Prof. Emma Macpherson, Prof. Yuanting Zhang**

for the degree of Doctor of Philosophy

at The Chinese University of Hong Kong in June 2010.

The bio-molecular interaction has been one of the most challenging subjects to probe due to its complexity. In the thesis, we have been attempting to answer fundamental questions about bio-molecular interactions in the terahertz (THz) region from the macroscopic to microscopic level. Terahertz radiation (defined as 0.1-10 THz) can excite intermolecular interactions such as the librational and vibrational modes. These attributes make it feasible to probe the dynamic characteristics of the bio-molecular system. Furthermore, it is worth investigating whether terahertz technology could potentially be used as a novel tool in the biomedical diagnosis field in the near future.

We develop a controlled study to investigate the effects of formalin fixing on the THz properties of two different tissue types. The optical properties are measured using THz reflection spectroscopy. The results present how the fixing process can affect image contrast in THz images of biological samples.

Secondly, we focus our aims on investigating protein molecules due to the possibility of being able to explain the mechanism of molecular interactions more clearly. Two kinds of labeled immunoglobulin G were investigated using a reflective THz-TDS system. The dielectric properties were sensitive to the conjugation of the antibody. Additionally, terahertz spectroscopy is able to evaluate the depth of the hydrogen shell and shows that the hydrogen-bonded networks of charged protein solutions play an important role in determining the dielectric.

Thirdly, using a transmission THz-TDS system we investigated a biomarker protein and observed distinct spectral differences at various temperatures. This work demonstrates that terahertz spectroscopy can be used to evaluate the anharmonicity of the vibrational potential. By comparing the absorption spectra of the THz-TDS and Synchrotron results it is possible to deduce the approximate localization of the vibrational modes within the molecular chain.

Finally, based on theoretical calculations and experiments, we present a development model (DDRA model) to describe the interaction between the protein and its solvent molecule. The parameters derived from this model provide good fits to the experimentally determined complex dielectric constant, making it of the model valuable benchmarks for other theoretical treatments of bio-molecular system.

Abstract of thesis entitled:

Investigating Biomolecular Interactions using Terahertz Pulsed Spectroscopy

Submitted by **SUN, Yiwen**

for the degree of Doctor of Philosophy

at The Chinese University of Hong Kong in June 2010.

Abstract

Bio-molecular interactions are one of the most challenging subjects to probe due to their complexity. In the thesis, we have been attempting to answer fundamental questions about bio-molecular interactions in the terahertz (THz) region from the macroscopic to microscopic level. Terahertz radiation (defined as 0.1-10 THz) lies between the microwave and infrared regions can excite intermolecular interactions such as the librational and vibrational modes. These attributes make it feasible to probe the dynamic characteristics of the bio-molecular system. Furthermore, it is worth investigating whether terahertz technology could potentially be used as a novel tool in the biomedical diagnosis field in the near future.

Several THz studies of freshly excised tissue have highlighted the sensitivity of THz imaging to biological tissues. However, it is not always possible to obtain fresh samples for a study; the most common preservation technique is formalin fixing. Along with sample variability, the sample distortion caused by formalin fixing can present a significant challenge. In this thesis we develop a controlled study to investigate the effects of formalin fixing on the THz properties of two different tissue types. The optical properties of fresh and formalin-fixed samples are measured using THz reflection spectroscopy. The results are compared, and we discuss how the fixing process can affect image contrast in THz images of biological samples. Secondly, we focus our aims on investigating protein molecules due to the possibility of being able to explain the mechanism of molecular interactions more clearly. In this thesis, two kinds of labeled immunoglobulin G were investigated using a reflective THz-TDS system. The dielectric properties of each solution containing an antibody were sensitive to the conjugation of the antibody. Additionally, through consideration of the hydrogen dynamic effects of the antibody at terahertz frequencies, terahertz spectroscopy is able to evaluate the depth of the hydrogen shell for each antibody. This work shows that the hydrogen-bonded networks of charged protein solutions play an important role in determining the dielectric properties as detected by terahertz spectroscopy.

Thirdly, using a transmission THz-TDS system we investigated a biomarker protein (HER2) and observed distinct spectral differences at temperature from 15 K to 294 K. This work demonstrates that terahertz spectroscopy can be used to evaluate the anharmonicity of the vibrational potential which relates to the strength of the reset force of the oscillating system. Important parameters relating to the dynamics of the molecules' low frequency relaxation motion can be extracted using a simple model. By comparing the absorption spectra of the THz-TDS and Synchrotron results it is possible to deduce the approximate localization of the different vibrational modes within the molecular chain.

Finally, based on theoretical calculations and experiments, we present a development model (DDRA model) to describe the interaction between the protein and its solvent molecule. The parameters derived from this model provide good fits to the experimentally determined complex dielectric constant, making the frequency-dependent dielectric constants of the model valuable benchmarks for molecular dynamics simulations and other theoretical treatments of bio-molecular system.

摘要

研究生物分子間的相互作用已成為目前極具挑戰性的課題之一。太赫兹(THz)技術是近年來發展起來的一個新型交叉前沿領域，其重要學術價值已得到國際科學界公認。THz波是一種介於遠紅外和微波之間的電磁波譜，太赫兹射線可以無電離的激發分子間振動或轉動模式，這些特質使得THz波非常適合用於研究生物分子之間的動態特徵。本論文致力於從宏觀到微觀角度，研究生物分子在太赫兹頻率下相互作用的特點，為將來把太赫兹技術用於實際臨床診斷領域提供理論及實驗數據依據。

在臨床診斷中，為保持組織的形態特徵，樣品往往經過固定才用於組織學檢測。福爾馬林溶液固定是最常用的方法之一。本文中，我們將利用太赫兹反射成像系統，研究福爾馬林固定對太赫兹輻射下組織樣品的作用，並揭示固定過程對組織太赫兹成像對比的影響。

為進一步了解分子間相互作用的機制，本文利用THz-TDS反射系統，研究了兩種形態相似的抗體蛋白(IgG)在液體環境下的分子動態特性。實驗證明，太赫兹輻射下蛋白質抗體的介電常数對其配體結構十分敏感；太赫兹光譜可揭示出蛋白質分子的水合作用，並可用於蛋白質分子水合層厚度的評估。此項研究還表明，帶電性蛋白質溶液的氫鍵網絡在利用太赫兹光譜測量介電常數的過程中，發揮著極其重要的作用。

此外，利用THz-TDS透射系統，我們對癌症標記蛋白(HER2)進行了一系列研究。通過從15K到室溫的測量，我們得到一系列光譜信息。實驗證明，太赫兹光譜可以用來探測蛋白質分子的非簡諧振動，並揭示了振子間作用力的變化。我們採用經典模型，提取了HER2蛋白在太赫兹頻率下的動態參數，並通過THz-TDS透射系統及同步加速器對蛋白質吸收光譜的測量比較，證實太赫兹輻射可預測分子鏈中不同振動模式在頻譜中的位置。

最後，基於理論計算及實驗數據的對比，我們針對蛋白質分子與其周圍溶劑分子之間的相互作用，提出一種DDRA(Double Debye Resonant Absorption)模型。該模型參數與試驗測量的介電常數相符。模型中基於頻率的介電常數對分子動態模擬及其它生物分子系統理論研究具有較高的參考價值。

Acknowledgments

I would like to take this opportunity to express the immense gratitude to my supervisor, Prof. Emma Pickwell-MacPherson, for the invaluable guidance and support during the year of my PhD study. I am also grateful for her patience and time spent on my thesis and deeply appreciates the opportunity to work under her supervision.

I am also greatly indebted to my supervisor Prof. Yuan-ting Zhang for his guidance and support throughout this study.

There are a number of people to whom I am indebted for their assistance during my PhD study.

I would like to thank Prof. Derek Abbott for a great opportunity supporting to process the collaborative work in his excellent THz laboratory at University of Adelaide. I also thank Dr. Jegathisvaran Balakrishnan, Mr. Benjamin Ung, Mr. Hungyen Lin, Mr. Shaoming Zhu for their huge help in collaboration when I lived at Adelaide and all the colleagues from the University of Adelaide for their kind assistance.

I would extend my appreciation to Dr. Bernd Michael Fischer for his insightful suggestions to my experiment proposal and papers and Dr. Edward Parrott for his aids in thesis modification.

I am also grateful to Dr. Kun Qin at the Department of Microbiology, The University of Hong Kong, for the guidance of sample preparation.

I would like to thank all the colleagues in JCBME, especially Dr. Shengyang Huang, Ms. Kanis Kan, Dr. Yang Chen and Mr. Stanley Sy for their enormous technical support and valued friendship.

Last but not least, I would like to express my gratitude to my parents, Dr. Zexuan Zhu and all my family members for their support.

Contents

List of Figures

List of Tables

Chapter 1

Introduction

Terahertz radiation, also termed THz waves, THz light, or T-rays, is situated in the far infrared range which is one of the least explored ranges of the electromagnetic (EM) spectrum. In 1975, David Auston at AT&T bell Laboratories developed a photoconductive emitter gated with an optical pulse that led towards bridging this gap. This device, known as the "Auston switch", emitted broadband terahertz radiation up to 1 mW [1]. Subsequent improvements in the generation and detection of coherent terahertz radiation enabled terahertz time-domain spectroscopy and imaging techniques to be pioneered for applications in various fields. Now, researchers are able to extensively explore the material interactions occurring in the terahertz spectral region due to the ready availability of the ultrafast pulsed sources and detectors. Arising from its ability to penetrate deep into many organic materials without the damage associated with ionizing radiation, the application of the terahertz radiation in biomedical detection has been attracting an increasing number of investigators. Within this thesis, we do not want to suggest an unrealistic "Utopia" for the improvement of the terahertz technology since it is clear that there is still a long way to go before such a goal may be realised. However, as a relatively new and the advantageous technique, it is worth investigating whether terahertz technology could potentially be used as a novel tool in the biomedical diagnosis field in the near future.

1.1 Terahertz Radiation

Now that the hurdle of generating terahertz radiation has been overcome [2], there is increasing interest in the terahertz (THz = 10^{12} Hz) region which lies between the microwave and infrared regions of the EM spectrum. The terahertz regime is typically defined as ranging from 0.1 to 10 THz in frequency, or 3.33 cm^{-1} to 33.3 cm^{-1} in wavenumbers, and photon energies of 2.0×10^{-22} to 1.3×10^{-20} J [3]. This region has only recently been explored due to a previous lack of appropriate sources and detectors. In fact, it was commonly referred to as the "terahertz gap" before advances in semiconductor physics enabled this so-called gap to be bridged.

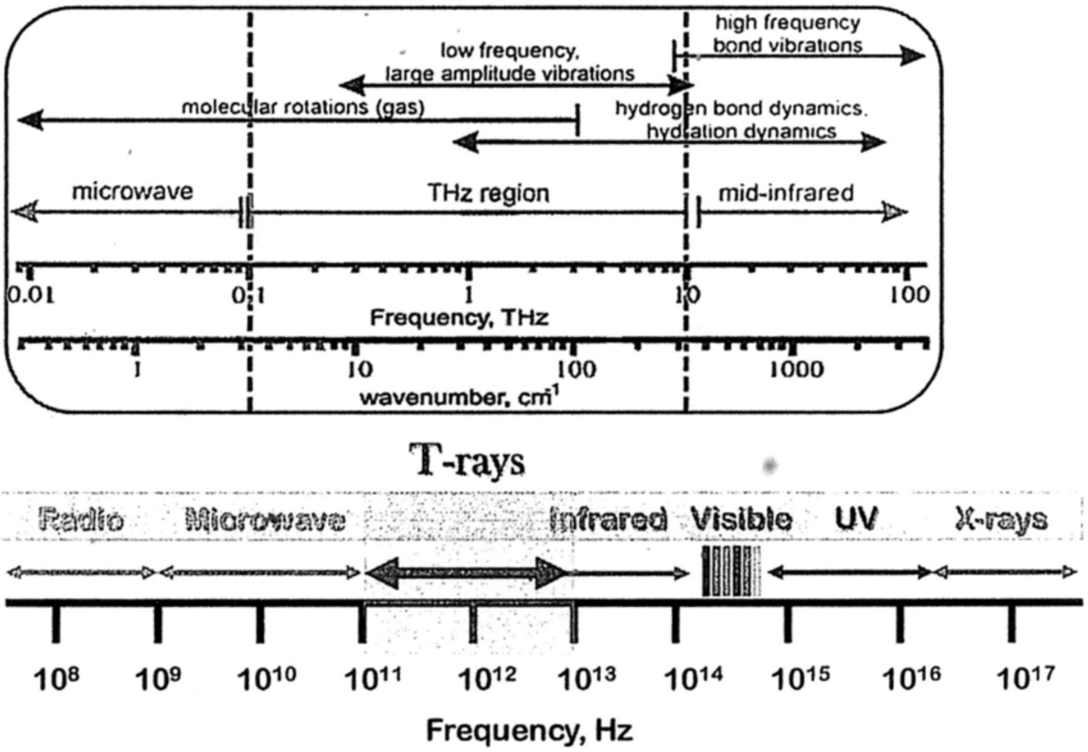

Figure 1.1: The THz region and molecular transitions in the electromagnetic spectrum

On the basis of this recent improvement of the ultrafast pulsed visible and near-infrared lasers, the coherent generation and detection of sub-picosecond, broadband (0.05-10 THz) pulses became possible. This, in turn, stimulated research into the application of terahertz radiation, both as an imaging technique and in spectroscopy. Terahertz technology, because of its unique features, has allowed many fascinating and important applications in modern society to be investigated, e.g., in quality management, security and with special potential applications in medicine and biology [4]. The water content of a material, a frequently considered question in terahertz technology because water displays strong absorption characteristics at terahertz frequencies, is able to show distinctive contrast in medical imaging. In addition, many organic substances have characteristic absorption spectra in this frequency range [5, 6], which is a benefit for the research into spectroscopy for biomedical applications. In this thesis, the interaction of terahertz radiation with both tissues and biological molecules has been investigated.

1.2 Interaction with Molecules in THz Regime

Understanding the interactions between molecules and terahertz radiation also requires an understanding of molecular energy states and an appropriate theoretical framework. The potential energy surfaces of a molecular system are probed by molecular vibrations via a variety of spectroscopic techniques. Of particular interest in the terahertz region, for the typical diatomic polar molecules including atoms with atomic masses less than 20 as an example, the energy separation between two consecutive rotational states ΔE is approximately 1.602×10^{-22} J [7]. ΔE therefore corresponds to a frequency of 0.242 THz, confirming that the absorption of terahertz radiation is likely to produce changes in the rotational states of simple polar diatomic molecules. Bernd Fischer reviewed and showed that the spectral separation between external and internal molecular vibrations is due to the remarkable difference in the strengths of the internal covalent bonds, with energies in the range of 300-400 kJ/mol, and the weak intermolecular forces, e.g., van-der-Waals forces of about 1 kJ/mol. This separation is, however, significantly smaller in ionic crystals composed of polar molecules (electrostatic ion-ion interactions are on the order of 20 kJ/mol) or in hydrogen-bonded substances, where the hydrogen-bonds have typical energies of 10-40 kJ/mol [8].

The frequencies associated with terahertz radiation are associated with a photon description and those which use an electromagnetic wave model to describe interactions with matter. Thus, one approach is to use a classical EM wave description which characterizes the medium in terms of the permittivity ε (the ability of the medium to be polarized) and conductivity σ (the ability of ions to move through the medium). These parameters readily describe interactions with collections of molecules, including water and proteins in macroscopic terms i.e. bulk motions of the molecules (polarization and conduction), rather than microscopic absorption of radiation due to transitions between molecular energy levels [3].

Although the intermolecular modes in the terahertz regime are usually mixed with intramolecular vibrations which obscures spectra and complicates assignment of individual modes, it has the advantage that the spectrum contains not only information about the intermolecular arrangement, but also characteristics related to the internal molecular structure. Such modes usually carry far more structural information than vibrations in the mid-infrared spectral region, which do not depend much on the overall molecular structure and configuration.

1.3 Biomedical Applications of Terahertz Imaging

1.3.1 Medical Imaging

THz radiation is non-ionizing, non-destructive and non-invasive [9, 10]: the low energy of the THz radiation does not damage the sample [11]. One potential application of THz imaging is the diagnosis of skin cancer. Work by Wallace *et al.* has highlighted the potential advantages of being able to use terahertz imaging to study skin cancer *ex vivo* in time-domain by a Terahertz Pulsed Imaging (TPI) system used in reflection geometry [12].The first *in vitro* measurements on skin cancer demonstrating the ability of TPI to differentiate basal cell carcinoma (BCC) from normal skin was produced by Woodward *et al.* [13]. It is promising that the potential of terahertz imaging technology as an *in vivo* tool for the study of skin hydration levels have enabled differentiation between diseased, normal and inflamed tissue [14, 15]. In a similar way to how terahertz imaging could assist the planning of skin cancer surgery, Fitzgerald *et al.* have investigated the use of terahertz imaging to aid the removal of breast cancer intra-operatively [16]. P. Knobloch *et al.* imaged histo-pathological samples including the larynx of a pig and a human liver with metastasis [17]. We have investigated the effects of formalin fixing on the terahertz properties of porcine adipose tissue and muscle (see Chapter 3).

Another potential application of THz imaging is the diagnosis of dental caries [18]. Caries are a result of mineral loss from enamel, and this causes a change in refractive index within the enamel. This change in refractive index means that small lesions, smaller than those detected by the naked eye, can be detected [19].

1.3.2 Pharmaceuticals

Furthermore, there has been a strong drive in the pharmaceutical industry for comprehensive quality assurance monitoring. This move opens the way for new tools providing useful analysis of tablet formulations. The ability of terahertz technology to determine both spectral and structural information has fuelled interest in the pharmaceutical applications of this technique [20]. To date, terahertz radiation has been established for pharmaceutical applications when used as a spectroscopic technique in polymorph identification and quantification [21-23], phase transition monitoring [24, 25], and distinguishing behaviors hydrated forms [26]. Here, we represent our previous investigation on non-invasive tablet inspection using terahertz pulsed imaging.

Terahertz radiation can penetrate through plastic packaging materials. Figure 1.2(c) is a terahertz image of the tablet taken through the packaging - from this

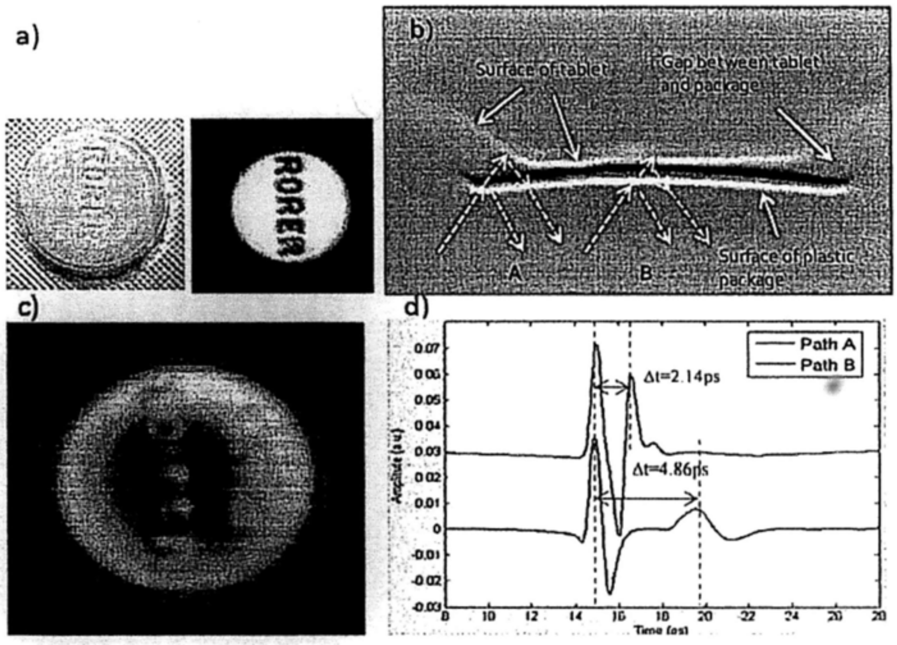

Figure 1.2: (a) The photograph presents the white side and the yellow side of the tablet in the plastic package. (b) Terahertz B-Scan image shows the structure of the cross-section of the tablet and the terahertz light paths at the edge of the tablet (path A) and the centre (path B). (c) Terahertz C-Scan image shows the tablet face. (d) Terahertz deconvolved waveforms in the time-domain reflected from the paths A and B in (b).

image we can see the lettering on the surface of the tablet. The cross-section of the tablet is better conveyed by an image of the depth profile. To obtain this, we take a slice of the image along the *x* axis and plot the pulse intensity on a gray scale. In this way we can see the reflections off the different interfaces at depth (this is similar to an ultrasound B-scan and is illustrated in Figure 1.2(b)). Here we can see the beveled edge of the tablet through the packaging. It is interesting to look at the pulses that make up this image. The pulses reflected off the sample were deconvolved by the reference measurement of the mirror and then filtered using a (Gaussian) band pass filter. In this way we obtained the deconvolved waveforms. Terahertz pulses are reflected first off the front surface of the package and then from any subsurface structure within it resulting in multiple pulses returning to the detector. The dashed arrows in Figure 1.2(b) mark out the terahertz light paths at the edge of the tablet (path A) and the centre (path B). In path A the beveled edge means that there is an air gap between the packaging and the tablet and this corresponds to a greater optical delay between the reflected peaks in the waveforms illustrated in Figure 1.2(d). Thus, terahertz imaging has non-destructively revealed the structure of the tablet through the packaging.

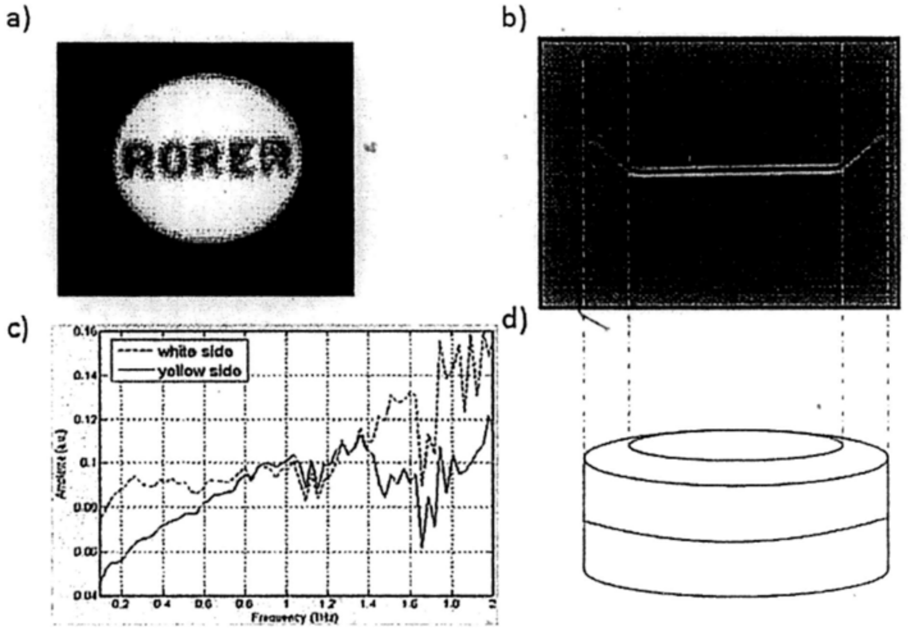

Figure 1.3: (a) Terahertz C-Scan section imaging shows the tablet face without the package. (b) Terahertz B-Scan section imaging shows the structure of the cross-section of the tablet without the package. (c) The frequency domain terahertz spectrum of the each side of a tablet. (d) The geometric structure of the tablet corresponding to the THz B-Scan section imaging (as dash line shown).

The tablet was then removed from the packaging and imaged on both sides. The terahertz image of the "RORER" (yellow) side of the tablet (with no packaging) is presented in Figure 1.3(a). It was formed by using a gray-scale to plot the amplitude of the maximum peak of the reflected terahertz pulse at each pixel. From this image we can clearly see the engraved lettering. In Figure 1.3(b) we show a B-scan of a horizontal slice taken at a height containing the lettering. Since the lettering is engraved the horizontal line is broken in places. The terahertz beam was focused on to the plane of the tablet rather than the engraved lettering. Thus, to extract our spectral information, we use data from pixels which are not involved in the lettering. Figure 1.3(d) shows the frequency domain reflectance terahertz spectrum from each side of the tablet. The spectral amplitude (y in Equation 1.1) is determined by dividing the data from the sample by that of the mirror in the frequency domain:

$$y = \frac{|\mathrm{FFT(sample)}|}{|\mathrm{FFT(reference)}|} \tag{1.1}$$

Terahertz spectroscopy is able to distinguish between polymorphic forms [24], and it is also sensitive to the small variations in a material [27]. From Figure 1.3(c) there are differences between the white side and the yellow side of the tablet at terahertz frequencies: the amplitude of the white side is greater than that of yellow one for all frequencies apart from between 0.8 THz and 1.4 THz. In this frequency range, the amplitudes coincide which is likely to be due to some common component or structure. To interpret the differences observed in Figure 1.3(c), let us consider the molecule structure of the pharmaceutical components of the two sides. Aluminum hydroxide (gibbsite, $Al(OH)_3$) has a typical metal hydroxide structure with hydrogen bonds. It is built up of double layers of hydroxyl groups with aluminum ions occupying two-thirds of the octahedral holes between the two layers [26]. The basic structure of magnesium hydroxide (brucite) forms stacked sheets of octahedrons of magnesium hydroxide ($Mg(OH)_2$) and is closely related to the structure of aluminum hydroxide. However the lower charge in magnesium (+2) as opposed to aluminum (+3) does not require that one third of the octahedrons of a central ion be vacant in order to maintain a neutral sheet. The different symmetry of gibbsite and brucite is due to the different way that the layers are stacked [28]. Terahertz radiation is sensitive to crystalline phonon modes and hydrogen-bond vibrations - it is differences in these aspects which our spectroscopy in Figure 1.3(c) has probed.

1.4 Biomedical Applications of Terahertz Spectroscopy

THz spectroscopy is complementary to THz imaging and is primarily used to determine optical properties in the frequency domain. Since THz pulses are created and detected using short pulsed visible lasers with pulse widths varying from ~ 200 fs down to ~ 10 fs, it is now possible to make time resolved far-infrared studies with sub-picosecond temporal resolution [28]. This was not achievable with conventional far-infrared studies. An important aspect of THz time-domain spectroscopy is that both the phase and amplitude of the spectral components of the pulse are determined. The amplitude and phase are directly related to the absorption coefficient and refractive index of a sample and thus the complex permittivity is obtained without requiring Kramers-Kronig analysis. Furthermore, another advantage of THz spectroscopy is that it is able to non-destructively detect differences because it uses radiation of sufficiently long wavelength and low energy that does not induce any phase changes or photochemical reactions.

THz spectroscopy covers the spectral range from about 0.1-10 THz (3 cm^{-1} to 300 cm^{-1}); this is also known as the far-infrared and extends into the mid-infrared. Since many important chemical and physical processes are associated with energies in terahertz region, there is longstanding interest in THz spectroscopy of the EM spectrum [3]. The simplified treatment of molecular absorption spectra confirms the likelihood of strong absorption lines in the THz region of the spectrum associated with changing vibrational and rotational energy states of polar diatomic molecules. The treatment also suggests that similar relatively simple polar molecules are likely to yield THz absorption spectra and these are indeed observed [29]. Towards the higher frequency end of the terahertz range (from about 1 THz and above) there are vibrational modes corresponding to protein tertiary structural motion; such intermolecular interactions are present in many biomolecules. Other molecular properties that can be probed in the terahertz range include bulk dielectric relaxation modes [29] and phonon modes [30] – these can be difficult to probe using other techniques. For instance nuclear magnetic resonance (NMR) spectroscopy can determine the presence of various carbon bonds, but it cannot be used to distinguish between molecules with the same molecular formula, but with different structural forms (isomers) [31]. Terahertz spectroscopy is able to distinguish between isomers and polymorphs [32] and is therefore emerging as an important and highly sensitive tool to determine biomolecular structure and dynamics [33, 34]. Indeed THz spectroscopy can distinguish between two types of artificial RNA strands when measured in dehydrated form [35]. Furthermore, Fischer *et al.* demonstrated that even when the molecular structure only differs in the orientation of a single hydroxyl group with respect to the ring plane, a pronounced difference in the terahertz spectra is observed [36]. Intermolecular interactions are present in all biomolecules, and since biomolecules are the fundamental components of biological samples, they can be used to provide a natural source of image contrast in biomedical terahertz imaging [37].

The work in this thesis uses time-domain spectroscopy to determine the response of THz radiation to biological materials. We are especially interested in the THz dielectric response of protein solution since it is a major and natural state of biological tissue, and the coherence and sensitivity of THz time-domain spectroscopy make it an ideal analysis tool.

1.5 From Tissue to Protein Spectroscopy

Terahertz radiation can be severely absorbed by biological tissues with high water content. Due to a limited penetration depth in these objects, to date THz applications have been limited to easily accessible parts of the body, for instance, skin, breast tumors and teeth. On the other hand, because THz radiation is readily absorbed by water, it can be used to distinguish between materials with varying water content-for example, adipose tissue versus muscle tissue. These properties lend themselves to applications in process and quality control such as how the fixing process can affect image contrast (see Chapter 3).

Biomolecules, especially proteins, which play an essential structural and catalytic role in cells and tissues often require an aqueous phase in order to be transported to their target sites. In the protein-water system, the characteristic water structure induced near the surfaces of proteins arises not only through hydrogen bonding of the water molecules to available proton donor and proton acceptor sites, but also through electrostatic forces associated with the water molecule that arise from its large electric dipole moment. If an electric field is imposed on such a system of protein-associated water, there will be a torque exerted on each water dipole moment to induce them to attempt to align along the direction of the field vector. A dielectric orientational relaxation time τ can then be defined as the time required for $1/e$ of the field-oriented water molecules to become randomly reoriented on removing the applied field. Measurements may be analysed in terms of the complex dielectric constant $\varepsilon(\omega)$ (where ω denotes angular frequency) or the complex refractive index $\tilde{n}(\omega)$. The degree of orientational polarization and the rate of reorientational relaxation depend on how the water dipoles are influenced by local electrostatic forces and the extent to which the breaking and/or reforming of local hydrogen bonds is required to accommodate the orientational changes. Relaxations of polar side-groups, vibrations of the polypeptide backbone, and fluctuating proton transfer between ionized side-groups of the protein also contribute to the overall polarizability of the protein-water system. If dielectric measurements are made on protein solutions, then orientational relaxations of the protein molecule itself will also be observed [38].

1.6 Overview of Thesis

This thesis is organised in the following way: In **Chapter 1** the basic introduction of terahertz knowledge is reviewed which highlights the potential application of the terahertz technology within the biomedical field. **Chapter 2** outlines the terahertz theoretical and technical concepts employed in this study.

In the following four chapters we give a broad overview of the capabilities and potentials of terahertz spectroscopy of biomolecules from the macroscopic (tissue) to the microscopic (protein) and from the reflective geometry to transmission geometry. In **Chapter 3** a controlled study to investigate the effects of formalin fixing on the terahertz properties of two different tissue types (porcine adipose tissue and muscle) is given. The optical properties of fresh and formalin fixed samples in the terahertz frequency range were measured using THz reflection spectroscopy. The results are compared and we discuss how the fixing process can affect image contrast in terahertz images of biological samples. Considering that proteins are essential to the structure and function of living organisms, in **Chapters 4** and **5**, modified THz-TDS reflection and transmission systems were used to extend our interest from the macroscopic tissue to the microscopic protein. All of the proteins we selected in this study have a critical significance for the diagnosis of disease, and our aim is to understand the interactional properties of these proteins in terahertz radiation, which is an important step towards biomedical detection using terahertz technology. In **Chapter 6**, we will further discuss the simulation model based on Debye theory to describe the dielectric property of protein dissolved in aqueous solution. Finally, **Chapter 7** makes conclusions and and proposes possible further work for dissertation.

Chapter 2

Experimental Setup and Analysis Techniques

The aim of this chapter is to introduce the mathematical techniques accompanying different measurement geometries that will be implemented and referred to in subsequent chapters.

2.1 Refraction and Absorption in the Terahertz Range

The interaction between an electromagnetic wave and an optical medium in which it propagates through can be revealed by the optical parameters of the medium. Absorption occurs when the light frequency is resonant with transition frequencies of the electrons, atoms or molecules in the medium. In the case of terahertz radiation with photon energies in the meV range, the relevant transitions are the molecular rotations for gas, crystalline photon vibrations for solid and hydrogen-bonding stretches and torsions for gas and liquids [19]. The resonant photons are absorbed, transferring their energy into the excitation of higher energy levels of the system. As the consequent of the energy conservation, the light beam will be successively attenuated while propagating through the medium [39]. This attenuation of light is quantified by its absorption coefficient α. This is defined as the fraction of power in a unit length of a medium. If the beam is assumed to propagate in the z direction,

$I(z)$ is the intensity at position z. Then the decrease of the intensity in an incremental slice of thickness dz is given by:

$$dI = -\alpha dz \cdot I(z) \qquad (2.1).$$

This expression can be integrated to the well known Beer's law:

$$I(z) = I_0 \cdot e^{-\alpha z} \qquad (2.2).$$

The refractive index is due to the reduction of the phase-velocity of the light wave and assigned as the ratio of the velocity of light in free space c to the velocity of light in the medium v. Of note, a direct measurement of the refractive index involves measuring the relative phases of the incident and transmitted light waves. Spectroscopic methods, such as THz-TDS in a transmission geometry, which use phase-sensitive detection schemes, directly determine the relative phases of the terahertz radiation. As a result the refractive index can be calculated in a simple fashion (for details see Section 2.2).

The absorption and refractive index can be described by a single parameter, the complex refractive index $\tilde{n}$, defined by

$$\tilde{n} = n - i\kappa \qquad (2.3).$$

Here n is the real refractive index and κ is the extinction coefficient. The parameter κ is related to the absorption coefficient when considering an electric plane wave of a light beam to propagate in x-direction through a medium with refractive index n. The wave vector is given by

$$k = \frac{2\pi}{\lambda/\tilde{n}} = \frac{\tilde{n}\omega}{c} = (n - i\kappa)\frac{\omega}{c} \qquad (2.4)$$

Note that both parameters of absorption and refractive index are a function of frequency. Alternatively the optical properties of a medium are often expressed by the complex dielectric function. The dielectric constant is simply the square of the complex refractive index, where

$$\begin{aligned}\varepsilon(\omega) = \varepsilon'(\omega) - i\varepsilon''(\omega) &= (n(\omega) - i\kappa(\omega))^2 \\ &= n^2 - (\frac{c\alpha}{2\omega})^2 - 2in(\frac{c\alpha}{2\omega})\end{aligned} \quad (2.5).$$

Conversion between refractive index and dielectric constant is done by:

$$\varepsilon'(\omega) = n^2 - \kappa^2 = n^2 - (\frac{c\alpha}{2\omega})^2 \quad (2.6)$$

$$\varepsilon''(\omega) = 2n\kappa = 2n(\frac{c\alpha}{2\omega}) \quad (2.7)$$

thus n and α can be used to express $\varepsilon'(\omega)$ and $\varepsilon''(\omega)$.

2.2 Terahertz Setup in Reflection Geometry

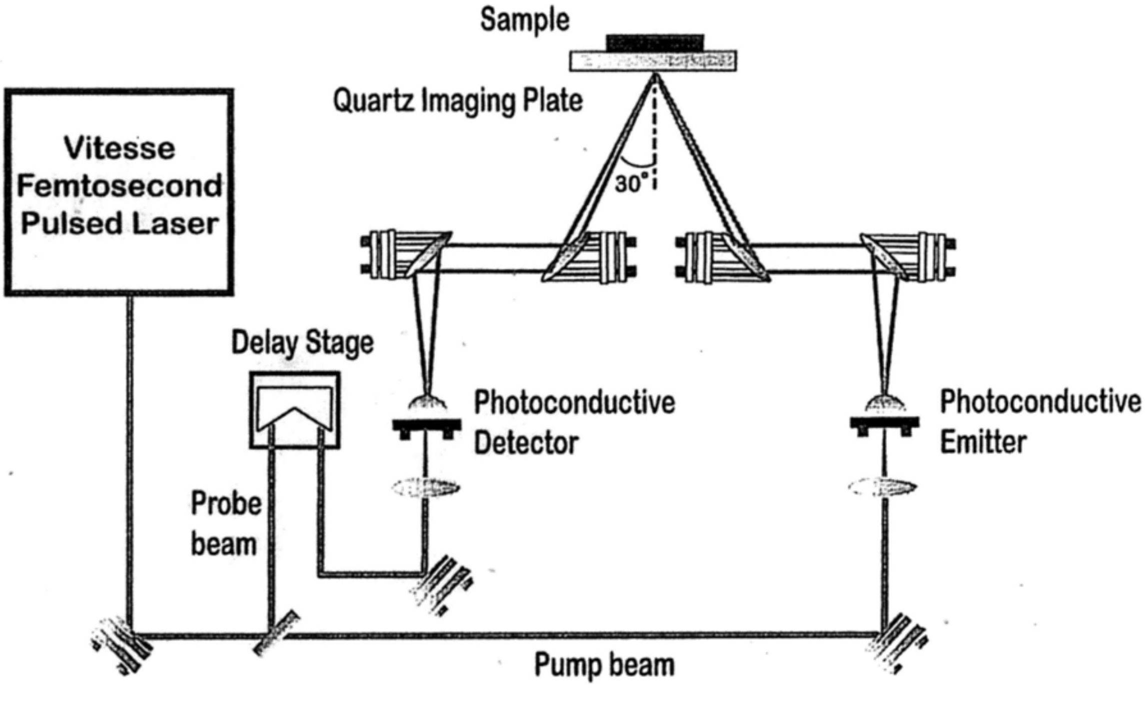

Figure 2.1: Schematic diagram of a terahertz pulsed imaging system TPI^{TM} in reflection geometry.

The Terahertz Pulsed Imaging (TPI^{TM}) system used in this study was the TPI Imaga 1000^{TM} (TeraView Limited, Cambridge, UK). The system uses photoconductive devices to generate and detect terahertz light: the optical excitation is achieved by an 800 nm femtosecond pulsed laser. The system has a reflective geometry (Figure 2.1), such that the laser beam is separated into the pump and probe beams by a beam splitter. The pump beam is directed to excite the carriers in the photoconductive emitter in order to generate terahertz pulses. The terahertz pulses are collimated and focused using off axis parabolic mirrors onto the top surface of a z-cut 2 mm thick quartz window with an angle of incidence of 30°. The sample is placed on the quartz window and the reflected terahertz pulse from the quartz/sample interface is detected coherently by a photoconductive receiver.

In this system, the relaxation of the excited carriers produces broadband electromagnetic pulses typically with a FWHM of 0.3 ps and results in a usable frequency range from about 0.1 THz to 3 THz with an average power of approximately 1μW. The terahertz beam path was purged with nitrogen gas to remove water vapor from the air which would otherwise have attenuated the signal [40]. Detailed information about the system can be found in our previous work [19,41,42].

2.3 Hand-held TPI Setup

The hand-held TPI system is a reflection geometry using a modified version of the TPI Imaga 1000^{TM} (TeraView Limited, Cambridge, UK). The similar optical set up has been described in the Section 2.2. Briefly, this system also uses photoconductive antennas for generation and detection of terahertz radiation, an ultrafast laser (Vitesse, Coherent Inc.) emits 90 fs pulses centered at a wavelength of 800 nm, with a 80 MHz repetition rate and an average power of about 200 mW. The laser beam is separated into the pump and probe beams by a beam splitter, but in contrast to the TPI Imaga 1000^{TM}, the laser in this system used for optical excitation reaches the antennas via a fiber optic, rather than through free space optics. The probe is used to contact the liquid sample directly with an angle of incidence of 3.4° and the reflected terahertz pulse from the quartz/sample interface is detected coherently. The THz beam is scanned up and down across the center line of the window to form a line scanning. The scanning motion is achieved by controlling a Risley prism beam steering system, which includes a pair of Risley prisms and a set of motors and bearings as seen in the Figure 2.2(b & c) [35]. Consider the case of only one wedge prism, when the prism rotates, the steering beam travels in a circle along the optical axis. When two wedge prisms aligned and rotated together, the output beam is the superposition of the circles resulted from two prisms rotating independently. Hence, by matching wedge prisms with different wedge angles and controlling the rotating speed of the two prisms, the steering beam would result in different scanning patterns.

In the case of our probe, a line scanning pattern is achieved by rotating the two prisms with the same wedge angles in opposite direction, given the initial orientations are identical for two prisms. The scan speed of the system is up to 8 lines per second. The scan length is 7 mm and each line contains at most 25 pulses, so it means at most 200 pulses per second. On average, the signal to noise ratio on the receiver of the system is 800:1 (~1000:1 at 1 THz). The usable frequency range is from about 0.1 THz to 1.6 THz but the valid range tends to decrease when the sample is in an aqueous phase due to signal attenuation by the sample.

Terahertz spectroscopy is typically done with an average point measurement of a homogenous sample and the resulting terahertz electric field can be recorded as a function of time. A fast Fourier transform of the temporal profiles was performed to offer meaningful spectroscopic information due to the broadband nature of pulsed THz radiation. We used a measurement of air as a reference. The complex spectrum $E_{ref}(\omega)$ of the reference THz pulse is related to the complex spectrum $E_{sam}(\omega)$ of the output THz pulse, Thus we can determine $\alpha(\omega)$ and $n(\omega)$ for the sample. The details have been indicated in next section.

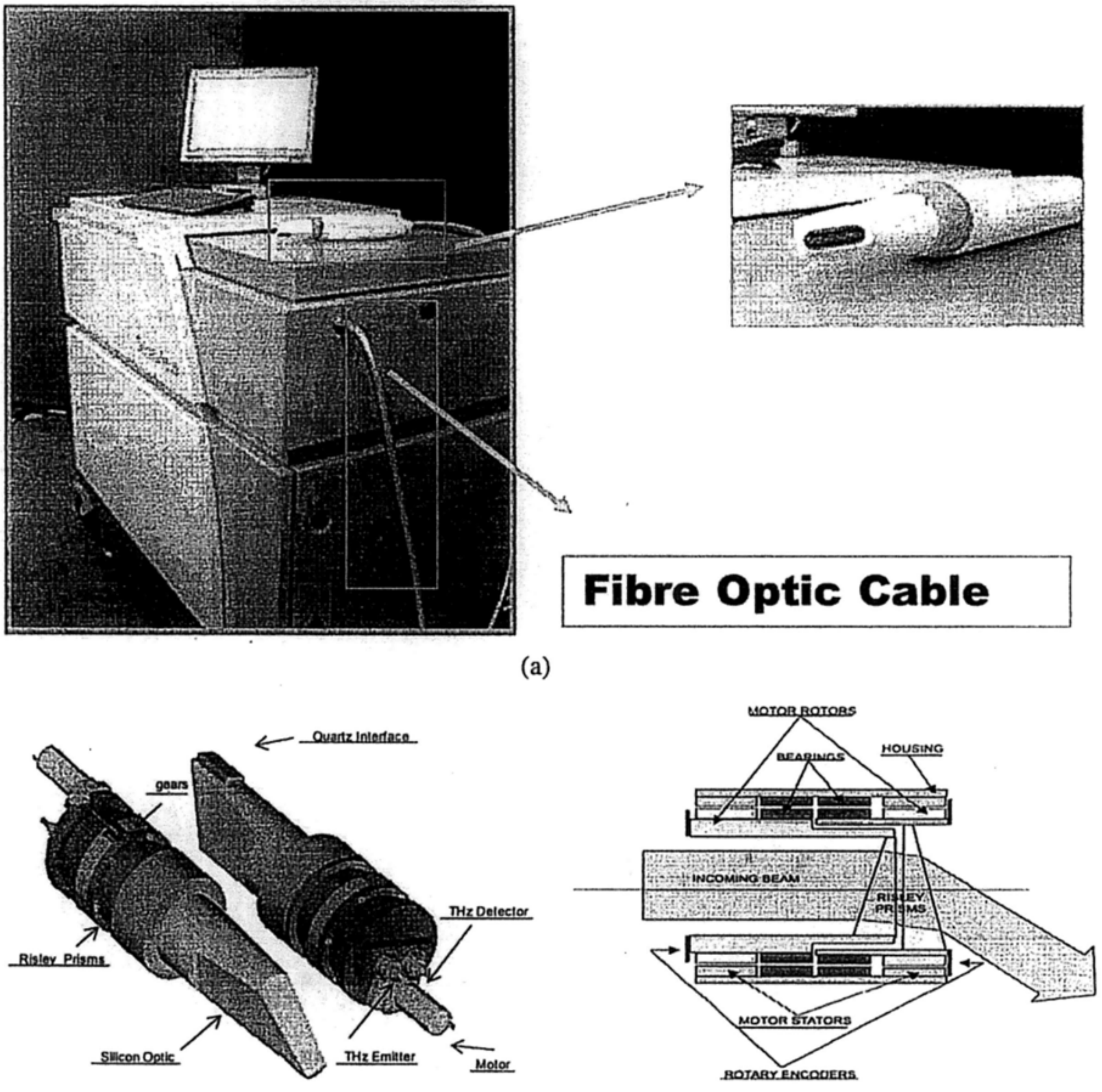

(a)

(b)

(c)

Figure 2.2: Pictures of the (a) THz reflection hand-held probe systems; (b) Schematic diagram of the probe head internal setup (from Teraview^{TM}); (c) Schematic diagram of the risley prism beam steering system embedding in the probe.

2.4 Data Analysis in Reflective Geometry

The spectroscopic data shown in Chapter 3&4 was obtained by using the THz time-domain spectrometer setup in reflective geometry. THz pulse is reflected off a sample interface before the THz waves enter the sample. In real materials, the polarization does not respond instantaneously to an applied field. This causes dielectric loss, which can be expressed by a permittivity that is both complex and frequency dependent. A complex index of refraction can be defined such as Equation 2.8. Here, n is the refractive index indicating the phase speed, while κ is called the extinction coefficient correlate with the absorption coefficient α, which indicates the amount of absorption loss when the electromagnetic wave propagates through the material, c is the speed of light in a vacuum

$$\tilde{n}(\omega) = n(\omega) - i\kappa(\omega) = n(\omega) - i(\frac{c\alpha(\omega)}{2\omega}) \qquad (2.8).$$

In this study, the complex refractive index of a sample can be acquired through consideration of Fresnel's coefficient in a reflection geometry. When terahertz waves are collimated to the sample, different angles of incidence may be used. The complex reflectivity R is defined as

$$R = \frac{E_2}{E_1} = \frac{\tilde{n}_1 \cos\theta_1 - \tilde{n}_2 \cos\theta_2}{\tilde{n}_1 \cos\theta_1 + \tilde{n}_2 \cos\theta_2} \qquad (2.9)$$

where E_1 is the incident light, θ_1 is the angle of incidence; E_2 is the measured reflectance spectrum from the sample, θ_2 is the angle of refraction.

As the incident light is unknown, a reference measurement R^{ref} using known refractive index and absorption coefficient must be taken firstly. Here, the quartz with a refractive index around 2.12 and the air with a refractive index of 1 is used as a reference for the calculation of $\tilde{n}_{\text{sample}}$.

$$R^{\text{ref}} = \frac{E_2^{\text{ref}}}{E_1^{\text{ref}}} \qquad (2.10)$$

$$R^{\text{sample}} = \frac{E_2^{\text{sample}}}{E_1^{\text{sample}}} \qquad (2.11)$$

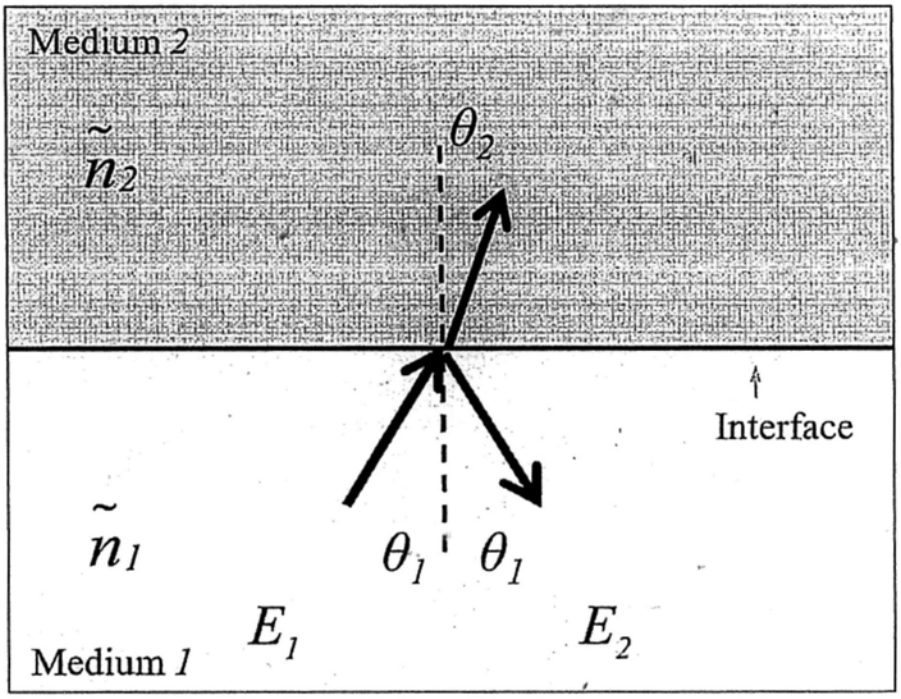

Figure 2.3: Schematic diagram of reflection geometries with the incidence angle.

The wave incident on the interface is the same for both measurements so $E_1^{\text{sample}} = E_1^{\text{ref}}$, and therefore the optical properties can be determined by ratio M as stated in Equation 2.21, assuming the THz beam propagating is s-polarized.

$$\begin{aligned}\frac{R^{\text{sample}}}{R^{\text{ref}}} &= \frac{E_2^{\text{sample}}}{E_2^{\text{ref}}}\\ &= \frac{(\tilde{n}_{\text{quartz}}\cos\theta_{\text{quartz}} - \tilde{n}_{\text{sample}}\cos\theta_{\text{sample}})(\tilde{n}_{\text{quartz}}\cos\theta_{\text{quartz}} + \tilde{n}_{\text{air}}\cos\theta_{\text{air}})}{(\tilde{n}_{\text{quartz}}\cos\theta_{\text{quartz}} + \tilde{n}_{\text{sample}}\cos\theta_{\text{sample}})(\tilde{n}_{\text{quartz}}\cos\theta_{\text{quartz}} - \tilde{n}_{\text{air}}\cos\theta_{\text{air}})}\\ &= M\end{aligned} \qquad (2.12)$$

In order to extract $\tilde{n}_{\text{sample}}$, we rearrange above equation as below,

$$\begin{aligned}\tilde{n}_{\text{sample}}\cos\theta_{\text{sample}} &= \tilde{n}_{\text{quartz}}\cos\theta_{\text{quartz}}\\ &\cdot \frac{(1-M)\tilde{n}_{\text{quartz}}\cos\theta_{\text{quartz}} + (1+M)\tilde{n}_{\text{air}}\cos\theta_{\text{air}}}{(1-M)\tilde{n}_{\text{air}}\cos\theta_{\text{air}} + (1+M)\tilde{n}_{\text{quartz}}\cos\theta_{\text{quartz}}}\end{aligned} \qquad (2.13).$$

From Snell's law, we know that the angle is actually dependent on the refractive index of the medium where the light propagates

$$n_{\text{sample}}\sin\theta_{\text{sample}} = n_{\text{air}}\sin\theta_{\text{air}} \qquad (2.14).$$

From (2.13) we know that

$$\cos\theta_{\text{sample}} = \frac{1}{n_{\text{sample}}}\text{Re}\{\tilde{n}_{\text{quartz}}\cos\theta_{\text{quartz}} \cdot \frac{(1-M)\tilde{n}_{\text{quartz}}\cos\theta_{\text{quartz}} + (1+M)\tilde{n}_{\text{air}}\cos\theta_{\text{air}}}{(1-M)\tilde{n}_{\text{air}}\cos\theta_{\text{air}} + (1+M)\tilde{n}_{\text{quartz}}\cos\theta_{\text{quartz}}}\} \qquad (2.15).$$

Then substitute Equation 2.15 into Equation 2.13 and we can obtain $\tilde{n}_{\text{sample}}$. Meanwhile, the refractive index and absorption coefficient can also be determined as

$$n(\omega) = \frac{c}{\omega\cos\theta_{\text{sample}}}\text{Re}\{\tilde{n}_{\text{quartz}}\cos\theta_{\text{quartz}} \cdot \frac{(1-M)\tilde{n}_{\text{quartz}}\cos\theta_{\text{quartz}} + (1+M)\tilde{n}_{\text{air}}\cos\theta_{\text{air}}}{(1-M)\tilde{n}_{\text{air}}\cos\theta_{\text{air}} + (1+M)\tilde{n}_{\text{quartz}}\cos\theta_{\text{quartz}}}\} \qquad (2.16)$$

$$\alpha(\omega) = -\frac{2}{\cos\theta_{\text{sample}}}\text{Im}\{\tilde{n}_{\text{quartz}}\cos\theta_{\text{quartz}} \cdot \frac{(1-M)\tilde{n}_{\text{quartz}}\cos\theta_{\text{quartz}} + (1+M)\tilde{n}_{\text{air}}\cos\theta_{\text{air}}}{(1-M)\tilde{n}_{\text{air}}\cos\theta_{\text{air}} + (1+M)\tilde{n}_{\text{quartz}}\cos\theta_{\text{quartz}}}\} \qquad (2.17).$$

2.5 Baseline Evaluation in Reflective Geometry

In reflection geometry, samples are typically placed on a quartz window. The terahertz radiation is focused onto the top surface of the window (see Figure 2.4). As the incident THz pulse propagates across the quartz window, the reflected signal will contain two reflections, namely the reflected pulse from the bottom (pulse 1) and top (pulse 2) of the quartz window. The pulse 1 is named "baseline". Clearly, only pulse 2 takes the sample information including in. So our aim is to filter out baseline from the collected data.

Pulse 1 has an enduring signal or "ringing" which will extend into the region of reflection 1. Due to this overlap, the tail cannot be measured directly. Therefore, a method with 3 measurement steps was used to obtain data See Figure 2.5, a) An additional quartz plate is placed on the quartz window to obtain a baseline. The window is made of a material with minimal absorption at terahertz frequencies such as silicon or z-cut quartz. Since the radiation is now effectively passing through a

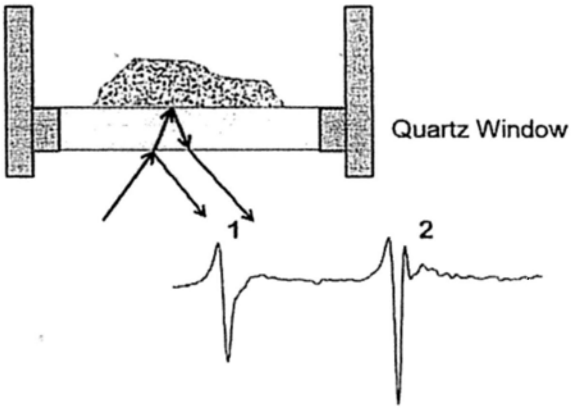

Figure 2.4: Schematic diagrams to illustrate the baseline artefacts.

very thick layer of quartz, there are no reflections except for those off the lower surface of the fixed quartz window. b) The beam is focused onto the top surface of the quartz plate and a reference is taken, for example with nothing on the quartz plate: just a quartz/air interface. c) The sample is placed on the quartz plate. Therefore a baseline waveform is subtracted from both the reference and sample waveforms to remove any back-surface reflection off the quartz/air and quartz/sample interface measurements.

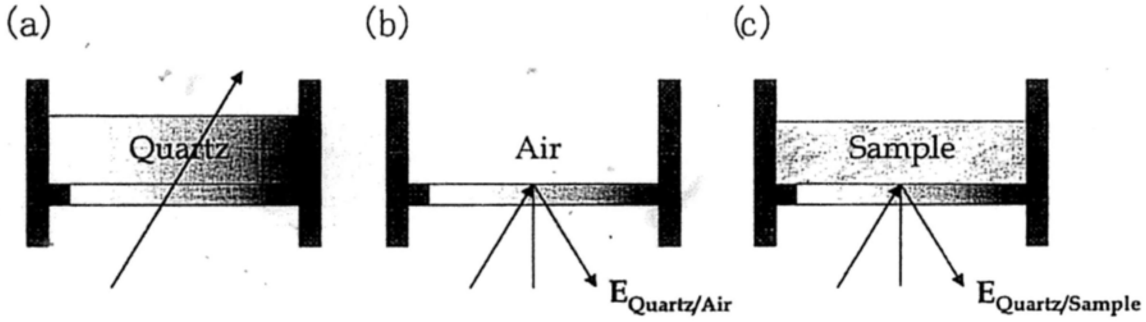

Figure 2.5: Schematic diagrams to illustrate the 3 steps measurement for (a) baseline, (b) reference and (c) sample measurements in reflection.

The acquired data represent the impulse function of the subject convolved with the reference data. Deconvolution is performed to extract the impulse function

(Equation 2.18). In this work a double Gaussian filter function is applied to remove both the low and high frequency noise components and also to produce a suitable time-domain response

$$\text{FFT(ImpulseFunction)} = \text{FFT(Filter)} \times \frac{\text{FFT(Sample} - \text{Baseline)}}{\text{FFT(Reference} - \text{Baseline)}} \qquad (2.18).$$

However, bad contact between quartz windows (Figure 2.5(a)) can introduce errors in the practical experiment. Therefore a new approach to estimate the baseline through water measurement is proposed (Of note, it is not necessary to only use water but any other standard materials with known). Comparing the simulated water reflection with the measured water reflection, we are able to determine the 'ringing' effect. This ringing can then be accounted for in the baseline of unknown samples.

To calculate the baseline, first we need to obtain an air measurement $E^{m}_{\text{air}}(t)$ and a water measurement $E^{m}_{\text{water}}(t)$. Since the baseline reflection $E_{\text{baseline}}(t)$ due to the ringing overlaps the actual reflection due to the sample, the measured electric field in the time domain becomes the superposition of these two reflections:

$$E^{m}_{\text{air}}(t) = E_{\text{air}}(t) + E_{\text{baseline}}(t) \qquad (2.19)$$

$$E^{m}_{\text{water}}(t) = E_{\text{water}}(t) + E_{\text{baseline}}(t) \qquad (2.20).$$

Where $E_{\text{water}}(t)$ and $E_{\text{air}}(t)$ are the actual reflections in the time domain off the quartz/water and quartz/air interfaces respectively. The reflected time domain pulses are Fourier transformed to obtain the corresponding frequency domain spectra, in this case $E_{\text{water}}(\omega)$ and $E_{\text{air}}(\omega)$. For the actual reflected pulses, which are s-polarized in our system, the Fresnel equations and the ratio in Section 2.4 can be used again. Here we define M as,

$$\begin{aligned}\frac{R^{\text{water}}}{R^{\text{ref}}} &= \frac{E_2^{\text{water}}}{E_2^{\text{ref}}}\\ &= \frac{(\tilde{n}_{\text{quartz}}\cos\theta_{\text{quartz}} - \tilde{n}_{\text{water}}\cos\theta_{\text{water}})(\tilde{n}_{\text{quartz}}\cos\theta_{\text{quartz}} + \tilde{n}_{\text{air}}\cos\theta_{\text{air}})}{(\tilde{n}_{\text{quartz}}\cos\theta_{\text{quartz}} + \tilde{n}_{\text{water}}\cos\theta_{\text{water}})(\tilde{n}_{\text{quartz}}\cos\theta_{\text{quartz}} - \tilde{n}_{\text{air}}\cos\theta_{\text{air}})}\\ &= M\end{aligned} \qquad (2.21).$$

Values for $\tilde{n}_{\text{air}}$ and θ_{air} are known. Spectroscopy data acquired in transmission geometry are used for calculating $\tilde{n}_{\text{quartz}}$ and $\tilde{n}_{\text{water}}$. The angles θ_{quartz} and θ_{water} can be calculated from Snell's law:

$$n_{\text{quartz}} \sin\theta_{\text{quartz}} = n_{\text{air}} \sin\theta_{\text{air}} = n_{\text{water}} \sin\theta_{\text{water}} \qquad (2.22).$$

From the above three equations, we obtain the following formula for $E_{\text{baseline}}(\omega)$:

$$E_{\text{baseline}}(\omega) = \frac{E^{m}_{\text{water}}(\omega) - M \cdot E^{m}_{\text{air}}(\omega)}{1 - M} \qquad (2.23)$$

$$E_{\text{baseline}}(t) = \text{FFT}^{-1}\{\frac{E^{m}_{\text{water}}(\omega) - M \cdot E^{m}_{\text{air}}(\omega)}{1 - M}\} \qquad (2.24).$$

2.6 Terahertz Setup in Transmission Geometry

In this section, we outline a basic technique of transmission mode THz time-domain spectroscopy (THz-TDS) system based on photoconductive antennas. A typical transmission mode THz-TDS system is shown in Figure 2.6. A MiraSeed (Coherent) Ti-sapphire femtosecond modelocked laser is used as a source of the optical pulses. It is pumped by the Verdi (Coherent) V6 with a wavelength of 532 nm. The femtosecond laser produces an output pulse duration of approximately 20 fs at a repetition rate of 76 MHz. The laser has an output power of 1 W with a center wavelength of 800 nm. The femtosecond source is split into a probe beam and a pump beam using a non-polarised 50:50 beamsplitter. An optical chopper with SR540 controller is used to modulate the pump beam at approximately 2 kHz. The modulated beam is then focused onto the emitting antenna using a 6 mm diameter plano-convex optical lens that has a focal length of 12 mm. Here, the photoconductive antenna is at 90 Vdc using a standard low current power supply. As the modulated laser beam hits the emitter, a THz pulse is generated. The THz pulse is coupled and collimated into free space using a Si hyper-hemispherical lens, which is then further collimated using a pair of off-axis 90 paraboloidal mirrors. The collimated THz beam is focused onto the sample as shown in Figure 2.6. The transmitted pulse is then recollimated and refocused onto the photoconductive detector using a second pair of off-axis 90° paraboloidal mirrors. The probe beam gates the transmitted THz pulse by focusing the probe laser beam using a plano-convex lens onto the photoconductive detector. The averaged THz pulse can be sampled by varying the time delay of the retroreflector mounted onto a delay stage. A lock-in amplifier model is used to extract the signal received at the detector. Signal analysis and data processing are carried out using LabVIEW and Matlab software packages.

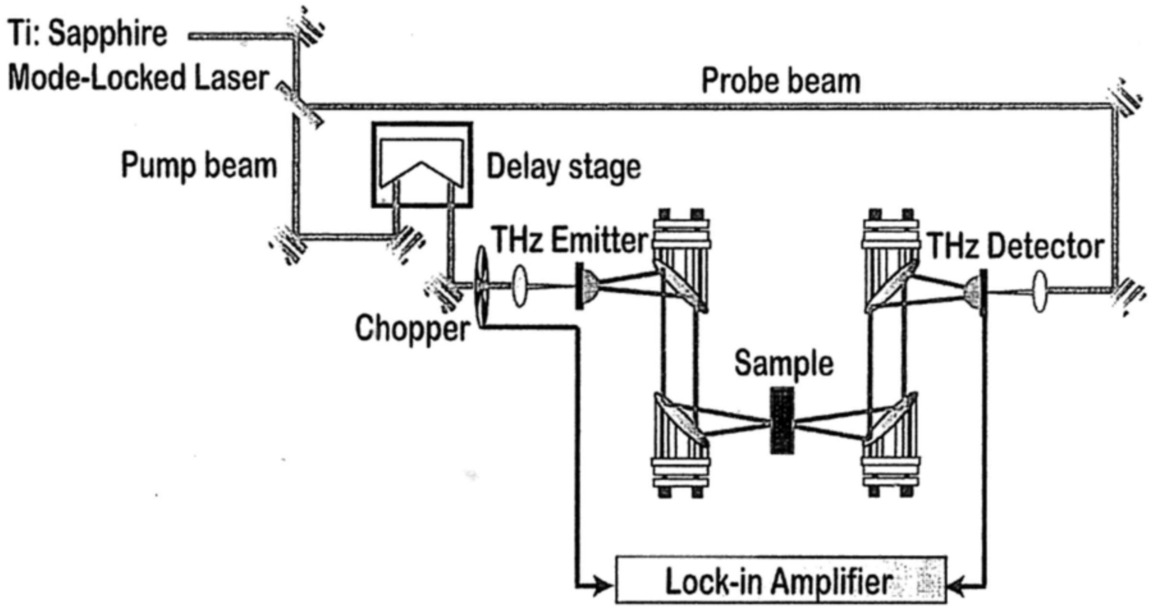

Figure 2.6: THz time domain spectrometer. This schematic diagram was supported by Dr. Jegathisvaran Balakrishnan. The sample under test is placed at the focal plane.

The temporal electric field and its corresponding spectral amplitude obtained from the THz-TDS spectrometer illustrated in Figure 2.6 are shown in Figure 2.7. Figure 2.7 (top), shows a typical temporal profile of a reference signal. In Figure 2.7 (bottom), the spectral amplitude is obtained by fast Fourier transforming the temporal profile. According to Figure 2.7 (bottom), a bandwidth of approximately 1.6 THz is achieved in our setup configuration. Here, the bandwidth is mainly controlled by the pulse width of the optical source (i.e., femtosecond laser), carrier lifetime of the photoconductive antenna, and also the water vapour absorption. Therefore, in order to maximise bandwidth, a femtosecond laser with a pulse width of approximately 20 fs and photoconductive that have a very short carrier lifetime are used. Furthermore, the water line effects can be reduced by purging the nitrogen chamber with nitrogen gas.

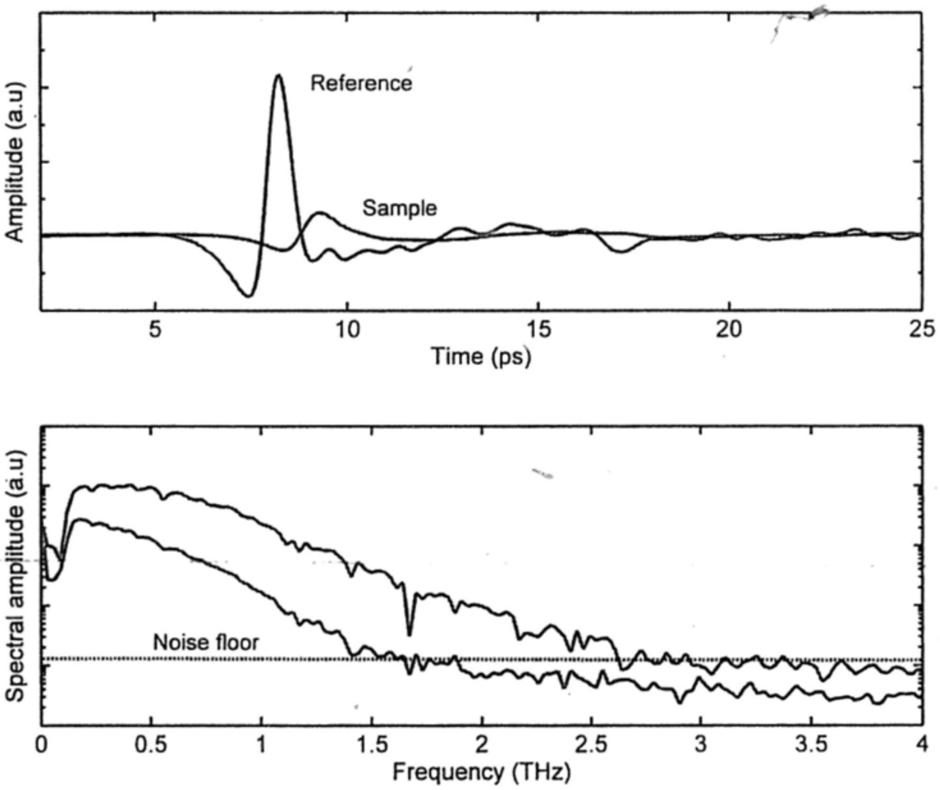

Figure 2.7: Typical temporal profile and spectral amplitude. This figure (top) illustrates a typical temporal profile of a reference signal and (bottom) its corresponding spectral amplitude of our transmission setup. A bandwidth of up to 1.6 THz is obtained from our experimental setup illustrated in Figure 5.3.

2.7 Data Analysis in Transmission Geometry

In a transmission experiment, we assume that a THz pulse propagates from the first medium (medium 1) through a sample (medium 2) to the third medium (medium 3). The data-analysis for the work presented in chapter 5 is based on the transmission geometry. Here, the dielectric properties of a material are determined by measuring the terahertz pulses twice and convert pulses from the time-domain into the frequency-domain by a Fourier Transformation. We will explain more in the next section as a liquid sample cell is considered about in the transmission system.

2.8 Liquid Cell in Transmission Geometry

A typical sample cell geometry used for liquid measurement in transmission system is illustrated in Figure 2.8.

This solution sample cell consists of two homogeneous parallel plates (TOPAS^{TM} COC 5013L 10) that are sandwiched together. Each plate has a thickness which is denoted by d_{cell} in Figure 2.8. The cell allows for a small volume of solution to reside between the plates. Here, a spacer with a thickness, d_{liquid}, is inserted in between the parallel plates. The solution is deposited on one half of the bottom plate while the other half is kept pressed together. Each substrate is housed in an aluminum frame, one of which contains two identical apertures (approximately 4.7 mm diameter). The solution covers one of the apertures, while the other contains an equivalent volume of air trapped between the two plates. The clear empty aperture serves as a reference. Terahertz radiation are illuminated through the window cells to produce $E_{\text{reference}}$ (Figure 2.8a). For the sample measurements, the air gap with thickness, d_{liquid}, is filled with liquid. Illumination by terahertz radiation through this window cell set up produces E_{sample} (Figure 2.8b). The experimentally measured spectral components of the reference and sample signal can be modeled by

$$\begin{aligned}\tilde{E}_{\text{reference}}(\omega) = T_{12}(\omega) \cdot P_2(\omega, d_{\text{cell}}) \cdot T_{23_{\text{air}}}(\omega) \cdot P_{3_{\text{air}}}(\omega, d_{\text{liquid}}) \\ \cdot T_{3_{\text{air}}4}(\omega) \cdot P_4(\omega, d_{\text{cell}}) \cdot T_{45}(\omega) \cdot A(\omega)\end{aligned} \tag{2.25}$$

$$\begin{aligned}\tilde{E}_{\text{sample}}(\omega) = T_{12}(\omega) \cdot P_2(\omega, d_{\text{cell}}) \cdot T_{23_{\text{liquid}}}(\omega) \cdot P_{3_{\text{liquid}}}(\omega, d_{\text{liquid}}) \\ \cdot T_{3_{\text{liquid}}4}(\omega) \cdot P_4(\omega, d_{\text{cell}}) \cdot T_{45}(\omega) \cdot A(\omega) \cdot FP(\omega)\end{aligned} \tag{2.26}$$

where T_{ab} is the transmission amplitude coefficient from interface a to interface b and $P_i(\omega, d)$ is the propagation coefficient in medium i over thickness d. Also, $A(\omega)$ accounts for the amplitude of each frequency component. Taking the ratio of Equations 2.25 and 2.26 gives the complex transmission coefficient as follows:

$$\begin{aligned}\tilde{T}(\omega) &= \frac{\tilde{E}_{\text{sample}}(\omega)}{\tilde{E}_{\text{reference}}(\omega)} \\ &= \frac{T_{23_{\text{liquid}}}(\omega) \cdot P_{3_{\text{liquid}}}(\omega, d_{\text{liquid}}) \cdot T_{3_{\text{liquid}}4}(\omega)}{T_{23_{\text{air}}}(\omega) \cdot P_{3_{\text{air}}}(\omega, d_{\text{liquid}}) \cdot T_{3_{\text{air}}4}(\omega)} \cdot FP(\omega) \\ &= \rho e^{-i\varphi}\end{aligned} \tag{2.27}$$

Here, ρ is denoted as the magnitude and phase, φ of the complex transmission coefficient, $T(\omega)$. The $FP(\omega)$ accounts for multiple reflections or Fabry-Perot reflection. Here, in order to avoid complications from the $FP(\omega)$, it is assumed that the window cell and liquid sample under investigation are sufficiently thick so that $FP(\omega) = 1$. Thus, Equation 2.27 can be simplified and expressed as

$$\tilde{T}(\omega) = \frac{\tilde{n}_{3_{\text{liquid}}}(\tilde{n}_2 + 1)^2}{(\tilde{n}_2 + \tilde{n}_{3_{\text{liquid}}})^2} \exp(\frac{-i\omega d_{\text{liquid}}}{c}(\tilde{n}_{3_{\text{liquid}}} - 1)) \tag{2.28}$$

where the complex refractive index of the window cell is $\tilde{n}_2 = \tilde{n}_4$. The refractive index of air is denoted as $\tilde{n}_1 = \tilde{n}_5 = \tilde{n}_{\text{air}} = 1$. Here, $\tilde{n}_3$ liquid is the complex refractive index of the liquid. With the above assumption, the analytic expression for the THz material parameters can be found with some approximation given in Duvillaret *et al.* (1999) [43]. Substituting the complex refractive index, $\tilde{n}_{3_{\text{liquid}}} = n_{3_{\text{liquid}}} - i\kappa_{3_{\text{liquid}}}$ into Equation 2.28 reveals the frequency dependent phase information,

$$\varphi(\omega) = \frac{i\omega d_{\text{liquid}}}{c}(n_{3_{\text{liquid}}} - 1) \tag{2.29}$$

and the frequency dependent magnitude

$$\rho(\omega) = \frac{n_{3_{\text{liquid}}}(\omega)(n_2+1)^2}{(n_2+n_{3_{\text{liquid}}}(\omega))^2}\exp(-\frac{\omega d_{\text{liquid}}}{c}\kappa_{3_{\text{liquid}}}(\omega)) \quad (2.30).$$

Rearranging Equation 2.30 produces frequency dependent refractive index,

$$n_{3_{\text{liquid}}}(\omega) = \frac{\varphi(\omega)c}{\omega d_{\text{liquid}}} + 1 \quad (2.31).$$

The frequency dependent extinction coefficient can be obtained by rearranging Equation 2.31. Thus, the extinction coefficient can be expressed as

$$\kappa_{3_{\text{liquid}}}(\omega) = -\frac{c}{\omega d_{\text{liquid}}}\ln[\rho(\omega)\frac{(n_2+n_{3_{\text{liquid}}}(\omega))^2}{n_{3_{\text{liquid}}}(\omega)(n_2+1)^2}] \quad (2.32).$$

The frequency dependent absorption coefficient can be written as follows:

$$\alpha_{\text{liquid}}(\omega) = 2\frac{\kappa_{3_{\text{liquid}}}(\omega)\omega}{c} \quad (2.33).$$

One may rewrite Equation 2.33 as follows:

$$\alpha_{\text{liquid}}(\omega) = -\frac{2}{d_{\text{liquid}}}\ln[\rho(\omega)\frac{(n_2+n_{3_{\text{liquid}}}(\omega))^2}{n_{3_{\text{liquid}}}(\omega)(n_2+1)^2}] \quad (2.34).$$

Figure 2.9 shows the custom-built liquid cell using TOPAS™ COC 5013L10 as a window material. This liquid cell allows one time sample preparation for measurements of reference and sample signals as compared to previously discussed liquid cells which require separate sample preparation for each measurement.

2.9 Summary

This chapter has summarized the mathematical techniques employed in the study reported herein. We have explained how we extract the frequency dependent refractive index and absorption coefficient from both systems under use and how these processing steps are applied to the results that are reported in Chapters 3,4 and 5.

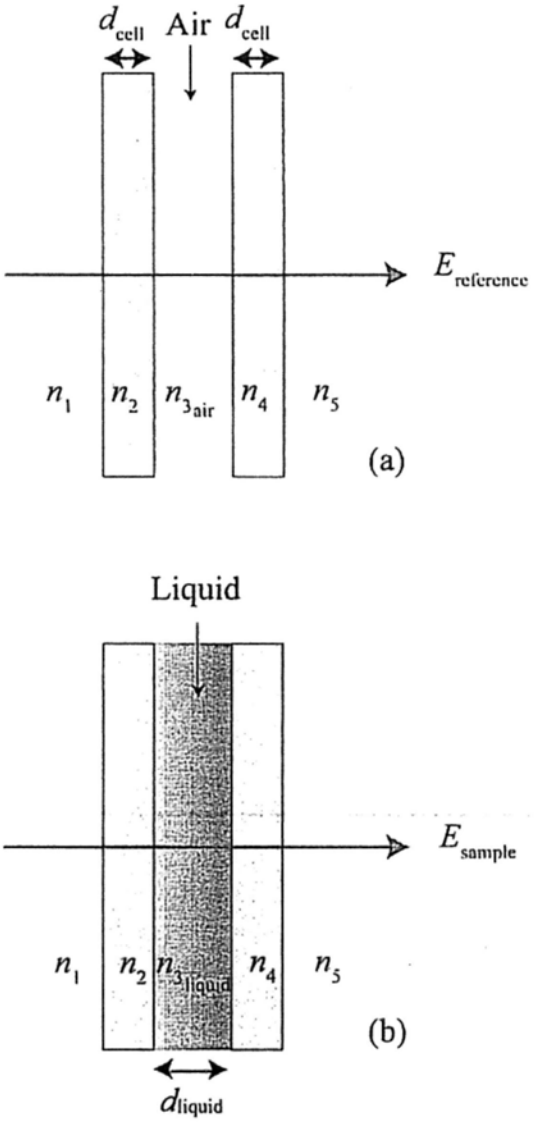

Figure 2.8: Transmission schematics for the liquid sample cell geometry. This schematic illustrates the notation for specifying THz radiation propagation through liquid sample, inserted in polymer window cell.

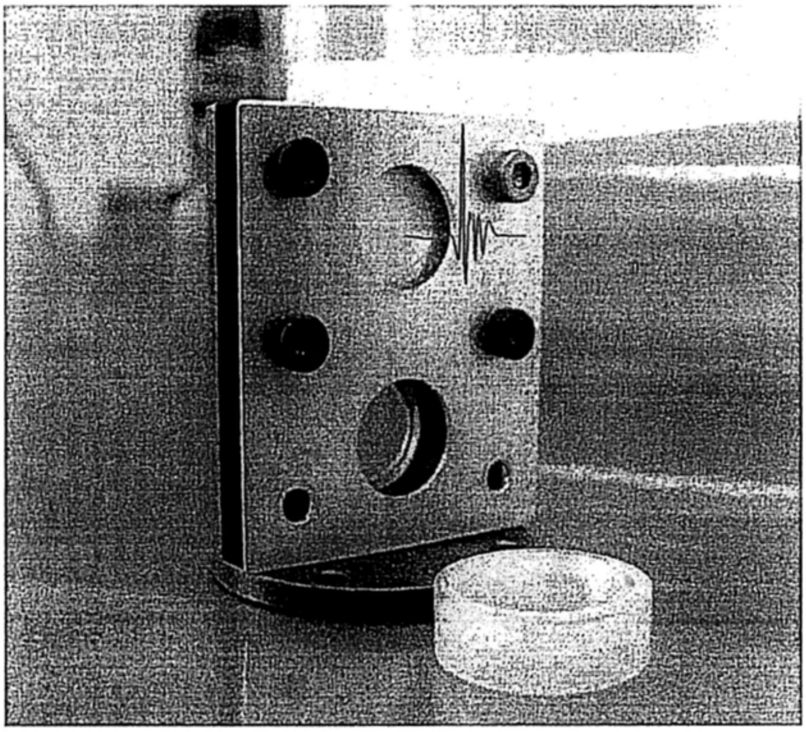

Figure 2.9: Custom-built fixed thickness liquid cell. This figure illustrates our custom-built fixed thickness liquid cell using TOPAS^{TM} COC 5013L 10 as a window material. This window cell is design with two windows; one for reference measurement and one for sample measurement.

Chapter 3

Effects of Formalin Fixing on the Terahertz Properties of Biological Tissues

Formalin-fixing is the most common preservation technique used on histologically prepared tissues. Therefore, in order to advance medical imaging and spectroscopic applications of THz radiation, there is a need to make measurements on formalin-fixed samples so that typical responses and biological variation can be determined, and contrast mechanisms for *in vivo* images can be investigated. In this chapter, a controlled study to investigate the effects of formalin fixing on the terahertz properties of two different tissue types (porcine adipose tissue and muscle) is given. The optical properties of fresh and formalin fixed samples in the terahertz frequency range were measured using THz reflection spectroscopy. The results are compared and we discuss how the fixing process can affect image contrast in terahertz images of biological samples.

3.1 Introduction

There is an increasing interest in biomedical applications of THz radiation because it is non-ionizing, non-destructive and non-invasive, subject to far less Rayleigh scatter than IR or optical wavelengths and is highly sensitive to moisture content. Several terahertz studies of freshly excised tissue have highlighted the sensitivity of terahertz imaging to biological tissues. For instance, terahertz images of skin cancer have shown contrast between healthy and diseased areas [37]. The contrast can be attributed to differences in the fundamental properties of the tissues [44]: diseased skin tissue (basal cell carcinoma) has been found to have an increased absorption coefficient compared to the adjacent normal tissue [45]. In a breast cancer study, terahertz images of freshly excised human breast tissue revealed tumor margins that correlated well with those from histology [16] and recent terahertz reflection spectroscopy of freshly excised rat tissues has been able to distinguish between healthy tissues from different organs [46]. However, it is not always possible to obtain fresh samples for a study; the most common preservation technique is formalin-fixing.

Formalin-fixing is used to preserve tissues for routine histo-pathological diagnosis and the resulting samples are often useful for retrospective studies. Another common method for treating the fresh tissues is lyophilization and investigations of samples with this treatment process includes recent work reported by Png *et al.* [47] and Hoshina *et al.* [48]. However along with sample variability, the sample distortion caused by formalin-fixing can present challenges. For example DNA information is often spoiled by the fixing process [49]. Previous terahertz images of histo-pathological samples have been able to reveal contrast between different tissue types. Knobloch *et al.* (2001) imaged formalin-fixed and paraffin-embedded samples in transmission geometry and contrast between the soft tissue and the cartilage of a pig larynx was seen at particular frequency windows [50]. Similarly they observed contrast between the healthy and diseased areas in an image of a histo-pathological human liver sample with metastasis. The several different samples were fixed for 24 hours in 10% formalin solution and measured using terahertz spectroscopy in reference [51]. However, it would be useful to know if there would there have been more terahertz contrast if the samples had been measured in a fresh state, or conversely if the fixing process had enhanced the terahertz contrast.

3.2 Sample Preparation

Three samples of white adipose tissue and two samples of porcine skeletal muscle were taken from the same piece of meat for investigation. The meat was from an abattoir and stored in a refrigerator, it was first measured within 24 hours of collection. Adipose tissue was chosen because fatty tissue is known to have significantly different terahertz properties from other more fibrous/lean tissues; this means that it should be easier to see the contrast before and during the fixing process. The focus of this study was to see how fixing can affect terahertz image contrast i.e. we are investigating intra-subject variation rather than subject to subject (or inter-subject) variation. Thus by taking all the samples from the same piece of meat we were able to study the effects of the fixing process without added subject variation. The samples were therefore all treated and handled in the same way and exposed to the same environmental conditions. Terahertz radiation can penetrate through several millimeters of some dehydrated tissues [41, 52], therefore, to avoid potential etaloning within the sample after the fixing, each sample was cut such that the thinnest dimension was no less than 1cm in thickness. The fresh samples were imaged before the formalin fixing process began. A standard protocol was followed for this process [53, 54] whereby non-buffered 30% formalin was used. The volume of formalin applied to the sample was at least 20 times the initial sample volume. The sample was then left to soak in the fixative in a sealed container and refrigerated at a constant temperature (4°C). The penetration of formalin is related to the temperature of the solution [55] and so great care was taken to store all samples and formalin at the same temperature. Before placing the fixed tissue sample to be measured on the quartz window, the sample was washed under running water for 20 minutes to remove the excess formalin and then dried using blotting paper. During imaging, gentle pressure was applied to the sample to ensure it made good contact with the quartz [45]. This became more difficult as the fixing progressed as the sample became more rigid. In order to monitor the changes caused by the formalin, each sample was measured after being fixed for 24 hours, 48 hours and 72 hours. Only data points where the sample had made good contact with the quartz window were used in the following results. Figure 3.1 shows the photograph of a tissue sample placed on the quartz window of our system.

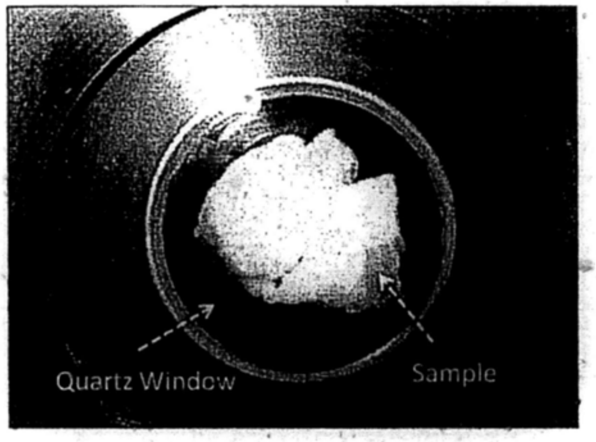

Figure 3.1: Photograph of a sample to be imaged placed on the quartz window.

3.3 Frequency-domain Analysis

The raw terahertz data obtained by our system are recorded in the time domain. However since the fundamental optical properties of interest, namely the refractive index and absorption coefficient, are frequency dependent, we present the frequency domain analysis first.

By Fourier transforming the sample data and applying Fresnel equations to both sample and reference data, as detailed in reference [46], the refractive index and absorption coefficient were calculated. The reflection off the quartz/air interface was used as the reference data throughout this study. The calculated mean refractive index and mean absorption coefficient from the fresh and fixed sample measurements over time are plotted in Figure 3.2 and Figure 3.3 for the muscle and adipose tissue samples respectively. Data for water and formalin are also plotted for comparison. In Figure 3.4 we plot the mean refractive index and mean absorption coefficient

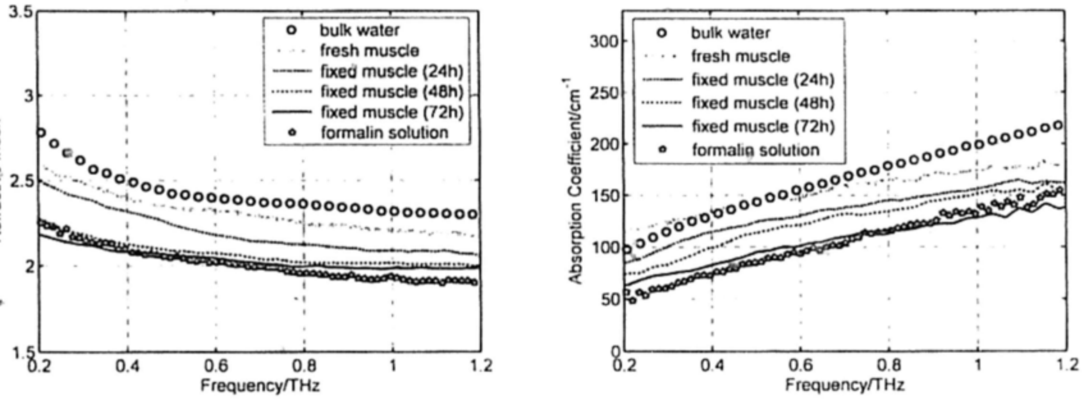

(a) (b)

Figure 3.2: The mean refractive index (a) and absorption coefficient (b) of skeletal muscle before and after formalin fixing for 24, 48 and 72 hours. Bulk water and formalin optical properties are also plotted for reference.

from the adipose tissue and skeletal muscle samples for both when the samples were fresh and also after 72 hrs of formalin fixing. Following standard statistical methods, we calculate the 95% confidence intervals [56] for the tissue samples by averaging over all samples of each tissue type (a total of more than 500 data points were used for each tissue type). The confidence intervals are plotted as error bars in Figure 3.4 to illustrate that both before and after fixing, there are statistically significant differences between the terahertz properties of the tissues (since the error bars do not overlap). The terahertz properties of water have also been plotted alongside those of the fresh muscle to highlight that although the muscle tissue properties are close to those of water, they are significantly different over most of the frequency range investigated.

The refractive index of the skeletal muscle decreased as the fixing time increased and seemed to converge after 48 hours. Comparing the fresh and fixed samples, the refractive index changed noticeably at the lower frequencies, falling from 2.6 (fresh) to 2.2 (72 hrs) at 0.2 THz. Above approximately 0.8 THz, the curves of the fixed samples started to plateau towards a constant refractive index of 2 [Figure 3.2(a)]. Since water was being removed from the tissue, it is logical that the absorption

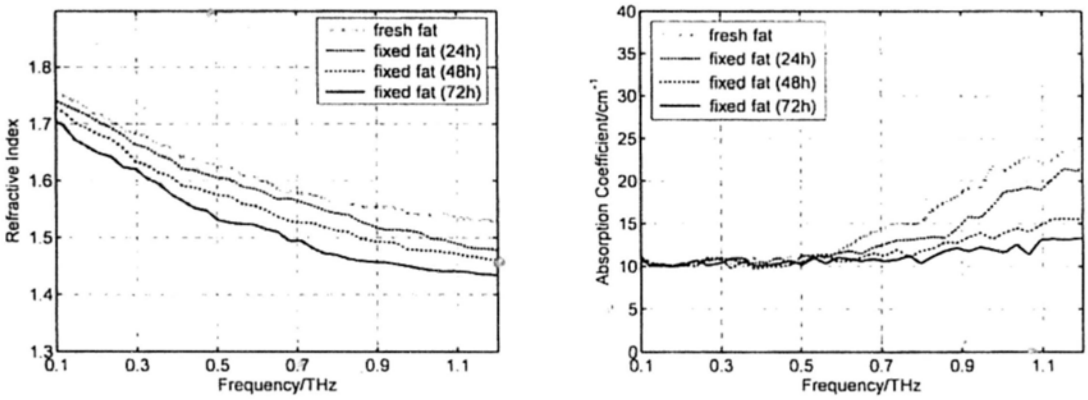

(a)

(b)

Figure 3.3: The mean refractive index (a) and absorption coefficient (b) of white adipose tissue before and after formalin fixing for 24, 48 and 72 hours.

coefficient should also be reduced by the fixing process, as shown in Figure 3.2. Before fixing, the absorption coefficient of the skeletal muscle tissue was about 120 cm^{-1} at 0.2 THz, it decreased rapidly to 60 cm^{-1} after only 24 hours. During the first 24 hours, the percentage of moisture being replaced was at its greatest, but as the fixing progressed there was less and less water left to be displaced and so the changes in optical properties decreased and tended towards zero as the fixing time increased. Other studies have also indicated that terahertz properties are dependent on the sample hydration. For instance Stringer *et al.* (2005) investigated *ex vivo* samples of human cortical bone and found that dehydrating the sample reduced both the absorption coefficient and the refractive index of the samples [57].

Similarly, above 0.6 THz, the refractive index and absorption coefficient of the white adipose tissue decreased as the fixing time increased. However the changes in the adipose tissue refractive index were not as significant as for the muscle. We explain these observations by considering the molecular interactions of the formalin with both muscle and adipose tissue.

Formalin is a saturated solution of formaldehyde (chemical formula: HCHO), water, and methanol. Unlike most anti-bacterial and germicidal agents which poison the bacteria and germ cells, formaldehyde kills cell tissue by dehydrating the

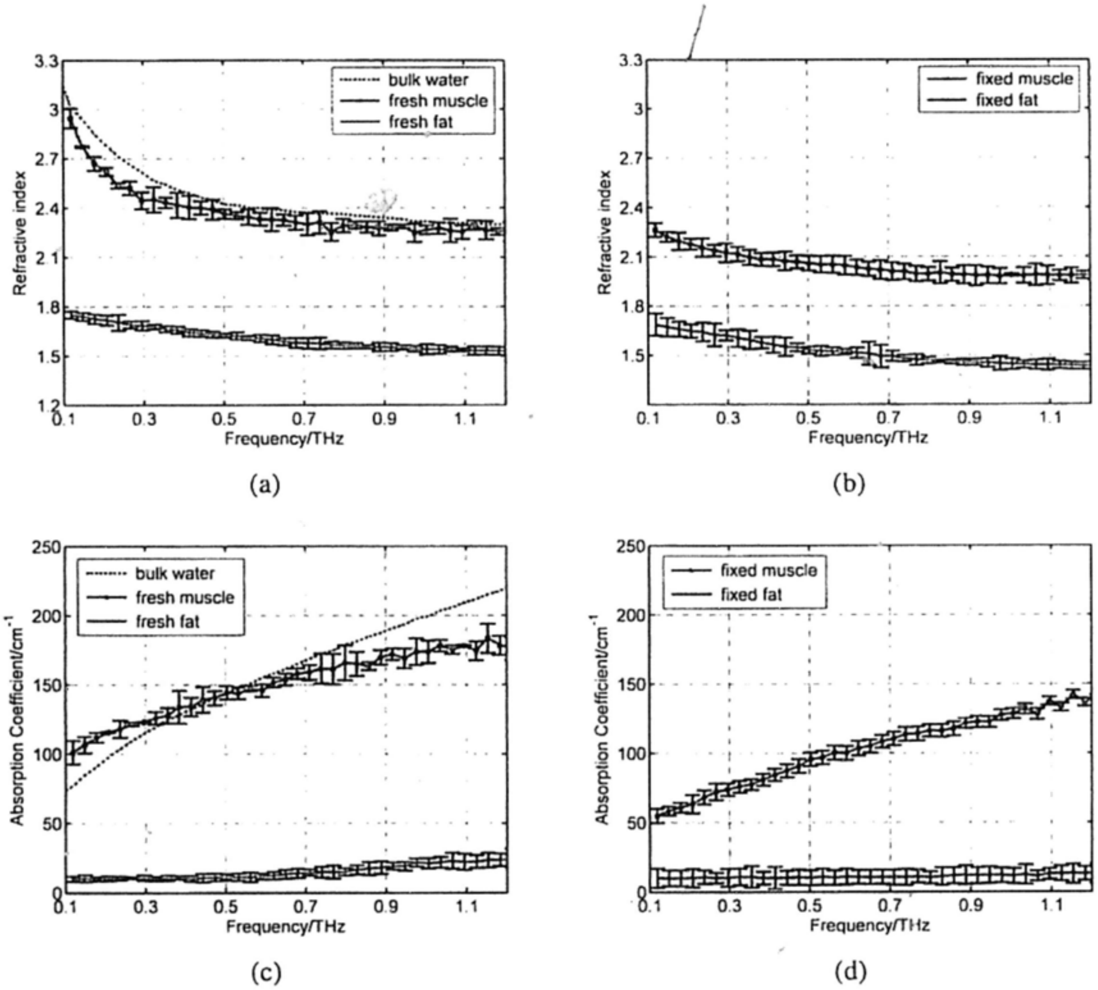

(a) (b)

(c) (d)

Figure 3.4: The mean refractive index and absorption coefficient for fresh and fixed samples of fat and muscle. Error bars represent 95% confidence intervals. The water data were acquired in transmission and the error bars are too small to be seen on this graph.

tissue and bacteria cells and replacing the normal fluid in the cells with a gel-like rigid compound [58]. Additionally, the structure of the protein in the "new" cell will resist further bacterial attacks [59, 60]. Tissue and bacterium cells are made of protoplasm and as such, contain large amounts of moisture. Skeletal muscle cells contain several types of protein and have a high water content. The water content in the muscle tissue is about 75%-80% [61] and from Figure 3.2 we see that the refractive index and absorption coefficient of the fresh muscle are close to those of water. Additionally, the refractive index and absorption coefficient of formalin are much lower than those of water or fresh tissue. The introduction of formaldehyde into the tissue dries out the protoplasm and destroys the cell. Since water is being removed from the tissue, it is logical that the absorption coefficient should be reduced by the fixing process. Similarly, the refractive index is also reduced and becomes closer to that of formalin. In contrast to the muscle tissue, white adipose tissue cells contain a single large fat droplet, and the water content is about 10%-30% [61] which is far less than the muscle tissue. This means there is very little water for the formaldehyde to displace and so we do not see such significant changes in the terahertz properties of the adipose tissue.

3.4 Time-domain Analysis

The amplitude and phase of a terahertz pulse reflected off a medium are dependent on the complex refractive index of the medium (as well as the incident pulse). As in optics, if a terahertz pulse is reflected by a medium of higher refractive index then it incurs a phase change of 180°. Conversely, if a terahertz pulse is reflected by a medium of lower refractive index, there is no phase change. Given that in Section 3.3 we have seen changes in the refractive index and absorption coefficients of the samples during the fixing process, we also expect to see changes in the reflected terahertz pulses.

To analyze the reflected time domain pulses meaningfully the system response

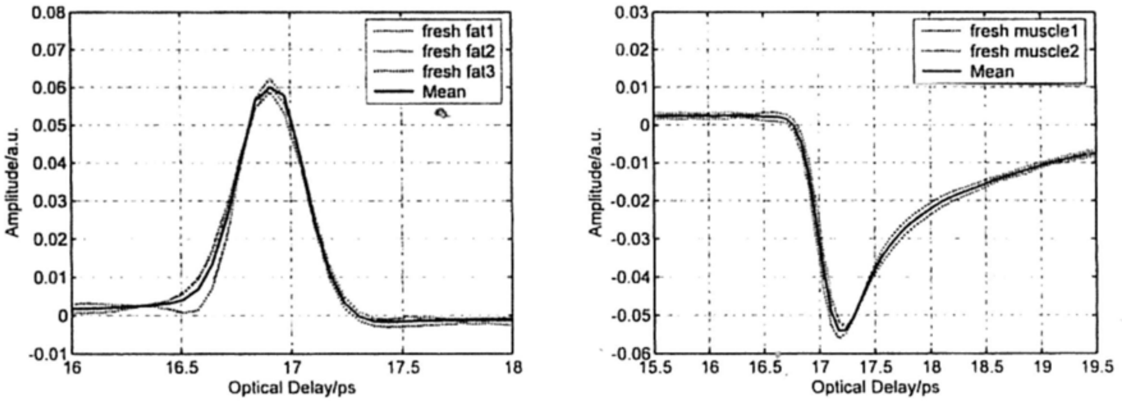

(a) (b)

Figure 3.5: The deconvolved waveforms for fresh samples of (a) adipose tissue and (b) skeletal muscle.

was removed. This was done by deconvolving the sample pulse by the reference pulse and applying a band pass (double Gaussian) filter to reduce the noise as detailed in our previous work [19]. The resulting waveforms for the three fresh adipose tissue samples and two fresh skeletal muscle samples and their corresponding means are illustrated in Figure 3.5. From Figure 3.5, we see that there is some variation between samples from the same type of tissue but that this variation is slight. In Figure 3.6 we illustrate the effects of the formalin fixing by plotting the mean deconvolved waveforms of each tissue type.

As seen in Figure 3.6(a), when the fixing time increased the waveform amplitude of the adipose tissue also increased. This was primarily because the refractive index of the adipose (Figure 3.6(a)) was decreasing over the majority of the bandwidth (due to the fixing) and this meant there was a greater difference between the refractive index of the quartz ($n \sim 2.1$) and that of the adipose (e.g.1.5 at 1 THz when fixed compared to 1.6 when it was fresh). From Fresnel theory, this increased difference in refractive indices resulted in a greater reflected amplitude.

As the fixing time increased for the muscle, three main changes were apparent. A small peak started to appear preceeding the trough and the width and magnitude of the trough decreased. These changes can also be explained by considering the

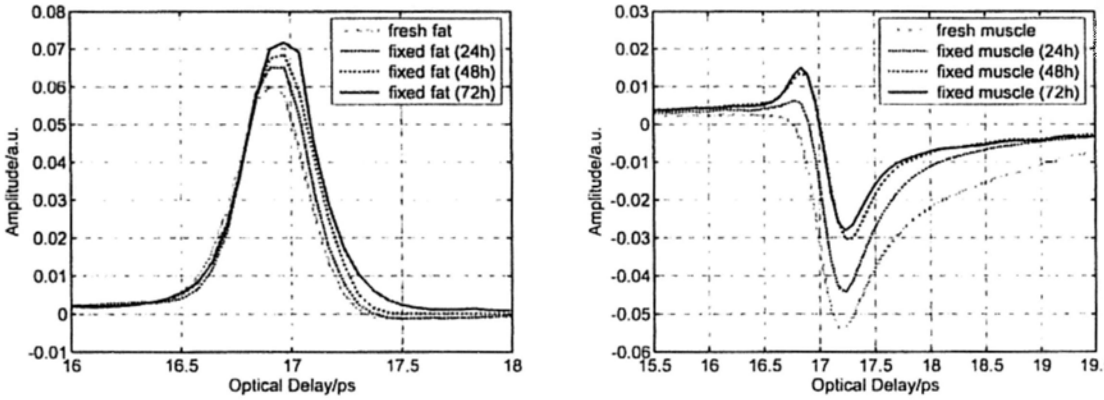

(a) (b)

Figure 3.6: The deconvolved mean waveforms for (a) adipose tissue and (b) skeletal muscle as the fixing time progressed.

effects of the formalin on the refractive index and absorption coefficient of the muscle. For the muscle, the formalin significantly reduced both the refractive index and the absorption coefficient. Before fixing, the refractive index of the fresh muscle was greater than that of quartz ($n \sim 2.1$) over the whole of the frequency range measured. The fixing reduced the refractive index so much that the refractive index became lower than that of quartz at higher frequencies and this was the cause for the small peak which appeared and increased as the fixing time was increased. As the the refractive index and absorption coefficient were reduced they became closer to the optical properties of the quartz. This meant that the reflected waveform was not as intense. Additionally, since the absorption coefficient was reduced there was less broadening of the trough (as more of the higher frequency components were preserved) and so we observed a narrower reflection. Therefore the formalin fixing can significantly affect the terahertz properties of samples such that they are apparent in both the frequency and time domain.

Figure 3.7(a) and Figure 3.7(b) present the deconvolved terahertz waveforms for fresh and fixed tissue respectively. In both figures we can see clear differences between the adipose tissue and muscle waveforms, however the differences are bolder for the fresh sample. When investigating a biological sample we typically look at an

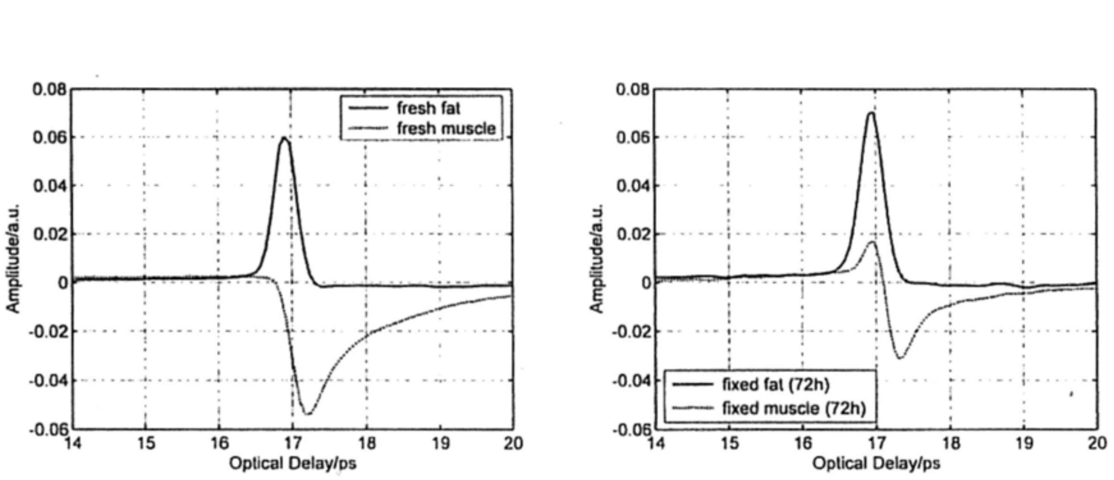

(a) (b)

Figure 3.7: The deconvolved waveforms for (a) fresh and (b) fixed white adipose tissue and skeletal muscle.

image of the whole sample and plot particular properties in the image. For instance we may plot at each pixel the maximum or minimum reflected waveform amplitude, or the refractive index at 1 THz.

Figure 3.8(b) is the terahertz image corresponding to the area of interest in the photograph of the fixed tissue in Figure 3.8(a).To form the image, the maximum amplitude of the deconvolved waveform is plotted on a false-colour scale. The more blue regions have higher maximum waveform amplitude and the redder regions have lower maximum waveform amplitude. The dark blue areas in the image correspond to where there was no sample on the quartz window - these waveforms have the highest amplitude because the reflected pulses are identical to the reference pulses. We can also see contrast between the adipose tissue and the skeletal muscle: the region of this image corresponding to the adipose tissue is pale blue but the rest of the image is more yellow/red. This is because the deconvolved waveforms from the adipose tissue have the same phase as the reference waveform, whereas the deconvolved waveforms from the muscle under go a phase change due to the higher refractive index of the muscle relative to the quartz. Therefore despite reducing the differences in both the time and frequency domain properties of the adipose and muscle, we were still able to distinguish the adipose tissue from the muscle in

Figure 3.8(b).

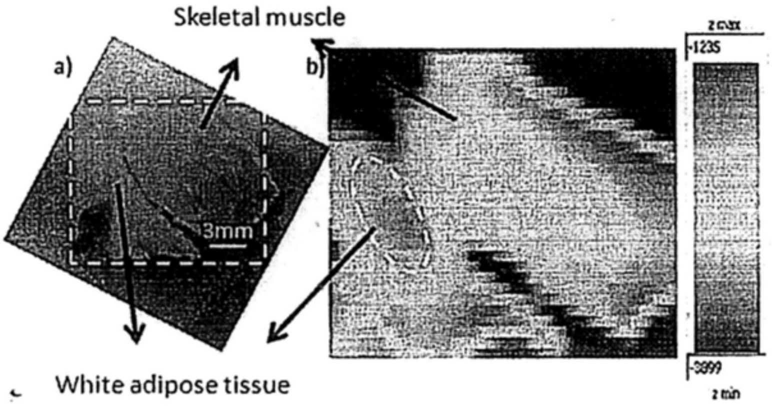

Figure 3.8: (a) Photograph of the fixed tissue. (b) Terahertz image corresponding to the area of interest within the square in (a).

3.5 Summary

In summary, we have used terahertz pulse imaging and reflection spectroscopy to determine the time and frequency dependent optical properties of tissue undergoing formalin fixing. The terahertz properties were affected by the formalin fixing as it (a) displaced water molecules and (b) introduced new intermolecular interactions between the sample and the formalin. It is well known that terahertz radiation is sensitive to hydrogen bonding and thus water content changes. Additionally we infer that the newly introduced intermolecular interactions may also have contributed to the terahertz response.

In our example study of adipose tissue and muscle the fixing process reduced the differences between the absorption coefficient and refractive index. However in this case there were still significant enough differences between the parameters for the two tissue types to be distinguished. In cases where the differences between tissues are more subtle, this may not be the case, and formalin fixing may prevent terahertz imaging from being able to distinguish the samples. Therefore when investigating biomedical applications of TPI it is very important to understand the composition of biological samples and be aware of how formalin fixing may reduce or enhance terahertz image contrast.

Chapter 4

Detecting Conformational Changes of Labeled-IgG Antibodies in Aqueous Phase

The terahertz properties of formalin-fixed tissue have been investigated using the TPI reflection system in Chapter 3. Terahertz pulsed imaging and reflection spectroscopy have been used to determine the differences between the absorption coefficient and refractive index caused by the fixing process. These parameters alone are able to distinguish two types of tissues. Considering that proteins are essential to the structure and function of living organisms, in this chapter, a modified TPI reflection system was used to extend our interest from the macroscopic tissue to the microscopic protein. Two types of antibodies, which only differ on the molecular scale in their conjugation pattern; namely whether it is peroxidase or fluorescein conjugated, have been determined using terahertz dielectric spectroscopy aimed to revel the changes of conformational properties for both of them.

4.1 Introduction

Biological proteins often require an aqueous phase in order to be transported to their target sites. Proteins influence both the spatial and dynamic arrangement of neighboring liquid layers through weak intermolecular interactions [38]. The collective vibrational modes are associated with the protein's tertiary structure and lie in the far infrared or terahertz frequency range [62–64]. With the advent of pulsed terahertz techniques, low frequency dielectric characterization of proteins can be accomplished. Dielectric spectroscopy is a non-invasive, very sensitive technique to investigate complex biological water systems as detailed in previous reviews [65–67]. Indeed, the dielectric spectrum can be used to investigate a number of diverse biological phenomena such as: cell division in lower eukaryotes, ion transport across the membrane, impact of different types of stress on cells as well as cell aging [68–71]. There is abundant literature on the investigation of biological systems such as globular β-lactoglobulin, hen egg white lysozyme and short-chain peptide in solid-phase using THz spectroscopy [72–74]. However, labeled immunoglobulin G (IgG), which constitute an extremely interesting and ample field of research, have not been as intensely studied by this technique. In this chapter we conduct terahertz spectroscopy to study the behavior of antibodies in polar liquid solutions.

Elevated levels of different classes of immunoglobulins can often be used to determine the cause of liver damage in patients whom the diagnosis is unclear [75]. IgG is the most abundant class of antibodies found in blood and tissue liquids and is especially elevated in viral hepatitis, autoimmune hepatitis and cirrhosis [76]. Therefore, over expression of specific IgGs could serve as a biomarker for rapid diagnosis of both acute and persistent infections. Thus, we investigate whether the terahertz properties of biological liquids are affected by the presence of a specific IgG to determine if terahertz spectroscopy could potentially be used for antibody detection in the future.

4.2 Sample Preparation

Two types of antibodies are selected for this investigation. The peroxidase (PX) -conjugated affinity purified goat anti-cat IgG powder and the fluorescein (FITC)-conjugated affinity purified goat anti-cat IgG powder (Jackson ImmunoResearch Laboratories, Inc., West Grove, PA) are dissolved in glycerol solution (Sigma-Aldrich (St. Louis, MO) L6876) at the same concentration of 0.8 mg/ml, and stored in the dark below 4°C. Glycerol is a common component of solvents dissolved in water as it stabilizes the protein molecules and, for frozen samples, it reduces damage due to ice crystal formation. The solutions at room temperature are clear and without precipitates.

4.3 Why Glycerol Solution

Proteins have very well-defined three-dimensional structures. A wide variety of biological functions depend on the protein's structure. The most common structural motifs in proteins are α-helix and β-pleated sheet [77]. The hydrogen bonds between the NH and CO units of the main chain stabilize the α-helix whereas the hydrogen bonds between the β-strands stabilize the β-sheet structure [77]. In order to perform specific biological functions, proteins must have a particular native structure – folded state. Protein folding is the physical process by which a polypeptide folds into its characteristic and functional three-dimensional structure from random coil [78]. Each protein exists as an unfolded polypeptide or random coil when translated from a sequence of mRNA to a linear chain of amino acids. The transformation from an inactive, denatured (unfolded) state to the native (folded) state is called the "protein folding". The protein folding problem remains one of the key unresolved issues in biochemistry [79, 80]. Specifically, despite massive research efforts and much recent progress, it is still unclear exactly how a disordered polypeptide chain spontaneously folds into a uniquely structured, biologically active protein molecule [81–84].

Glycerol has been used for many years as one of the common solvent additives to stabilize the activity of enzymes and the native structure (folded state) of proteins. The molecular structure of the glycerol was shown in Figure 4.1 [85]. Protein aggregation occurs after dilution into the solution, while glycerol as folding aids which can effectively inhibit aggregation during refolding. It is reported that the glycerol at 10% concentration not only completely prevented protein aggregation but also enabled the protein to return to its native state as well as to recover most of its native activity [86, 87]. The effect of glycerol on protein stability can be interpreted in terms of the solution properties of protein. In general, large cosolvent molecules are excluded from the solution shell near the protein's surface because of volume exclusion, and the protein is said to be preferentially hydrated [88,89]. It was experimentally shown that glycerol was excluded from the surface of wild-type protein in glycerol/water mixtures, confirming that the protein was preferentially hydrated. The protein surface area in contact with the solvent tends to be minimized by negative binding of glycerol. In most of the previous studies on the effects of glycerol, proteins were originally in the native state and the preferential hydration further stabilized them preventing the exposure of buried groups to the solvent [90–92].

4.4 Concentration Dependent Measurements

4.4.1 Glycerol Solution

As the first step towards the exploration of the interaction between the proteins with their solvent (glycerol) molecule, absorption coefficients of glycerol solution (without protein) in various concentrations range from 0 to 50% (vol/vol) were measured; the results of which are shown in Figure 4.2. The refractive indices were also determined but are not shown because they are less relevant to this work. The error

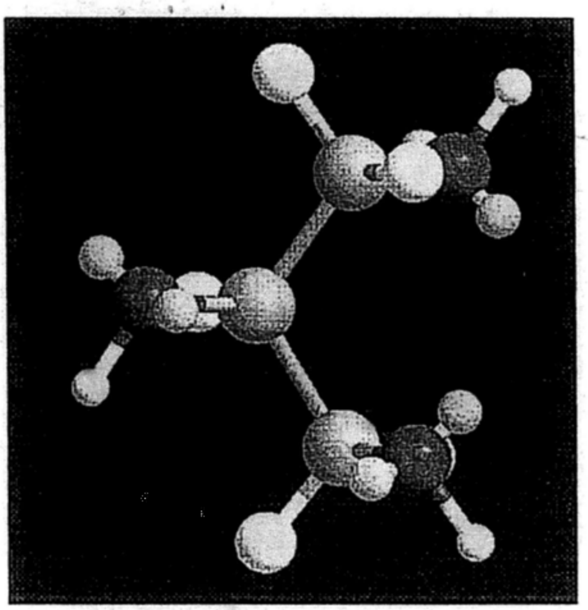

Figure 4.1: Glycerol (3D model), showing the atoms and the lone electron pairs (in pink) associated with the oxygen atoms (in red).

bars are generally small enough to distinguish between spectra of different concentration. Figure 4.3 shows the absorption coefficient dependence of the experimental values of the glycerol concentration at selected frequencies, 0.14, 0.43, 0.86 and 1.15 THz. Consistent with Beer's Law, in the binary glycerol/water mixture, the THz absorption of glycerol solutions varies linearly with concentration. It is important to note that because the terahertz absorption of glycerol is not as large as that of the solvent it displaces, the glycerol solution absorption reduces with increasing concentration of the solute (Figure 4.3).

4.4.2 Protein in Glycerol Solution

The PX-IgG and the FITC-IgG powder were dissolved in the glycerol solution (pure glycerol mixed with distilled water in equal volumes). The original protein solution was 0.8 mg/ml. Distilled water was used to dilute original solution to obtain concentration of 0.56, 0.4, 0.27 and 0.16 mg/ml, while five glycerol solutions with corresponding concentrations varying between 10% and 50% (vol/vol) were studied

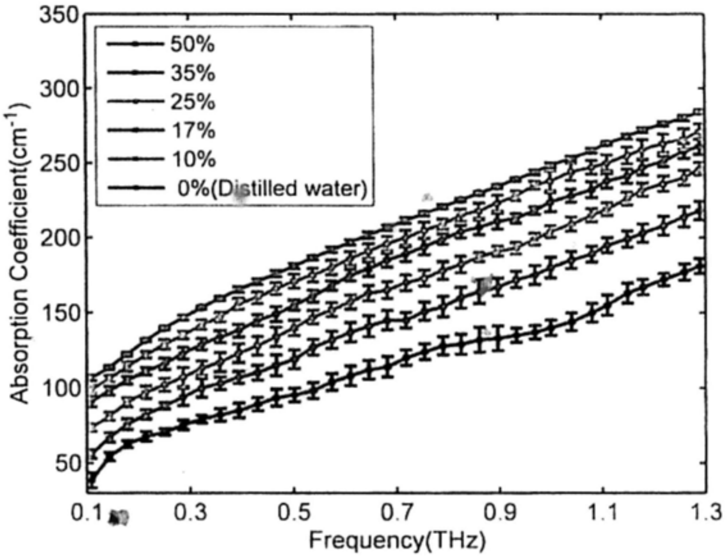

Figure 4.2: Absorption coefficient from 0.1 to 1.3 THz for distilled water, and mixtures that are 10%, 17%, 25%, 35% and 50% glycerol by volume. The general trend is that the absorption coefficient decreases as a function of increasing the glycerol fraction.

in this work.

In Figure 4.4 the terahertz absorption coefficient is plotted against concentration (0.16, 0.27, 0.4, 0.56 and 0.8 mg/ml) at selected frequencies at room temperature. We note that the absorption decreases from that observed for distilled water (zero point) and shows a sudden shift is observed to start from 0.16 mg/ml for the protein solution which contains 10% glycerol in solvent and then decline gradually from the 0.27 to 0.8 mg/ml protein solutions (namely from 17% to 50% for glycerol/water mixtures). When the whole frequency region is considered, this sharp change is very significantly at the higher frequencies (0.86 and 1.15 THz) than the lower ones (0.14 and 0.43 THz) and more obvious on PX-IgG (red marks) when compared to the FITC-IgG (green marks). This is not consistent with the linear changes in the glycerol solution based on the assumption of Beer's law shown in Figure 4.3, indicateing that it is not trivial to find that same reaction between solute (protein) and solvent (glycerol-water mixtures) happening in the ternary glycerol-water-protein

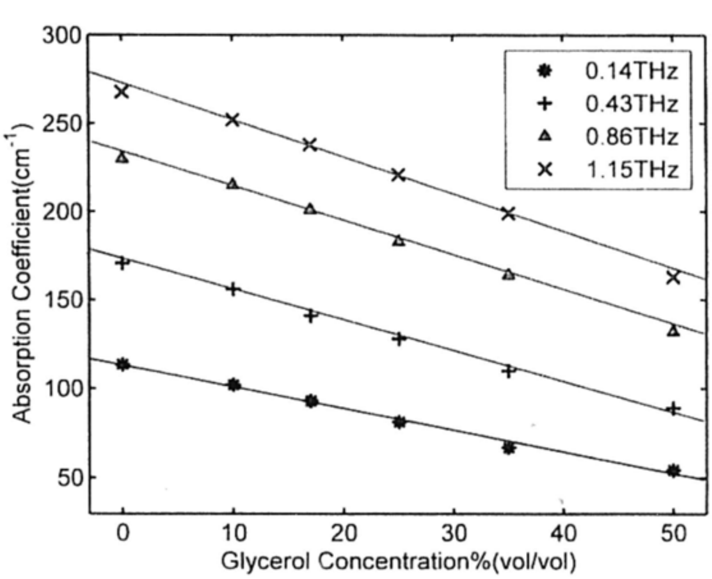

Figure 4.3: The terahertz absorption of the glycerol for several different frequencies varies linearly with solute concentration, consistent with Beer's Law. Of note, the observed absorption coefficient decreases with increasing solution concentration, indicating that the terahertz absorption of glycerol solution is not as great as that of the water it displaces.

system presented here.

The effect of various concentration of glycerol solution on protein refolding reaction was published by Roman V. Rariy in 1997 [87]. Their group declared that when an aqueous solution was used as a medium in the refolding phase, the refolding yield was 38 ± 1%, while in the solution of 20% glycerol, this yield increased up to two times of the aforementioned one and remained at this value after the glycerol concentration reached to 60%. We firstly compared the Terahertz absorption coefficient with the protein refolding yield in various glycerol solutions in order to give a convincing explanation for the sudden change in the Figure 4.4.

For comparison work, we used the distilled water data as a reference, and extracted the absorption coefficient of antibody protein PX-IgG and FITC-IgG at 0.86 THz, where

$$\Delta\alpha = \frac{\alpha_{\text{protein}} - \alpha_{\text{reference}}}{\alpha_{\text{reference}}} \tag{4.1}$$

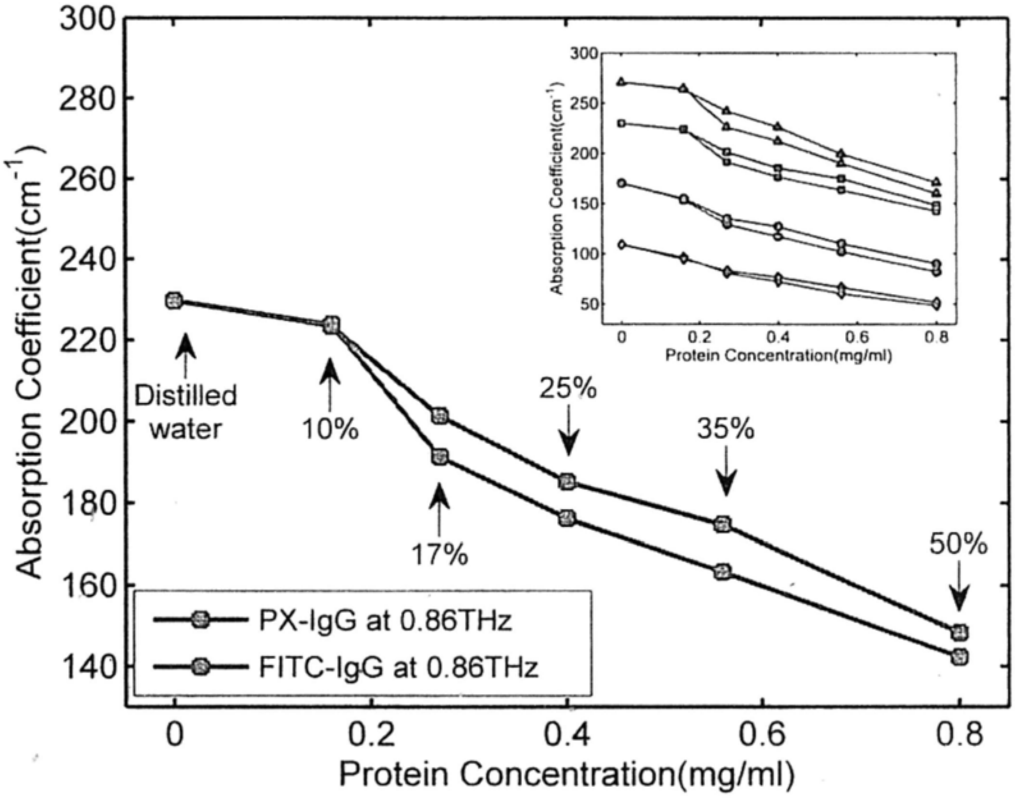

Figure 4.4: The terahertz absorption of antibodies solutions at 0.86 THz. Green marks present the fluorescein conjugated IgG (FITC-IgG) results and red marks present the peroxidase conjugated IgG (PX-IgG) results. Arrows present the various of the glycerol-water mixtures (0-50%,vol/vol). (Inset) Differences of the terahertz absorption coefficient are relative to the concentration of protein in the glycerol solution at selected frequency (▲-1.15 THz, ■-0.86 THz, ●-0.43 THz and ♦-0.14 THz).

The data obtained, presented in Table 4.1, are striking in that there is a small change in the absorption coefficient (2.5 for PX-IgG and 2.7 for FITC-IgG) in 10% glycerol solution when compared with the pure aqueous solvent, however the absorption coefficient increases sharply to 16.7 and 12.4 respectively when the concentration of glycerol solution reaches 17%, which concentration is similar with the published data (in 20% glycerol) which resulted in the two-time increasing of protein refolding yield. Furthermore, due to the increasing water content in the glycerol solution, the absorption coefficient increases gradually which has been proven by our previous work, even though the refolding yield of protein is held at the same level.

Glycerol solution, %(vol/vol)	Protein concentration (mg/ml)	$\Delta\alpha*$,%(cm^{-1}) PX-IgG	$\Delta\alpha*$,%(cm^{-1}) FITC-IgG	Refolding yield, %†
0	0	0	0	38±1
10	0.16	2.5	2.7	
17	0.27	16.7	12.4	
20		23.3		61±3
25	0.40		19.3	
40		28.9		61±4
35	0.56	38.1	23.9	
50	0.80		35.4	

Table 4.1: Comparison of the changes of absorption coefficient of PX-IgG and FITC-IgG at 0.86 THz and †enzymatic activity yield upon refolding of hen egg-white lysozyme in various glycerol-water mixtures

Considering this ternary glycerol-water-protein system, the protein fraction varies with the glycerol fraction simultaneously. In order to find if the sudden change of the $\Delta\alpha$ was caused by the effects of the protein or glycerol itself, we fixed the concentration of glycerol solution by 50% in the ternary system and diluted the protein solution to the same values as used in the previous measurement. The absorption coefficient of the fixed glycerol solution was considered as the reference this time. The results are shown in Table 4.1. When comparing the concentration dependence of the protein signal that, on average, the changes of absorption in the fixed glycerol solution increases gradually without sudden shift and that therefore, the shift in the Figure 4.4 must be due to the protein refolding reaction.

Glycerol solution, %(vol/vol)	Protein concentration (mg/ml)	$\Delta\alpha *$,%(cm^{-1}) PX-IgG	$\Delta\alpha *$,%(cm^{-1}) FITC-IgG
50	0.16	10.4	3.4
	0.27	10.7	4.7
	0.40	13.1	8.9
	0.56	14.0	9.5
	0.80	6.2	2.2

Table 4.2: The changes of absorption coefficient of PX-IgG and FITC-IgG at 0.86 THz in 50% glycerol solution

4.5 Energy Theory for Protein Folding

The protein folding process can be described as an energy landscape that looks like a funnel [93, 94], as briefly shown in Figure 4.5 [95].

The horizontal axis in Figure 4.5 describes conformational entropy of the protein structure, while the vertical axis describes the level of energy, enthalpy. Another vertical element, Q corresponds to the "percentage of residues of protein in the native conformation". The unfolded states (Q~0%) are characterized by a high degree of conformational entropy and energy. As the folding proceeds, the narrowing of the funnel represents a decrease in the number of conformations, and hence in entropy. Small depressions along the sides of the energy funnel represent semi-stable intermediates that can briefly slow down the folding process [95]. At the bottom of the funnel, the protein finally reaches the native, folded state (Q=100%) characterized by the lowest energy with minimum conformational entropy.

Conformational change and flexibility of protein will be reflected in the vibrational modes related to the large scale motion and these modes lie in the far infrared

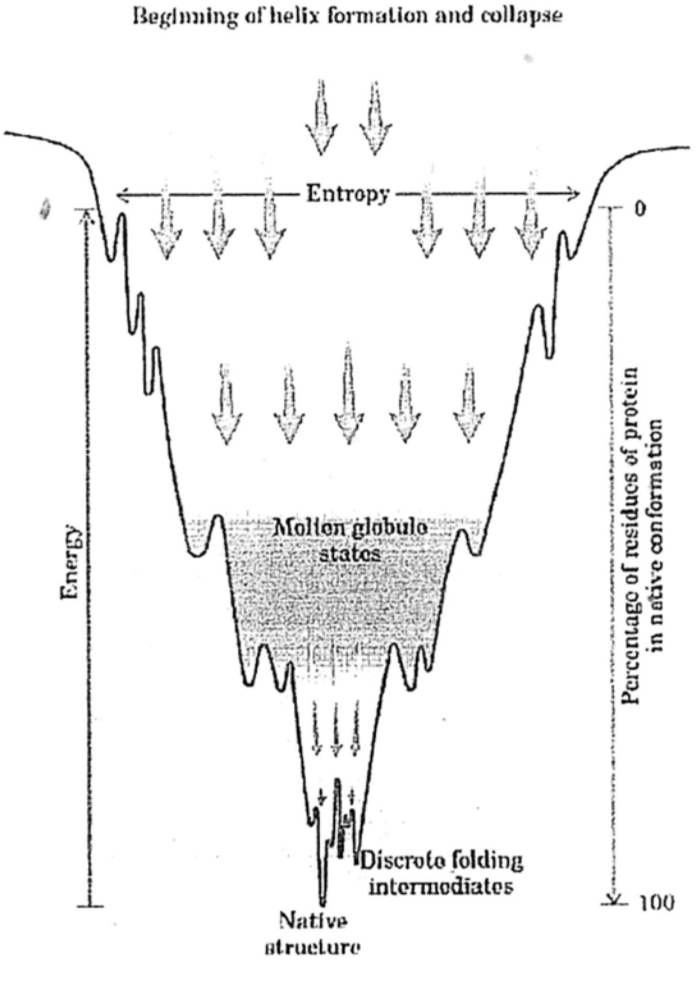

Figure 4.5: The funnel-like energy landscape model.

(FIR, λ=1-200 cm^{-1}, 0.03-4 THz) [96]. The terahertz region of the electromagnetic spectrum has energies of approximately 1-10 meV, which corresponds approximately to the frequency range of the transition between rotational states of molecules [97]. Other modes, such as breathing modes – hydrogen bond stretches between the two helices in DNA; modes due to conformational changes (known as soft modes); global stretching, twisting and vibrations in nucleic acids; and modes due to sugar repuckering have been found to be in this energy range [98, 99]. Most interestingly, it has been shown before that soft modes are important to the A to B conformational change in DNA [100].

Even though there exists fewer literature descriptions about how the protein refolding reaction can be affected at the terahertz energy level, our preliminary works show that the higher the energy level (or frequency) the more clear "sudden shift" effects happen in the biomolecule system.

4.6 Probing the Extended Dynamical Hydration Shell

4.6.1 Introduction

Hydrate water plays an integral role in the folding and function of proteins. Water molecules interact (or are highly correlated) with proteins on many length and time scales. Although the dynamics of the hydrate water occurs on the picosecond time scale, "slaving" [101] to fast solvent modes profoundly affects the slower but larger scale protein motions [102]. In return the protein influences the structure and dynamics of the surrounding water molecules [103]. Terahertz absorption spectroscopy of biomolecules fully solvated in water yields direct information on the global dynamical correlations among solvent water molecules. The terahertz absorption coefficient is even more sensitive to fast water dynamics than dielectric spectroscopy or IR spectral changes [104]. Yet, terahertz spectroscopy is experimentally challenging [105], because of the strong terahertz absorption of water.

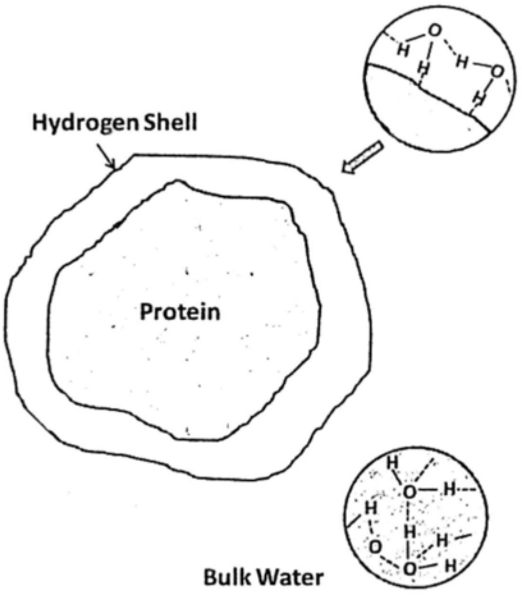

Figure 4.6: Schematic diagram of a hydrated protein molecule. The water molecules hydrogen-bonded with the protein molecule present in the hydration shell as well as the water molecules in the bulk hydrogen-bonded network are also shown schematically in the figure.

With the advent of powerful table-top terahertz sources, a new window between microwaves and the infrared is opening up onto the interaction of water molecules with proteins [106]. Even more, THz radiation is safe for biological samples because it is non-ionizing, unlike X-rays. Terahertz spectroscopy has been demonstrated as a new probe of the coupling between biomolecules and their hydration shells [107–110], because key large amplitude motions of water and biomolecules occur on the picosecond timescale – the typical characteristic time of terahertz spectroscopy.

4.6.2 Protein Dynamic Hydration Measurements

The terahertz frequency range probes the intermolecular collective modes of the hydrogen bonding network and some collective modes of the protein. It is reported that using a free electron laser, Plaxco *et al.* found that the terahertz absorption decreases linearly when large concentrations of protein are added to the solution

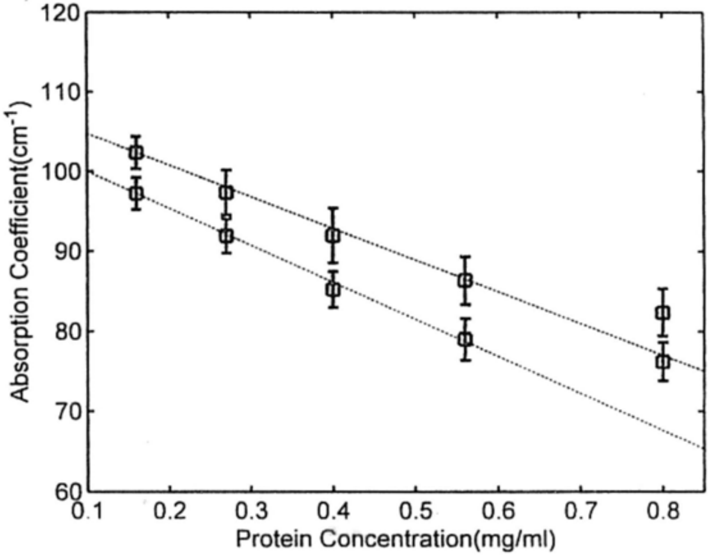

Figure 4.7: The terahertz absorption of antibodies in 50% glycerol solutions at 0.45 THz. Green marks present the fluorescein conjugated IgG (FITC-IgG) and red marks present the peroxidase conjugated IgG (PX-IgG). Terahertz absorption decreases linearly with the protein concentration increasing from 0.16 to 0.56 mg/ml before deviating to a lower gradient at the higher protein fraction.

[110]. Such behavior indicates that the solute molecules replacing the water have a lower absorption within this frequency range. It is to say a nonlinear dependence of the dielectric absorption coefficient on the solute concentration is predicted and originates from the mutual polarization of the liquid surrounding the solutes by the collective field of the solute dipoles aligned along the radiation field [111].

We determined the terahertz absorption coefficient α as a linear function of increasing protein concentration C_{protein} in the solvent volume V. We expect the proteins to be much less absorbing than the glycerol solution and so expect the absorption coefficient to decrease with increasing protein concentration. In Figure 4.7, the terahertz absorption determined at 0.45 THz for various concentrations of antibodies FITC-IgG (green marks) and PX-IgG (red marks) in 50% glycerol solutions is presented. Terahertz absorption decreases linearly with the protein concentration increasing from 0.16 to 0.56 mg/ml and presents deviation at the higher protein fraction. We use Equation 4.2 [112] to calculate the absorption coefficient of an ideal mixture and used the two component excluded volume model to fit $\alpha(\omega)$ vs. C_{protein}.

$$\alpha_{\text{ideal}}(\omega) = A_1 \alpha_{\text{protein}}(\omega) + A_2 \alpha_{\text{solvent}}(\omega) \tag{4.2}$$

where α_i is the absorption coefficient for each component, and the coefficient $A_1 = V_{\text{protein}}/V$ and $A_2 = (V - V_{\text{protein}})/V$. The absorption coefficient drops, leading to the non-monotonic, non-linear concentration dependence. The measured terahertz absorption deviates strongly from a linear decrease as shown in Figure 4.7. Although at higher concentrations it will decrease quasi-linearly as discussed in reference [109], such a non-monotonic, nonlinear behavior observed in Figure 4.7 cannot be explained just by a two component excluded volume model. The water layer around the protein molecule is known to exhibit distinct dynamical properties compared with bulk water. In Figure 4.7, nonlinear change can be explained as the beginning of overlap of the dynamical hydration shell around the protein molecule. Therefore, we continued our analysis in terms of individually determined absorption coefficients using a ternary component model (protein, hydrate water and bulk water), which assumes a distinct absorption coefficient of the water around the solute molecule due to the distinct properties of the solvation water [113]. In this model expressed by Equation 4.3, the ideal absorption coefficient is described as the volume-weighted of the absorption of the protein, the hydrate water, and the bulk water. The measured absorption coefficients of PX-IgG at 0.45 THz were fitted as a function of the protein concentration using nonlinear least-squares routine. By following the ternary component model, we can expect a turn at the concentration where the hydration shell starts to overlap. Furthermore, the separately fitted absorption coefficients for hydrate water is found to be increased by ~10 cm^{-1} at 0.45 THz compared with the bulk value at the same frequency; similar results have been discussed in reference [113].

$$\alpha_{\text{ideal}}(\omega) = A_1 \alpha_{\text{protein}}(\omega) + A_2 \alpha_{\text{hydration\_shell}}(\omega) + A_3 \alpha_{\text{bulk\_water}}(\omega) \tag{4.3}$$

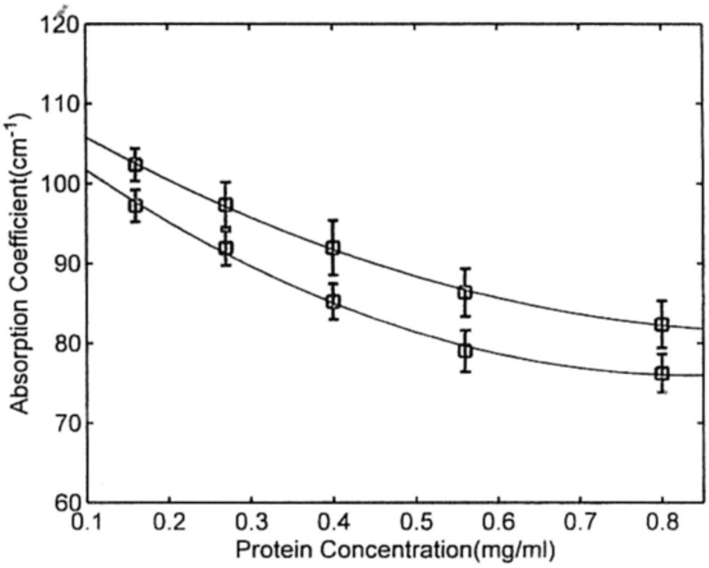

Figure 4.8: The terahertz absorption of antibodies in 50% glycerol solutions at 0.45 THz. Green marks present the fluorescein conjugated IgG (FITC-IgG) and red marks present the peroxidase conjugated IgG (PX-IgG). The solid line corresponds to the result of our fit also including hydrate water.

4.6.3 Size of Hydration Shell Evaluation

IgG antibodies are large molecules of about 150 kDa composed of 4 peptide chains. Typically they contain 2 identical heavy chains of about 50 kDa and 2 identical light chains of about 25 kDa. The enzyme (e.g. peroxidase) and the fluorophore (e.g. fluorescein) can be tagged on the IgG to become a labeled antibody [114]. If we assume each antibody molecule is either conjugated to a peroxidase or tagged to a fluorescein, the molecular masses for each PX-IgG and FITC-IgG would be approximately 200 KDa and 161 KDa respectively. Assuming the shape of the conjugated antibody to be a sphere, the concentration of 0.56 mg/ml would result in a radius of antibody R_{PX} of ~ 52.17 Å and R_{FITC} of ~ 48.42 Å. By comparing these to the radius of the bare IgG molecule (~ 48.42 Å, 160 KDa) [73], we found that the binding of native antibodies causes a decrease in the radius of about 3 Å for PX-IgG and 7 Å for FITC-IgG. This is induced by a significant change in the quaternary structure of protein [115]. Based on the hydration-free radius of gyration, which is estimated from small angle x-ray scattering data by Dumont *et al.* [115], we can directly deduce the maximum thickness of the hydration shell at this concentration to be 19.33 Å for PX-IgG and 24.08 Å for FITC-IgG. The above discussion is shown schematically in Figure 4.9. Similar values of the hydration shell have been reported by reference [116]. As the concentration of the antibodies increases, the hydration shells start to overlap and result in nonlinear absorption. Eventually, the hydration shells overlap fully and are saturated such that it is not possible to increase the concentration further. This occurs at much higher concentrations than those which we investigated in this study. A greater variety of concentrations would ideally be investigated in further work.

	MM(KDa)	R(Å)	DHS(Å)
PX-IgG	200	52.17	19.33
FITC-IgG	161	48.42	24.08

MM-molecular mass; R-radius of antibody; DHS-depth of hydration shell.

Table 4.3: Comparison of molecular mass, average protein-protein center of mass distance and depth of hydration shell of PX-IgG and FITC-IgG

4.7 Terahertz Dielectric Properties

Dielectric spectroscopy is a useful method for the investigation of the structure and dynamics of protein molecules in solution. The intrinsic time window of dielectric spectroscopy in the range from MHz to THz (the time scale is extended from microseconds down to 0.1 ns [117]) is very appropriate for biological processes, because characteristic conformational changes and catalytic actions occur with corresponding relaxation times. In aqueous solution the relaxation contributions of solute and solvent appear well separated in the dielectric spectrum. The low frequency contributions are essentially caused by the protein, while the high frequency contributions result clearly from the solvent molecules. Due to conformational changes

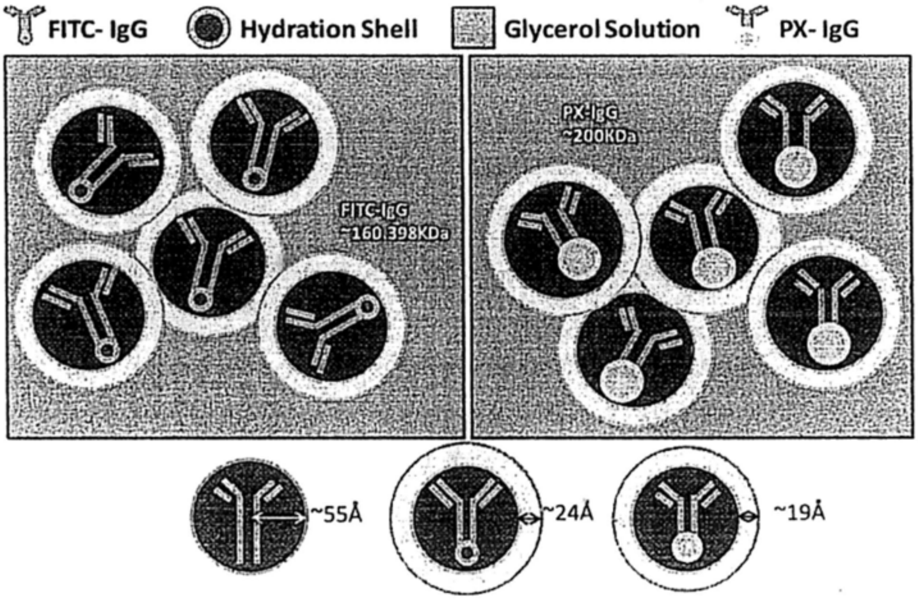

Figure 4.9: Schematic diagram for overlap of the hydration shells for FITC-IgG and PX-IgG in the glycerol solution.

on unfolding which result in changes in the rotational relaxation times and/or the apparent dipole moment, dielectric spectroscopy can provide information about the denaturation process of proteins. As a continuation of our previous work in Section 4.5, we report here the dynamic dielectric properties of antibody PX-IgG and antibody FITC-IgG in aqueous glycerol solution. The present study was intended to provide additional insight into the molecular mechanism of the stabilizing action of glycerol by analyzing specifically the dielectric relaxation of the water and protein moieties.

4.7.1 Cole-Cole Plots

Absorption coefficients of the distilled water, pure glycerol and glycerol-water mixed by equivalent volume are shown in Figure 4.10. The signal-to-noise ratio decreases rapidly above 1.3 THz, owing to a sharp drop in the intensity of high frequency components of the pulse, and to the high absorption of the samples.

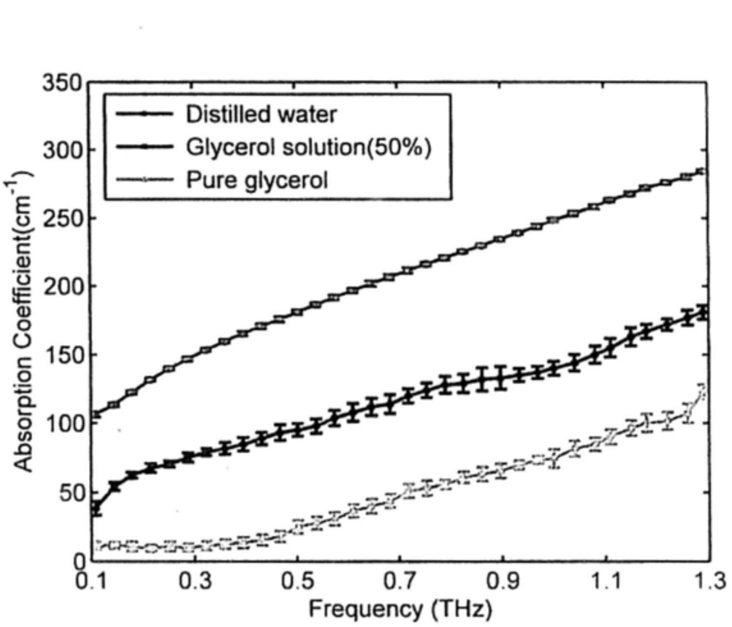

Figure 4.10: The absorption coefficients of distilled water (blue solid line), pure glycerol (pink dash-dotted line) and a mixture of glycerol/water by equivalent volume (black short dashes line)

Figure 4.11 shows the dependence of the absorption coefficients on the concentration of the antibodies PX-IgG and FITC-IgG. Terahertz absorption spectra are very sensitive to crystalline structures [118, 119], but the liquid protein form of FITC-IgG lacked any distinct peaks in the spectral region studied. However, the PX-IgG exhibited spectral peaks at 0.76 and 1.18 THz approximately. As expected, these peaks were submerged with increasing water content. The absolute overall absorption increases with decreasing protein concentration, since terahertz is absorbed strongly by the background water. When we compare the absorbance of two antibody proteins at the same frequency, the absorbance of FITC-IgG is consistently higher than that of PX-IgG.

The far-infrared dielectric properties are dominated by vibrational modes of the intermolecular hydrogen bonded network [120]. The dielectric constant of water is higher than that of almost all other liquids since the hydrogen bonding produces a higher volume polarizability [121, 122]. Thus in Figure 4.12 the complex permittivity of pure glycerol (pink line with squares) is consistently lower than that

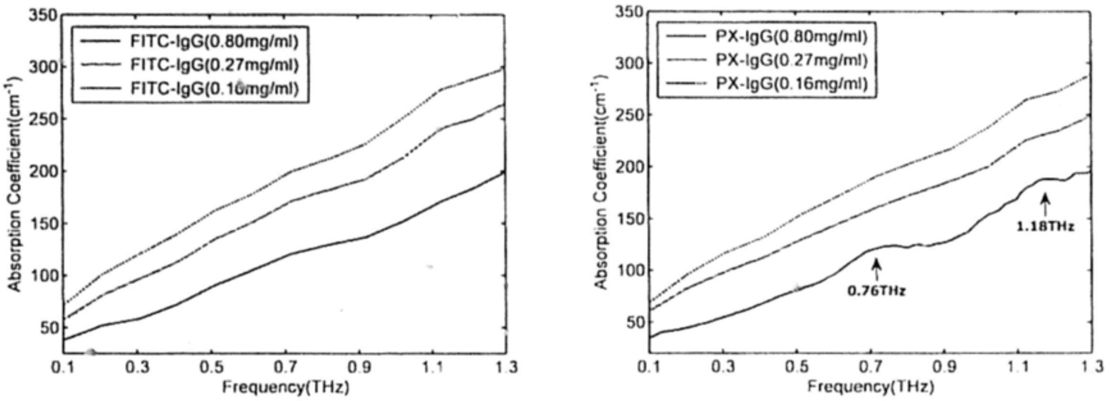

(a) (b)

Figure 4.11: The absorption coefficients of (a) FITC-IgG and (b) PX-IgG in glycerol solution at concentrations: 0.16 mg/ml (blue dash-dotted line); 0.27 mg/ml (black short dashes line); and 0.8 mg/ml (red solid line).

of water (blue line with circles) for both real and imaginary parts. As expected, when the glycerol is mixed with the water, the resulting dielectric response (black line with stars) lies between the constituent responses. Alternatively we can think of this as the glycerol lowering the dielectric properties of the water by introducing glycerol/water interactions which decrease polarizability.

The antibodies under investigation are stored in a glycerol-water solution. Therefore in Figure 4.13 we compare measurements of the antibodies in solution with the glycerol-water solution. This illustrates that each antibody affects the permittivity of the glycerol-water solution differently. When the PX-IgG is added to solution, the Cole-Cole plot (real part vs. imaginary part of the complex permittivity) is significantly shifted to the left. In contrast, when FITC-IgG is added to the solution, the Cole-Cole plot is shifted towards to the right.

We extracted the dielectric constant and the dielectric loss spectrum of the protein solutions to indicate the effects of these two antibodies. In Figure 4.15(a), when comparing the dielectric constants, PX-IgG has a higher dielectric constant than FITC-IgG over the whole frequency range. The double peaks corresponding

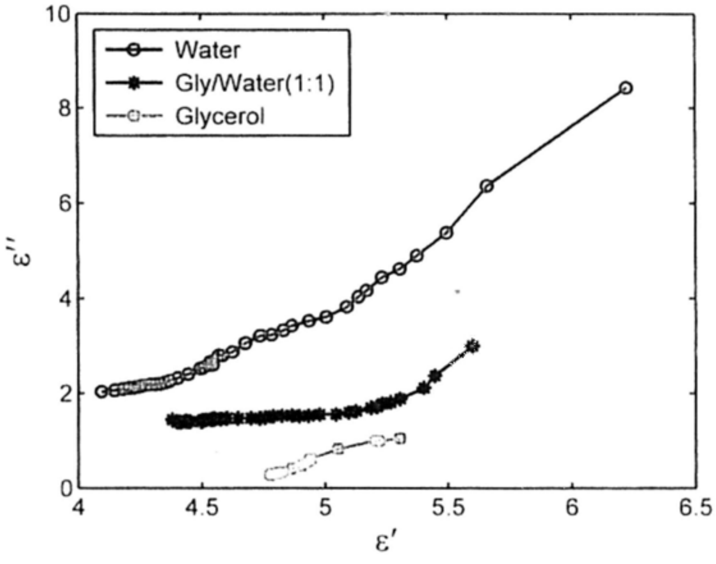

Figure 4.12: Real part (ε') and imaginary part (ε'') of the complex permittivity for distilled water, pure glycerol and glycerol/water solution (mixed by equivalent volume).

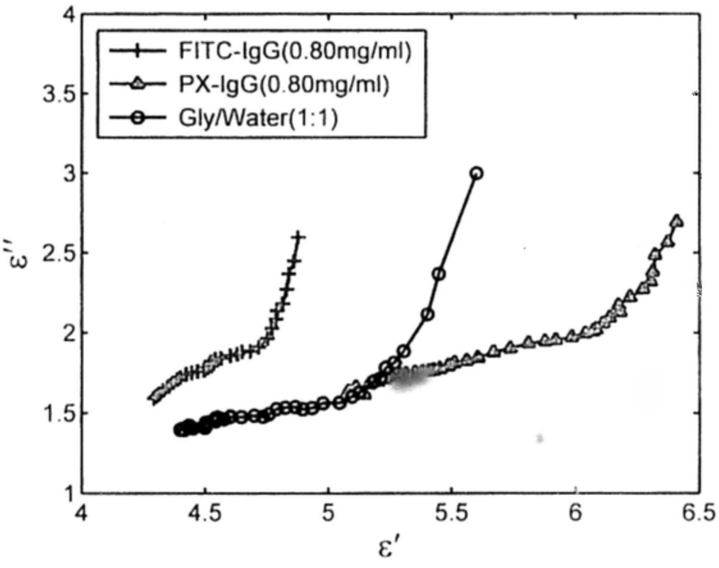

Figure 4.13: Cole-Cole plots of the complex permittivity for the water/glycerol mix (black line with circles) and peroxidase conjugated IgG (PX-IgG) (red line with triangles) and the fluorescein conjugated IgG (FITC-IgG) (green line with crosses) dissolved in the water/glycerol solution.

to the absorption peaks location at 0.76 and 1.18 THz respectively are more pronounced in Figure 4.15(b) for the imaginary part of the dielectric coefficient than in Figure 4.11(b) for the absorption coefficient.

4.7.2 Detection of Charged Proteins Solution

It is known that the effect of the dynamic depolarization, which is proportional to the solution conductivity, depends only on the dielectric properties of the solution [123]. A charge that moves in the driving electric field (the terahertz pulse) causes the surrounding solvent molecules to rotate [124]. The direction of this rotation has an opposite sign compared to the direction of the electric field, hence resulting in a decrease in the dielectric relaxation strength. It is reported that IgG fractions are negatively charged and that addition of fluorescein renders them more electronegative [125], while in the studies of John E. Herrmann *et al.* [126], through the use of gel electrophoresis they found that peroxidase has a positive charge. Hence the differences between antibody PX-IgG and FITC-IgG observed in their dielectric spectra is due to the type of the charges found in their hydrogen-bonded antibody networks. The variation of $\alpha'(\omega)$, however, shown in Figure 4.15(a), proves unambiguously that positively charged PX-IgG aqueous networks significantly enhance the dielectric relaxation strength. Dielectric spectra consist of many bands originating from vibrational modes [127], the only differences between the molecular structures for the two antibodies are in the conjugation pattern; namely whether it is peroxidase or fluorescein conjugated. FITC is the fluorescein base molecule functionalized with an isothiocyanate reactive group (-N=C=S) at one of two hydrogen atoms on the bottom ring of the structure. This derivative is covalently coupled to primary amine groups on proteins of the immunoglobulin, while sugar residues present on peroxidase can be oxidized to produce aldehydes which react with primary amines on antibodies [128]. The conjugation scheme for FITC and peroxidase reaction with a amine on immunoglobulin is shown in Figure 4.14.

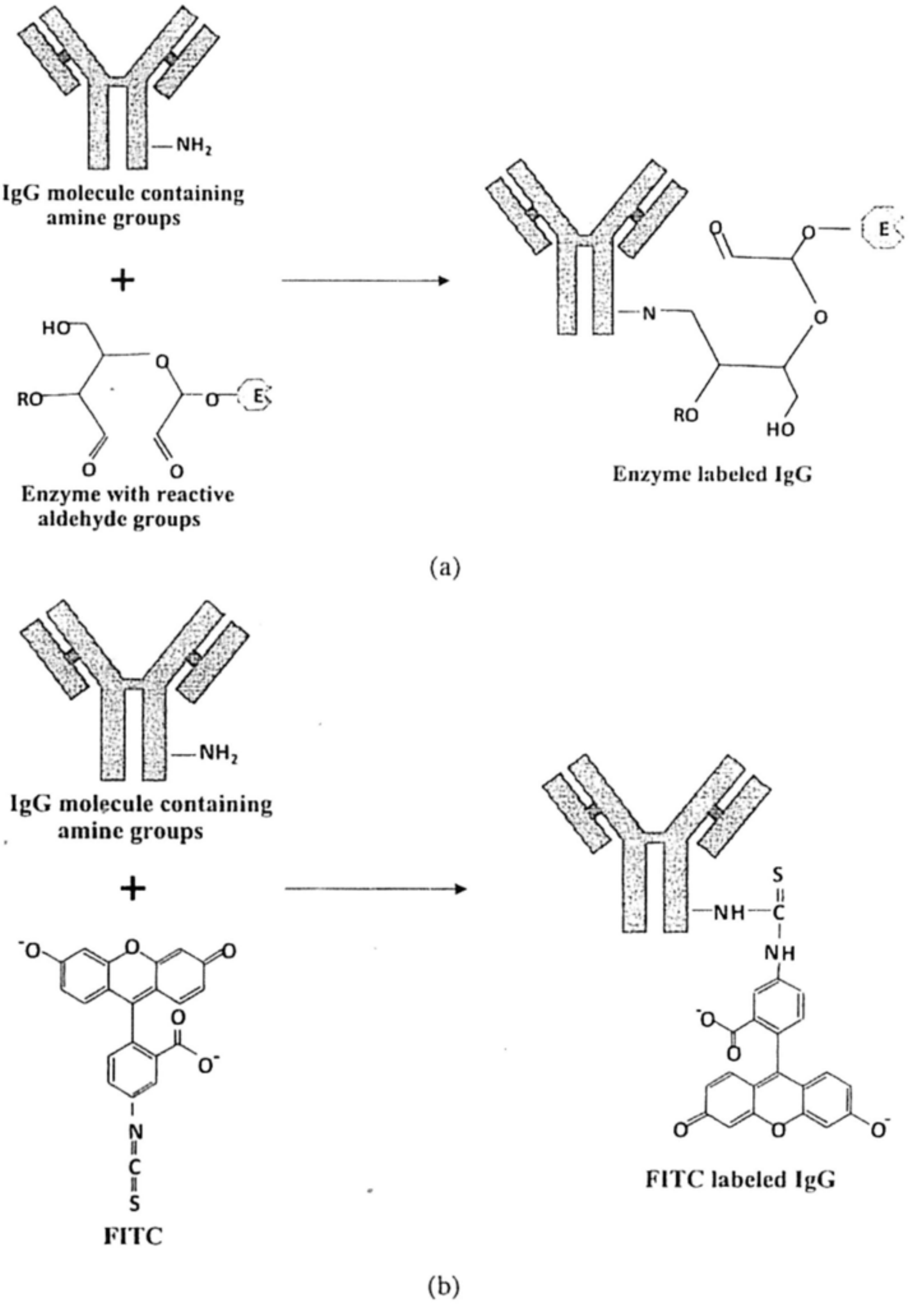

Figure 4.14: Conjugation scheme for (a) FITC and (b) enzyme reaction with a primary amine on immunoglobulin.

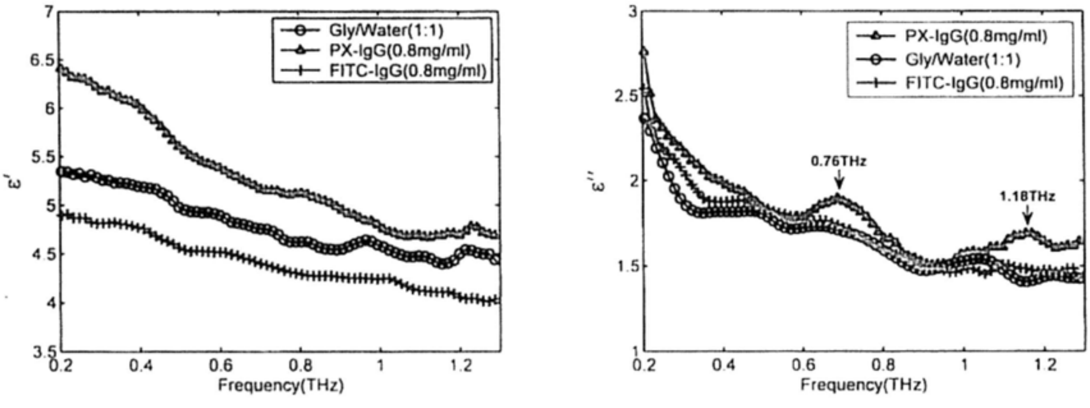

(a) (b)

Figure 4.15: (a) Dielectric constant spectra and (b) dielectric loss spectra of water/glycerol mix (black line with circles), peroxidase conjugated IgG (PX-IgG) (red line with triangles) and the fluorescein conjugated IgG (FITC-IgG) (green line with crosses) dissolved in the water/glycerol solution at the concentration of 0.8 mg/ml in the frequency range of 0.1-1.3 THz.

Dielectric relaxation spectroscopy is an appropriate method to characterize the dynamics of polar liquids and their solutes. Here the (negative) imaginary part $\alpha''(\omega)$, the dielectric loss, is of particular interest, since it is related by the general fluctuation-dissipation theorem to the spectrum of polarization fluctuations of a dielectric sample that originate from thermally induced translational stochastic motions of charge carriers and the rotational tumbling motion of dipolar entities. Besides, due to the relative broadness of the dielectric spectra these different relaxation processes will only be resolved adequately if the polar molecules under investigation differ significantly in size. This is the case for the ternary glycerol-water-protein system studied here. The low frequency contribution to relaxation can be assigned unambiguously to the motion of the protein while the high frequency contributions result from the solvent [129]. It is obvious from Figure 4.15(b), that in contrast to the protein solutions, the pure glycerol-water solvent exhibits a noticeable loss contribution in the low frequency region (typical from 0.2 to 0.4 THz). However, the reason for these somewhat higher peaks for PX-IgG (red line with triangles), whether it be caused by the difference of the binding site for the tagged label on the IgG, or the unknown chemical structure, has not been determined yet. The spectra of the solvent of the protein (black line with circles) and FITC-IgG (green line with crosses) do not show any clear band structure; they only decrease monotonically with frequency.

4.8 Summary

The dielectric response is associated with the collective vibrational modes of protein tertiary structure and sensitive to the conformational changes of the protein molecules due to the structure [63]. In this study we compare the effect of polar liquids in the far-infrared absorption spectrum of two types of normal antibodies from 0.1 to 1.3 THz. The complex permittivity response of polar liquids and the protein solutions have been measured as a function of frequency and presented by Cole-Cole plots. The response is strongly associated with the polarization arising from the polar liquids' network of hydrogen bonding. The size of the hydrogen shell was evaluated in this study also. The presence of different antibodies affected the solution uniquely such that the dielectric properties of each solution containing an antibody were sensitive to the conjugation of the antibody added and that charged protein solution hydrogen-bonded networks play an important role in determining the dielectric properties detected by terahertz spectroscopy. Therefore terahertz spectroscopy may be useful for medical diagnoses where the presence of antibodies is indicative of disease.

Chapter 5

Protein Measurement Using THz-TDS Transmission System

We are witnessing the increased interest in understanding the biomedical application of the electromagnetic radiation in the THz- frequency range as the regime is absolutely safe for the human body. Of particular interest is the molecular response of biological material to electromagnetic radiation. It has been shown that the THz spectra of many small biomolecules such as nucleobases and nucleotides [130] as well as polypeptides [131] show characteristic features that can be used to identify the individual molecules. In Chapter 4, the different properties of two IgG antibody molecules were identified using THz-TDS reflective system. Transmission spectroscopy is best suited to study liquid phases having a very high signal-to-noise ratio at low frequencies. In this chapter, another two protein molecules are investigated using a transmission system and our aim is to detect and characterize the cancer marker protein (HER2/neu) based on the sensitivity of terahertz technology to modes of molecular vibration.

5.1 Introduction

Various authors have predicted that proteins have vibrational resonances in the terahertz frequency range [130, 131]. These modes are thought to be essential for conformational dynamics necessary for protein function. In addition to these modes being of fundamental interest for the understanding of biological processes, their direct relation to the protein backbone structure suggests the spectrum may be used to determine the presence of a particular protein. Though larger molecules sometimes lack specific signatures, subtle changes in the absolute value of the absorption coefficient can be used for biomedical diagnostics [132–134]. Further research shows that the peptide HER2/neu is a prognostic breast cancer marker assayed in tissue biopsies from women diagnosed with malignant tumors. HER2/neu protein is over-expressed in about 20-30% of malignant breast tumors and has been used in postoperative follow-up evaluation as an indicator of patient relapse. So detecting and determining the properties of this protein possess very important diagnostic value for breast cancer treatment. Recognizing the overall oncological importance of the HER2/neu oncogene, a novel study was conducted and found the soluble HER2/neu protein present not only in serum but also in saliva. The study also suggested that the serum and saliva soluble HER2/neu concentrations increased in the presence of carcinoma of the breast [135].

5.2 Sample Introduction

HER2/neu (also known as ErbB-2) stands for "Human Epidermal growth factor Receptor 2" and is a protein giving higher aggressiveness in breast cancers. The molecular formula of HER2/neu is $C_{42}H_{77}N_9O_{11}$ and molecular weight is 884.12 Da. Figure 5.1 shows the structure of this molecule (the picture is supported by GenScript Corporation).

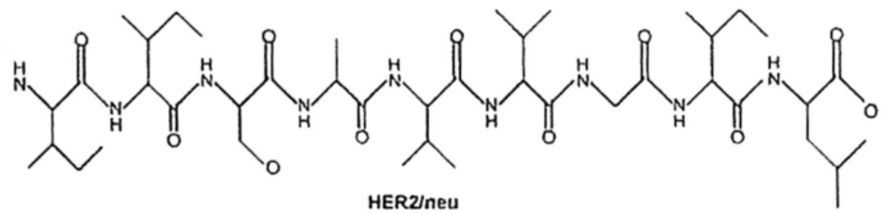

Figure 5.1: Structure of HER2 molecule (from GenScript Corporation).

The lysozyme structure was shown in Figure 5.2 [136]. The infrared and far-infrared spectra of lysozyme are relatively well known. Furthermore, hen egg white lysozyme (HEWL) which is slightly different from the human lysozyme presenting in human body liquids (tears, but also in small amounts in salvia) was also investigated as an experimental substance. The molecular weight of HEWL is approximately 14.7 kDa. HEWL has been wildly investigated and we have known clearly that it is a globular $\alpha + \beta$ protein with approximately 45% of α-helix type secondary structure and ~20% of β-sheet structure. In addition it has ~25% various turn conformations that generally exist in globular proteins and ~13% of unordered or "random coil" secondary structure [137].

5.3 Solution Studies

5.3.1 Sample Preparation and Methodology

In order to provide a more sensitive and comfortable detection method of THz technology in biomedical applications, we will concentrate on broad bandwidth THz technologies for spectroscopic identification of protein HER2/neu in both the liquid and solid phase. Broadband detection schemes can help to distinguish between richly structured spectra and therefore enable identification by comparison with the entries in a database.

For the solid phase measurement, the sample powder was pressed into a PE

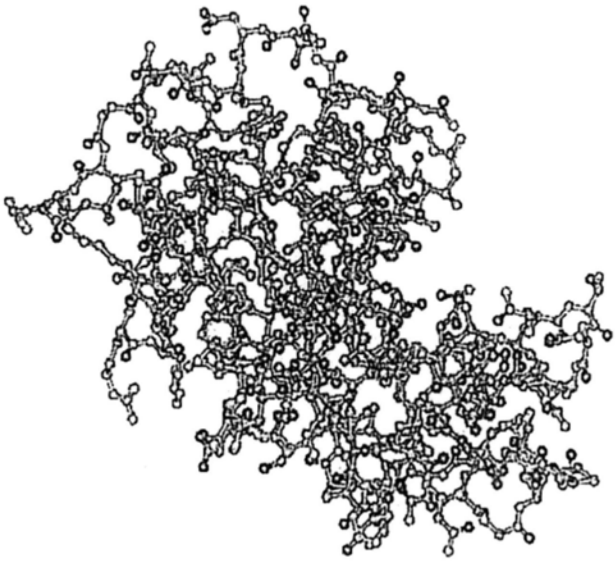

Figure 5.2: Ball-and-stick representation of the lysozyme structure. In this view, all protein atoms are shown as balls, and bonds between atoms are shown as a stick. Carbon, nitrogen, oxygen and sulphur atoms are coloured grey, blue, red and yellow, respectively.

matrix in order to produce mechanically stable pellets yet avoiding increased absorption losses that would be too strong at higher frequencies. PE, shown in section 5.4.3, is typically used to decrease the concentration of the sample material – thus increasing the accessible bandwidth of the system – while being itself nearly completely transparent to THz radiation; while for the protein-liquids sample preparation, samples were diluted in an buffer solution with a pH matching the pH of salvia in different concentration and temperature in the transmission spectroscopy. Temperature and concentration dependent measurements are also used on the solid sample.

The advantage of transmission spectroscopy in the liquid phase is a very high signal-to-noise ratio at low frequencies, however one drawback is that only very thin layers of the sample liquid can be measured, due to the high absorption properties of liquid water. Therefore, freezing the sample could bring advantages, in particular at higher frequencies, as ice is relatively transparent for THz radiation (at least compared to liquid water).

To prepare our samples, we first dissolved the HER2/neu (c-erbB-2) powder (GenScript Corporation, Piscataway, USA) into pH 7.0 buffer at a concentration of 20 mg/ml. The buffer, composed of 3.54 g potassium dihydrogen phosphate and 14.7 g disodium hydrogen phosphate per litre, was purchased from Sigma-Aldrich (USA). A drop of solution was deposited into the sample cell and the clean homogeneous parallel plate was used as a reference (refractive index ~1.53). Solutions were used to ensure that the hydration of the system was constant, which was frozen in a cryostat model. The experiment was performed under the varied temperature 15, 80, 200, 263, 273, 283 and 294 K respectively.

Lysozyme (Sigma Aldrich, St. Louis, MO) which is present in human body liquids (e.g. tears, and in small amounts in salvia) was prepared in the same way which was considered as a very good candidate for our study.

5.3.2 Temperature Dependence and Anomalous Temperature Shift

The far-infrared modes of the small molecules typically show a temperature dependence that can be explained by the anharmonicity of the vibrational potential [8]. However, in the course of this work, we discovered a few cases where modes showed a distinct shift when the sample was cooled.

The first time we present the temperature-dependent measurements of the absorption response in the case of HER2. Figure 5.3 shows the full temperature dependence of HER2 in the frequency range between 0.2-1.4 THz. Below a critical temperature of 263 K, the absorption coefficient spectrum presents an anomalous down shift. As discussed before, in large scale protein systems, there has been no observation of narrow band vibrational absorbances at terahertz frequencies when the temperature is above freezing point. However, the fluctuation in absorption for temperatures below 263 K suggests the possibility of an absorption peak at 0.58

THz (Figure 5.3(b)). There appears to be no calculated data concerning the dielectric behavior of HER2 in far-infrared range within the literature, therefore it is challenging to demonstrate whether vibrational motions relating to a resonant response arising from structural vibrational modes exist at this frequency or not. As seen in the Figure 5.4(a) the absorption coefficient rapidly increases above 263 K. This rapid increase is not present in measurements of pure buffer, demonstrating that the change in dynamics is in the protein. One does not expect a temperature dependence in the vibrational density of states for the harmonic approximation. If we allow for some anharmonicity we might expect a slight change in the absorbance as the temperature increases, but not a rapid increase as is observed. Joseph R. Knab [138] has described the temperature-dependent measurements (approximately from 90 K to 260 K) of the dielectric response for hen egg white lysozyme (HEWL) solution. The rapid increase of the absorption coefficient presented when the temperature increased near 200 K which is very similar comparing with our HER2 study shown in Figure 5.4(b). They suggest that this temperature transitions are possibly linked with hydration [138]. Here, we measured the expanded broad temperature range start from 15 K to 294 K. What is more, another temperature transition point appears at 273 K as shown in Figure 5.4(c). We know that all proteins have an optimum temperature at which they are able to operate. A temperature which is unsuitable for the proteins may cause it to denature into smaller peptides, or simply change shape due to the alteration of bond energies, resulting in broken or reformed bonds elsewhere in the amino chain. Briefly, the terahertz response is mainly determined by the relaxational response of side chains within the protein and the energy barriers for these motions are hydration dependent which can be denoted by temperature.

5.3.3 Harmonic and Anharmonic Oscillators

The harmonic oscillator is the most fundamental concept used to describe vibrations in atomic systems. A complicated molecule or crystal is usually approximated

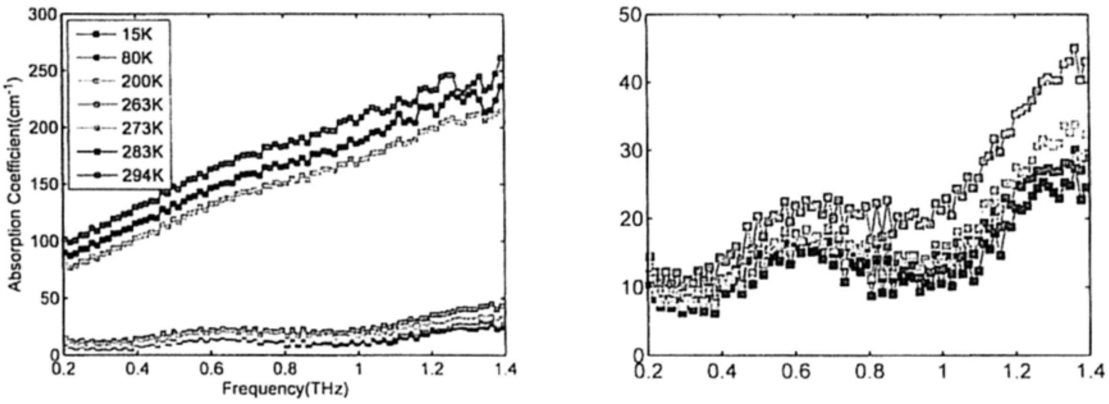

(a) (b)

Figure 5.3: (a)The absorption coefficient spectrum at various temperatures for HER2 solution. (b) The frequency dependence absorption coefficient at 263, 200, 80 and 15 K. The legend is the same for both plots.

by a set of individual harmonic oscillators. In an oscillating physical system vibrational motion occurs about a local minimum of the potential energy surface. The harmonic oscillator model can be applied to vibrational motion in molecules in the following manner: In a diatomic molecule for example, the vibrational potential would be centered around the equilibrium internuclear distance and the correct mass in the one-dimensional oscillator description is the reduced mass of the system. In polyatomics and in molecular crystals, the equilibrium position actually corresponds to the equilibrium positions of all the atoms while the one-dimensional translation coordinate corresponds to a particular collective motion of the atoms, a so-called normal mode. The vibrational spectrum can be understood in terms of excitations of (harmonic) normal modes of the system. A purely quadratic potential function as in the case of the harmonic oscillator becomes infinitely large, which is unsatisfactory for the description of real molecules, which have finite dissociation energies. Therefore real vibrational potentials are anharmonic. In fact, as the energy increases the displacement becomes larger. The chemical bond lengthens as the system is placed in increasingly higher vibrational states, which is the reason

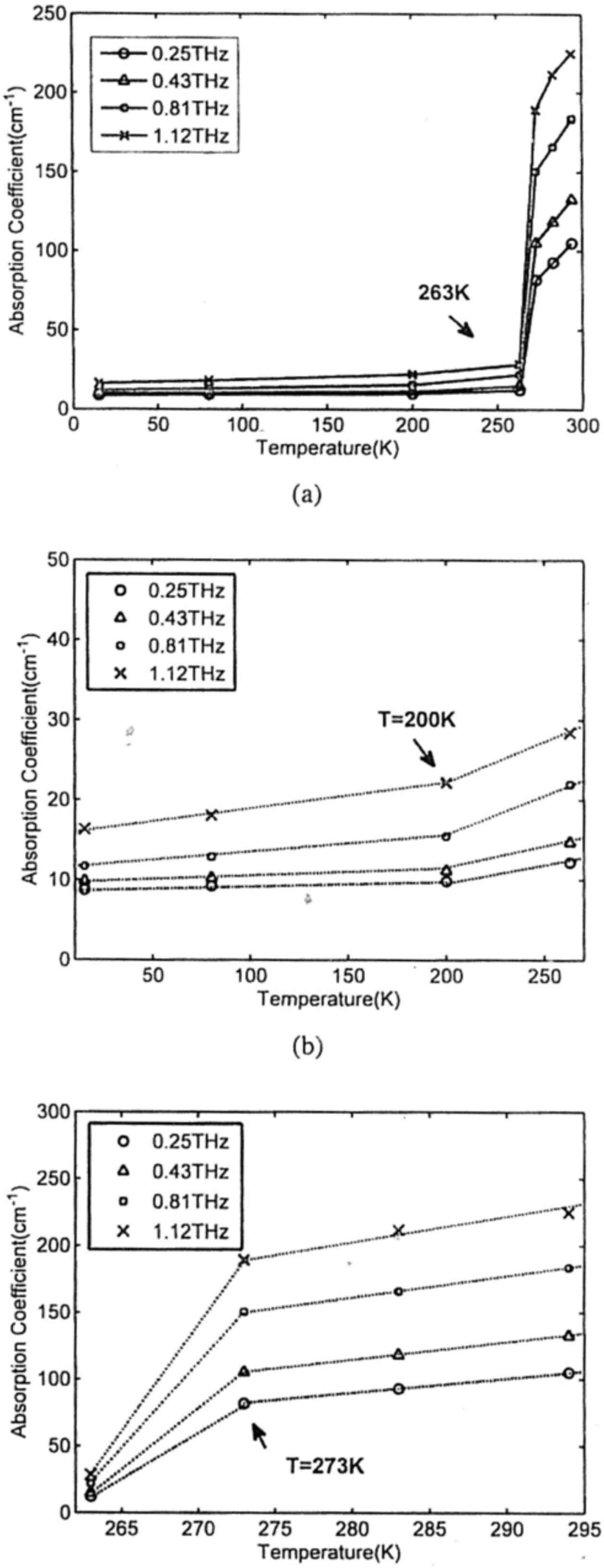

(a)

(b)

(c)

Figure 5.4: Temperature dependence of the measured absorption coefficient for HER2 solution. (a) Temperature dependence measurement at 0.25, 0.43, 0.81 and 1.12 THz. (b) Absorption coefficient spectrum at 263, 200, 80 and 15 K. (c) Absorption coefficient spectrum at 294, 283, 273 and 263 K.

for thermal expansion of solids. And finally, the energy spacing between each different eigenstate is no longer a constant. So, the effect of anharmonicity is that the spacing between energy levels becomes smaller as the vibrational quantum number increases and the energy approaches the dissociation limit.

5.3.4 Temperature Dependence

The total absorption intensity is proportional to the difference between the number of molecules in the initial and final states. The thermal populations of the individual states are related by Boltzmann-factors, therefore the absorption intensity for a transition from i to $i + 1$ is

$$I \propto N_i - N_{i+1} = N(e^{-i\frac{h\upsilon}{kT}} - e^{-(i+1)\frac{h\upsilon}{kT}}) \tag{5.1}$$

where N is the number of molecules in the sample, k is Boltzmann's constant and T is the temperature. Markus Walther [39] shows the relative populations of the vibrational levels for a mode at 1 THz at 10 K and 300 K. Whereas at 10 K nearly all molecules populate the ground state, at room temperature a considerable fraction populates levels up to $i = 10$ and beyond. Therefore at low temperatures only fundamental absorption from the vibrational ground state occurs, whereas at higher temperatures hot band absorption from higher levels also contribute. Since the thermal energy kT at room temperature corresponds to a vibrational energy of ~6 THz, the thermal distribution plays a prominent role in the THz regime.

For a harmonic oscillator no temperature effect on the absorption spectrum appears. However in an anharmonic potential, where the transition energies decrease with increasing quantum number, the center of the absorption shifts to lower frequencies as the temperature rises. Since this frequency shift depends on the anharmonicity of the underlying potential, one can in principle infer the degree of anharmonicity from the temperature dependence of the absorption profile. As a consequence of the thermal population of higher vibrational levels and the anharmonicity of the potential functions the average displacements increase at higher

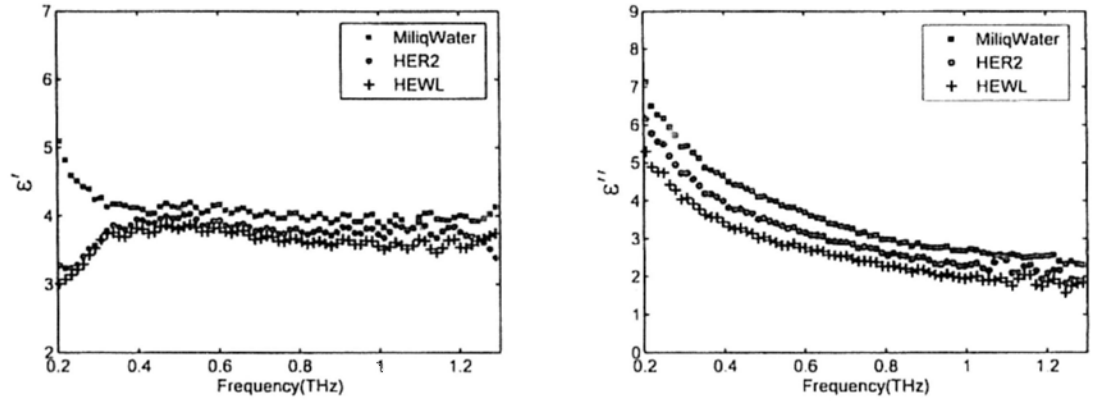

(a)

(b)

Figure 5.5: Real (a) and imaginary (b) parts of dielectric properties for bulk water, HER2 and HEWL.

temperatures. Therefore the interatomic or intermolecular distances also become larger, leading to a volume expansion of most substances when temperature is increased. In practice, we observe temperature-dependent changes of the absorption spectrum of HER2/nue due to the interplay of different intermolecular forces.

5.3.5 Dielectric Spectral Signatures

Figure 5.5 provides a good comparison of a dielectric dispersion exhibited by aqueous solution for HER2 (red dots) and HEWL (green crosses) at a concentration of 5 mg/ml at room temperature. The solvent bulk water was also determined and is shown as the blue squares in Figure 5.5. Real and imaginary parts of frequency dependent dielectric properties were extracted. The distinct dispersion region is apparent: the orientational relaxation of the solvent molecule can clearly be characterized, which is higher than solute molecule over the whole frequency range. Since the hydrogen bonding produces a higher volume polarizability, which is mentioned in chapter 4, the dielectric constant of water is higher than that of almost all other protein solutions.

A simple model, which can be used to describe the dielectric relaxation of a protein molecule with a permanent dipole moment, is to consider the dipole to be a rigid sphere whose rotation in response to an imposed electric field is opposed by frictional interaction with the surrounding viscous medium [139]. The relevant relaxation time for the orientation of such a sphere is

$$\tau = \chi / 2\kappa T \tag{5.2}$$

where χ is the molecular friction coefficient, which relates the torque exerted on the dipolar molecule by the applied electric field to the molecule's angular velocity, and κ is the Boltzmann constant. If we consider the dipole to be equivalent to a rigid sphere of radius a rotating in a Newtonian hydrodynamic fluid of macroscopic viscosity η, the Stokes-Einstein relation gives $\chi = 8\pi\eta a^3$ so that the relaxation time is

$$\tau = 4\pi\eta a^3 / \kappa T \tag{5.3}$$

Furthermore, if we assume that the molecular volume (and hence radius) of a globular protein is directly proportional to its molecular weight, then by substituting for the radius in Equation 5.3 we have

$$\tau = 3M\eta / N_A \rho \kappa T \tag{5.4}$$

where ρ is the average density of the protein molecule. The viscosity η of water at 298 K is 8.9×10^{-4} Nsm^{-2}. As a typical protein density, we can take the value of 1.39 g cm-3 obtained by Kuntz [140] for carboxypeptidase. Thus, as a rough working guide, $\tau = 0.78$ M ns. On this basis, for HER2 (M = 0.88 kDa) we would expect a rotational relaxation time of around 0.68 ns, instead of the experimental value of around 45 ns observed for dilute myoglobin solutions by South & Grant [141]. As another example, HEWL (M = 14.7 kDa) would be expected to have a value of 11.4 ns, compared with the experimental value of 0.3-0.4 ps [142].

The fact that the experimental relaxation times tend to exceed the theoretical ones expected from Equations 5.1-5.3 suggests that the molecular weight, and hence effective volume, of the rotating entity is greater than that of the protein molecule alone. A plausible explanation is that a layer or two of water of hydration remains strongly associated with each protein molecule during its orientational relaxations. Thus, by considering that the translational and rotational motions of hydrated water were restricted by proteins through hydrophobic and hydrophilic interaction in the protein solution, we will try to adopt the Debye model combined with the resonant effects to model this complex interaction in Chapter 6.

Figure 5.6 indicates the Cole-Cole plots of the HER2 and HEWL at a concentration of 5mg/ml and 2.5mg/ml respectively. Cole-Cole plots (the imaginary part of the permittivity against the real part) can be used to deduce whether the system is governed by a single relaxation time or a distribution of relaxation times, as a single relaxation time (Debye relaxation) is characterized by a semicircular Cole-Cole plot whereas a distribution of relaxation times would have a skewed arc [142]. The Cole-Cole plots for our data are shown in Figure 5.6 and the data appear to have the shape of an arc, indicating a distribution of relaxation times for this sample should be described by the Debye relaxation. However, the data at the high frequency side shapes the arc to be a skewed arc, in which case the Cole-Cole plot would indicate that the dielectric dispersion arises from a resonant process. We will discuss this analysis further in the Chapter 6.

By comparing the HEWL and HER2 plots, the main difference between them, as suggested by Cole-Cole plots, is the real part ε' at the higher frequency: that is the HER2 extends its range back to approximate 3, but it is not found for HEWL. When comparing the different concentration for each protein, we find that the real and imaginary parts increase with the increase in water fraction. Furthermore, according to the simulation analysis in Chapter 6, we know that both the relaxation time τ_2, which is interpreted in terms of the so-called δ-dispersion, characterized for the interaction in the protein solutions, and the resonant time τ decreases with the decrease in the concentration of the protein solution. For the protein solutions, the changes of relaxation time of the system correlated qualitatively with the proportion of apolar groups to dipolar ions in the solute (τ increasing with increasing apolarity), as well as with the proportion of total water immobilized as a hydration shell. Therefore we can conclude that because of the increasing of the protein concentration, the apolarity of the protein solution increases, and so the translational and rotational motions of hydrated water were more restricted by proteins.

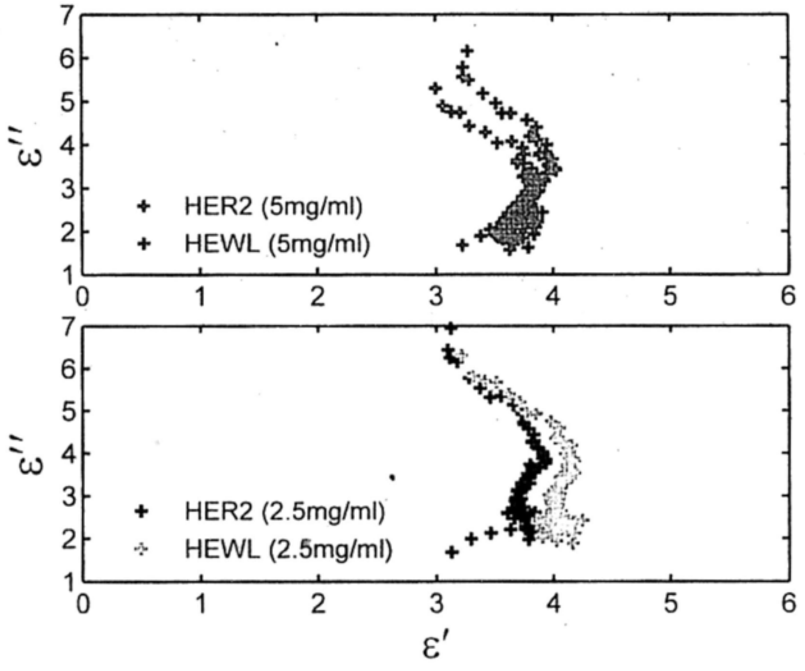

Figure 5.6: Cole-Cole plot for HER2 and HELW solution at different concentration.

5.4 Solid State Studies

5.4.1 Introduction

Rather than measure the dielectric properties of proteins in solution, one can measure protein powders as a function of their water content. The advantages of this approach include the ability to determine dielectric phenomena associated with protein-water interactions in the absence of protein and polar sidegroup orientational relaxations, and to investigate effects that arise from the motions of ions and protons on the hydrated protein surface.

5.4.2 Sample Preparation

In order to minimize surface scattering and scattering in the sample, homogeneous samples are required. This is accomplished by milling the solid samples into a single powder and subsequently pressing this powder into pellets with a mechanical press. This method for sample preparation allows us to produce high quality samples with defined thickness and a high degree of homogeneity, optimally suited for THz spectroscopy.

In order to decrease the concentration of the sample material, which prevents the strong absorption at higher frequencies exceeding the dynamic range of the terahertz measurement, it is useful to prepare mixed pellets with polyethylene (PE) powder at various dilution ratios. PE is nearly transparent and non-dispersive in the THz range with a frequency-independent index of refraction of 1.43 ± 0.02 below 1 THz ($33\ \mathrm{cm}^{-1}$) and is therefore a suitable filling material for far-infrared spectroscopic applications. By taking into account the densities of the sample materials and the index of refraction of PE the absorption coefficient and index of refraction of the pure substance can be extracted. In this study, HER2 and HEWL were pressed into PE in order to be a pellet for further research. Our experiments also confirm the current laboratory results of the THz properties for PE as the absorption properties is almost negligible. The pellet was mounted on the special sample holder with the air as the reference. The measurement was taken under the varied temperature.

5.4.3 Low Absorbing Material – Polyethylene

Polyethylene, the name is abbreviated to PE, is a polycrystalline polymer consisting of long chains of the monomer ethylene. Due to the low absorption properties of the polyethylene material at terahertz frequencies, PE was used as a filling material for sample preparation to exclude saturation of the strong absorption modes and increase the dynamic range and to guarantee mechanical stability and coplanar surfaces to avoid additional scattering effects. Figure 5.7 illustrates the absorption and

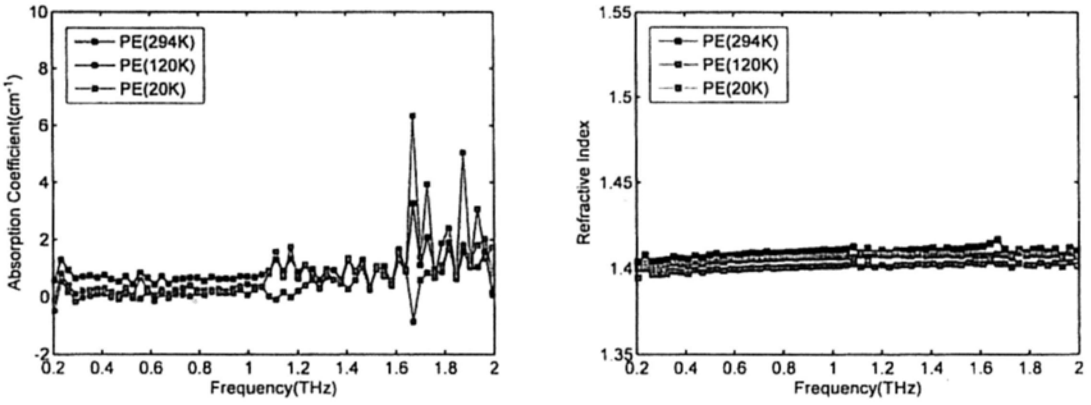

(a) (b)

Figure 5.7: The THz absorption (a) and index of refraction (b) of a high density polyethylene (HDPE) pellet. The three different curves show the spectra of the pellet at 20 K, 120 K and 294 K.

index of a pellet of high density polyethylene (HDPE), recorded with the transmission mode THz time-domain spectroscopy (THz-TDS) system described in Chapter 2. The thickness of the pellet was 3 mm. The absorption spectrum at all temperatures denotes that the absorption is very low, not exceeding 2 cm^{-1} below 1.6 THz. The reason for the negligible absorption can be found in the molecular structure. A molecule like polyethylene is long and so flexible that it can easily become entangled with other molecules to produce a chaotic ensemble. On the other hand, the molecule has such a simple repeat unit and one chain can fit together easily with another (or with itself in the case of a fold) that stereochemical forces strongly favor crystallisation [8]. It is reported that the vibrational mode of polyethylene can clearly be observed centred at 73 cm^{-1} at room temperature. This centre shifts to 78.8 cm^{-1} when the sample is cooled down to 13 K [143]. Based on the temperature dependence of this mode, Krimm and coworkers [144] established that this mode is truly a lattice mode.

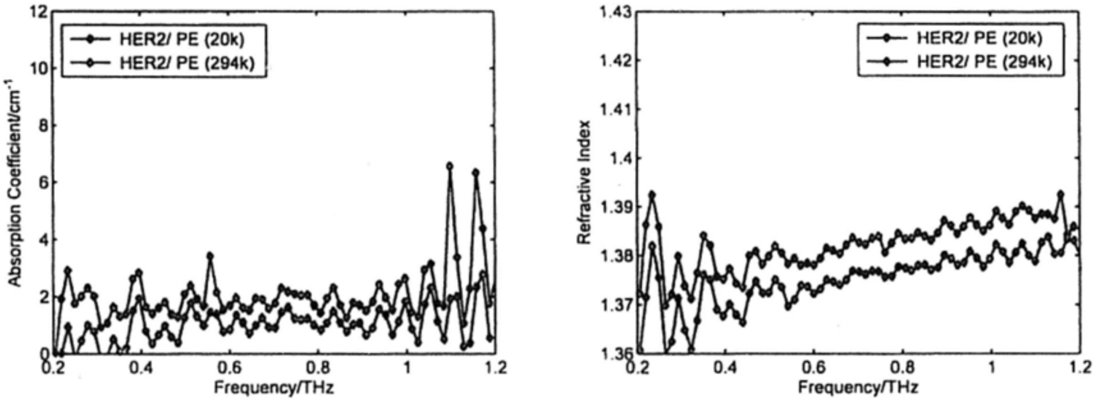

(a) (b)

Figure 5.8: The THz absorption (a) and index of refraction (b) of HER2 pellet at 20 K and 294K.

5.4.4 THz-TDS Results

Figure 5.8 compares the THz absorption and the refractive index of the HER2, recorded at 20 and 294 K. 1 mg HER2 mixed with 100 mg PE was under measurement. In contrast to the spectrum of the HER2, we observe a number of resolved features in the THz region. The intensity of the absorption peaks is distinct when the temperature down to 20 K, however a notable difference is seen in the region from 1.1 to 1.2 THz, as two absorption peaks are only found at 20K.

In Figure 5.9 we show the absorption coefficient and index of refractive index of HEWL at various concentrations. The absorption coefficient is significantly larger with monotonously increasing absorption at high frequencies, as well as a larger increasing absorption at higher protein concentrations. However, the frequency-integrated absorption in the range between 0.2 to 1.6 THz is similar when comparing with spectra at different concentrations, as is the presence of the absorption peaks after 1.6 THz which results in the resonant of the molecule motion; this motion will be compared to the FTIR measurement in the next section. A featureless refractive index profile was observed, and the small difference in overall refractive index was attributed to a change in concentration.

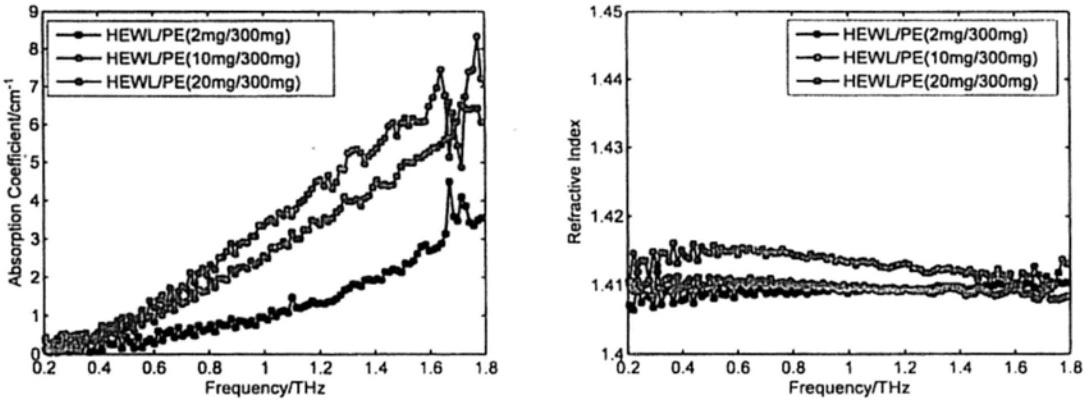

(a)

(b)

Figure 5.9: The THz absorption (a) and index of refraction (b) of HEWL pellet at three concentrations.

5.4.5 Synchrotron Comparison Results

Synchrotron radiation is electromagnetic radiation generated by the acceleration of ultrarelativistic (i.e., moving near the speed of light) charged particles through magnetic fields. This may be achieved artificially in synchrotrons or storage rings, or naturally by fast electrons moving through magnetic fields in space. The radiation produced can range over the entire electromagnetic spectrum, from radio waves to infrared light, visible light, ultraviolet light, X-rays, and gamma rays. It is distinguished by its characteristic polarization and spectrum. The proteins were measured by co-workers at the Australian Synchrotron (Melbourne, Australia). Figure 5.10 [145] presents how a synchrotron works.

For the sample preparation, it was not possible to just press the proteins in PE as the PE we were using for the THz measurements is only transparent for the THz region, above 200 wave numbers it blocks radiation almost completely, thus it is not suitable for the Synchrotron measurements. Therefore, we tried to immobilize the protein on a surface modified carrier that is transparent for the THz region. The protein was diluted in a specific protein binding buffer. Then, to make sure the carrier is homogeneously covered with the protein, the carrier (or rather a small piece of it) is completely submerged in the protein/buffer solution. After a while

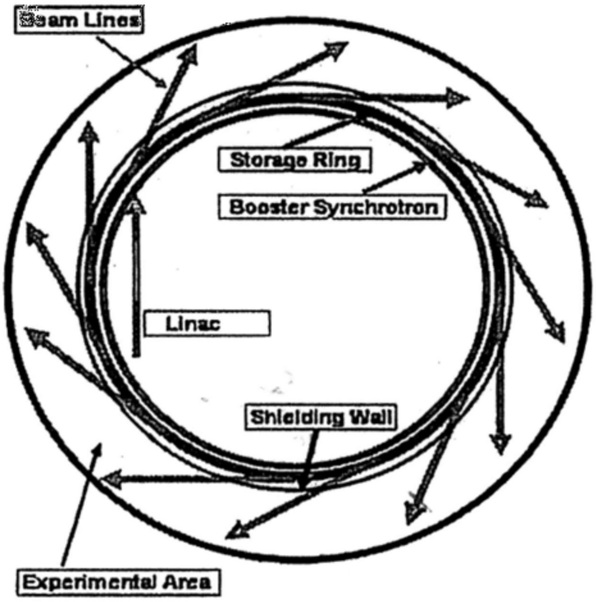

Figure 5.10: Schematic diagram of the Synchrotron.

(around 90 min) it is washed in a wash buffer solution to make sure all the proteins that have not binded to the carrier are washed off. For the reference, we used a carrier that has been in the pure buffer solution (obviously without protein) and has been washed and dried afterwards. The sample was a carrier that has been in the protein/buffer solution, then washed and dried. Before starting this procedure, the pure dry carriers had been measured individually to ensure they did not have different spectra.

In order to compare THz-TDS spectrum, the regions between 6.6 and 39.6 wavenumbers (0.2-1.2 THz) for HER2 and 6.6 and 66 wavenumbers (0.2-2 THz) for HEWL were extracted from the synchrotron spectrum.

The synchrotron spectrum in Figure 5.11 indicates 3 absorption peaks at 9.18, 12.1 and 20.1 wavenumbers (~0.28, 0.38 and 0.61 THz) respectively. Comparing with the measurement using THz-TDS, we observed similar features but with a small frequency shift in the absorption characteristic at 0.24, 0.40 and 0.56 THz. In addition, another two relative higher peaks at 1.09 and 1.15 THz were detected in

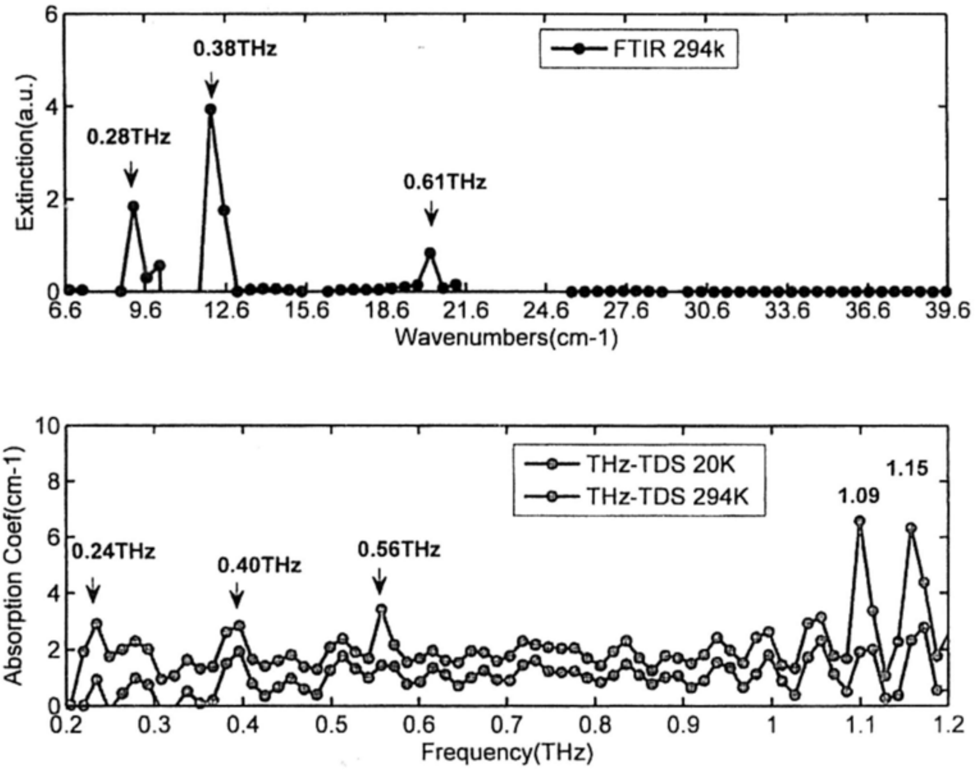

Figure 5.11: HER2 comparison spectrum for (up) synchrotron measurement at 294 K and (down) THz-TDS measurement at 20 and 294 K.

THz-TDS spectrum, however were not shown using synchrotron measurement. The reason for these deviations were possibly due to the technical restraints as the best results with the Synchrotron spectrometer are obtained above 50-80 wavenumbers. All data below can give good information about band locations, but the absolute values might not be exact. On the other hand, the normal reflection losses at a perfectly flat interface between two materials (carrier and protein) of different index of refraction should also be considered as a possible cause of the difference. The comparison spectrum under synchrotron measurement and THz-TDS measurement at different concentrations for HEWL was shown in Figure 5.12, the characteristic absorption is observed in the same range in both the synchrotron and THz-TDS

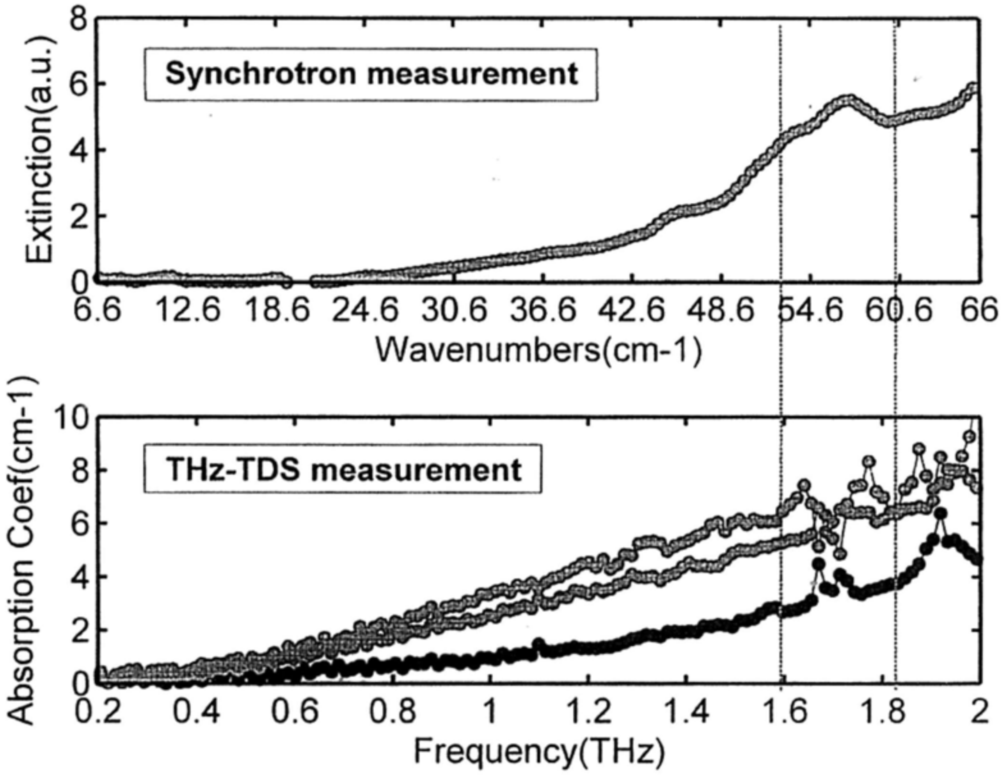

Figure 5.12: HEWL comparison spectrum for (up) synchrotron measurement and (down) THz-TDS measurement.

spectrum.

5.5 Summary

In this chapter, we presented the terahertz absorption and dielectric dispersion properties of a biomarker protein HER2 and HWEL which is a common protein used as an experimental substance determined by THz time-domain transmission spectroscopy. The observation of distinct differences at low as well as at room temperature demonstrate that THz spectroscopy can be used to distinguish the anharmonicity of the vibrational potential which relates to the strength of the reset force of the oscillating system in the HER2 molecule. Important parameters of the dynamics of the molecules' low frequency relaxation motion can be extracted using a simple model. By comparing the absorption spectra of the THz-TDS and Synchrotron it is possible to deduce the approximate localization of the different vibrational modes within the molecular chain. The time-resolution of THz-TDS of less than 250 fs [146], demonstrates the feasibility of a femtosecond time-resolved experiment in this interesting spectral region. A realistic future goal can therefore be the direct observation of biomarker molecular dynamics by studying the low-frequency modes in a time-resolved THz-experiment.

Chapter 6

Modeling for Liquid and Protein Solution

In previous chapters, the terahertz properties of the protein dynamics in the liquid phase have been investigated using both reflection and transmission systems. The measurement reveals that the THz dielectric spectrum is sensitive to the conformational mutation of protein and depends on the surface charge and flexibility of the protein. This chapter is mainly concerned with model fitting based on Debye theory for several liquids. In terms of the relaxation process of water which has been investigated by several groups [29, 104, 147–149], the double Debye model is used for water in this work in the aim of the comparison. Other liquids than water, such as methanol, ethanol, acetone, iso-propanol, glycerol and glycerol/water solutions are also discussed, and are successfully fitted by either a single or a triple Debye model considering their polar moment. The investigation of these liquids indicated is the first step towards the study of more complex protein solutions. In addition to the work outlined above, within this chapter an improved fitting model considering the resonant absorption effect combined with the triple Debye model is proposed and then applied to describe the biomolecule-water interactions first discussed in Chapter 5.

6.1 Dielectric Theories

When a dielectric medium is placed in an electric field, the current that flows in this medium can be separated into two parts: a conduction part, which corresponds to an actual current; and a displacement current part, which can be perceived as the elastic response of the medium to the applied field.

Polar molecules in a dielectric medium are oriented randomly without an applied electric field. When an external field is applied, the material is polarized; electric charges do not flow through the material, as in a conductor, but only slightly shift from their average equilibrium positions causing dielectric polarization: positive charges are displaced along the field and negative charges shift in the opposite direction. This polarization creates an internal electric field which partly compensates the external field inside the dielectric as shown schematically in Figure 6.1 [150].

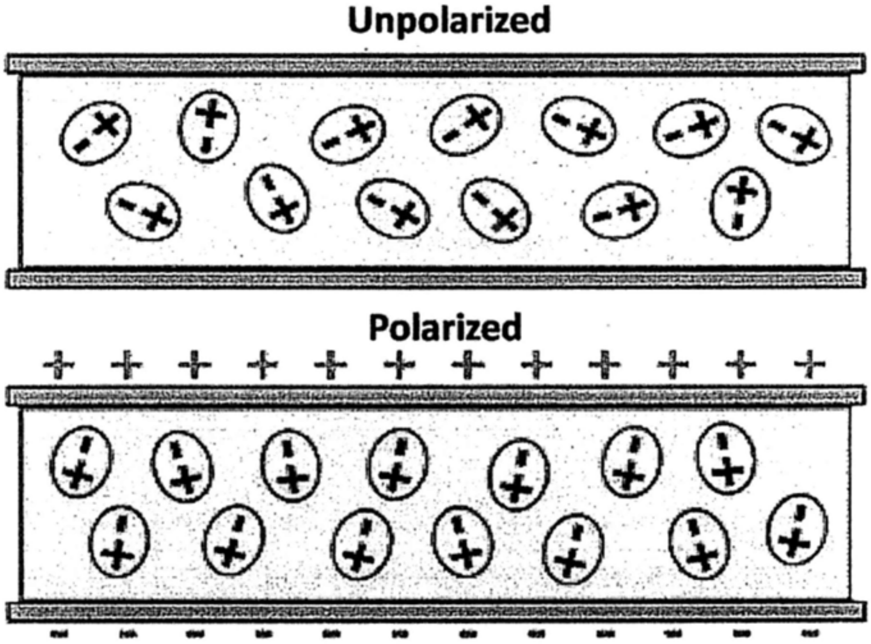

Figure 6.1: Response of a dielectric medium containing polar molecules to an applied electric field between parallel plates.

Here, the effect of an applied electric field E is represented by charge migration and dipole reorientation. Both of these effects on the electrical charge distribution of the medium are accounted for by D, electric displacement field. The permittivity ε is defined as the constant of proportionality relating the electric field to the electric displacement field:

$$D = \varepsilon E \tag{6.1}$$

The electric susceptibility relates the electric field to the dielectric polarization density P of the medium.

$$P = \varepsilon_0 \chi_e E \tag{6.2}$$

Here, ε_0 is the permittivity of free space (vacuum) and χ_e is electric susceptibility. It should also be noted that the polarization density is directly related to the dipole moment M as

$$P = \frac{M}{V} = \frac{1}{V} \sum_{i=1}^{N} q_i r_i \tag{6.3}$$

Here, V is the volume. The permittivity of a medium relative to the permittivity of free space is called the relative permittivity, or dielectric constant, and is denoted by ε_r

$$\varepsilon = \varepsilon_r \varepsilon_0 \tag{6.4}$$

The susceptibility is related to the relative permittivity by

$$\chi_e = \varepsilon_r - 1 \tag{6.5}$$

From this equation it follows that the electric susceptibility of a vacuum is zero. The dielectric displacement D is related to the polarization density P as:

$$D = \varepsilon_0 E + P = \varepsilon_0 (1 + \chi_e) E = \varepsilon E \tag{6.6}$$

Unlike vacuum, the polarization of a dielectric medium depends on the frequency of the applied field, since the material cannot polarize instantaneously.

$$P(\omega) = \varepsilon_0 \chi_e(\omega) E(\omega) \tag{6.7}$$

with ω being the frequency of the electric field. This frequency dependence of the response is due to causality, which also makes permittivity a frequency dependent complex function.

$$D_0 e^{i\omega t} = \varepsilon(\omega) E_0 e^{i\omega t} \tag{6.8}$$

where D_0 and E_0 are the amplitudes of dielectric displacement and applied electric field. The real and imaginary parts of the complex permittivity can be written as

$$\begin{aligned}
\tilde{\varepsilon}(\omega) &= (\tilde{n})^2 = (n - i(\frac{c\alpha}{2\omega}))^2 \\
&= n^2 - (\frac{c\alpha}{2\omega})^2 - 2n(\frac{c\alpha}{2\omega})i \\
&= \varepsilon'(\omega) - i\varepsilon''(\omega) \qquad (6.9) \\
&\Rightarrow \varepsilon'(\omega) = n^2 - (\frac{c\alpha}{2\omega})^2 \\
&\Rightarrow \varepsilon''(\omega) = 2n(\frac{c\alpha}{2\omega})
\end{aligned}$$

The complex permittivity $\tilde{\varepsilon}(\omega)$ is expressed by the real part ε' and the imaginary part ε'' in which the real part corresponds to the dielectric constant and the imaginary part, known as the dielectric loss factor, is a measure of the energy absorption per cycle [38]. The real and imaginary parts of the complex permittivity were calculated from the frequency-dependent optical constants $n(\omega)$ and $\alpha(\omega)$ as shown in Equation 6.9.

6.2 The Debye Model

The linear dielectric response for a time-dependent electric $E(t)$ is described by

$$D(t) = \varepsilon_\infty E(t) + \int_{-\infty}^{t} \phi(t - t')E(t')dt' \tag{6.10}$$

where ε_∞ stands for the immediate response and the response function $\phi(t)$ accounts for the time-dependent response. For an input electric field of delta function

$$E(t) = \delta t \tag{6.11}$$

Equation 6.10 gives

$$D(t) = \varepsilon_\infty E(t) + \phi(t) \tag{6.12}$$

which means that the function $\phi(t)$ describes the response for an impulse electric filed. The Fourier transform of Equation 6.10 prescribes the dielectric function

$$\varepsilon(\omega) = \varepsilon_\infty + \int_0^\infty dt e^{i\omega t} \phi(t) \tag{6.13}$$

as a function of frequency ω. Equation 6.13 is also called the complex dielectric function. Now, the Debye model assumes the response function to be

$$\phi(t) = \begin{cases} 0 & for \quad t < 0, \\ \frac{\varepsilon_s - \varepsilon_\infty}{\tau} e^{-t/\tau} & for \quad t > 0. \end{cases} \tag{6.14}$$

Here, ε_s stands for the static dielectric function $\varepsilon(0)$, and τ is called relaxation time. Thus the above response function abruptly rises at $t = 0$ and then decays exponentially. The Fourier transform of Equation 6.14 gives the familiar dispersion relation

$$\varepsilon(\omega) = \varepsilon_\infty + \frac{\varepsilon_s - \varepsilon_\infty}{1 + i\omega\tau} \tag{6.15}$$

This model was originally put forth by Debye for rotatable dipoles (molecules) in viscous liquid solutions and was subsequently extended to other various relaxation processes, and it is easy to separate the real and imaginary components:

$$\varepsilon'(\omega) = \varepsilon_\infty + \frac{\varepsilon_s - \varepsilon_\infty}{1 + \omega^2\tau^2} \tag{6.16}$$

and

$$\varepsilon''(\omega) = \frac{(\varepsilon_s - \varepsilon_\infty)\omega\tau}{1 + \omega^2\tau^2} \tag{6.17}$$

One of the strengths of using fs THz pulses is that they measure both the absorption and dispersion of the sample, allowing $\varepsilon(\omega)$ to be determined. The frequency-dependent, complex dielectric function, $\varepsilon(\omega) = \varepsilon'(\omega) - i\varepsilon''(\omega)$, provides a fundamental description of a medium. In the diffusional regime, the frequency dependence of $\varepsilon(\omega)$ is often successfully used to fit the analytic expressions based on the bulk reorientational relaxation times, τ [104].

6.3 Multi-pole Model

In general there are multiple mechanisms at various scales that account for polarization. To attempt to account for several of these over a range of frequencies, researchers tend to use the ubiquitous empirical Havriliak-Negami equation model to describe multi-pole conditions given by Equation 6.18:

$$\varepsilon(\omega) = \varepsilon_\infty + \sum_{j=1}^{n} \frac{\varepsilon_j - \varepsilon_{j+1}}{[1 + (i\omega\tau_j)^{1-\alpha_j}]^{\beta_j}} \tag{6.18}$$

Here, ω is the angular frequency, n is the number of relaxation processes, τ_j are their relaxation time constants, $\varepsilon_1 = \varepsilon_s$ is the static dielectric constant, ε_j are intermediate steps in the dielectric constant, $\varepsilon_{n+1} = \varepsilon_\infty$ is its limiting value at high frequency. The parameters $\alpha_j > 0$ and $\beta_j < 1$ describe either a symmetric or asymmetric distribution of relaxation time for process j.

The Debye equation treatment with $n = 1$, $\alpha = 0$, and $\beta = 1$ is the simplest case. It requires that a single relaxation time can provide an adequate description; in some sense, this indicates that all molecules sample the same environment over the time τ (see Equation 6.15).

More complicated models yield correspondingly more complicated expressions. Multiple Debye relaxation times are incorporated using Equation 6.18 with $n > 1$, $\alpha = 0$, and $\beta = 1$ and are as follows

$$\varepsilon(\omega) = \varepsilon_\infty + \sum_{j=1}^{n} \frac{\varepsilon_j - \varepsilon_{j+1}}{1 + (i\omega\tau_j)} \tag{6.19}$$

Some polar liquids exhibit a continuous distribution of relaxation times, which necessitates a Cole-Cole or Cole-Davidson description. A Cole-Cole treatment, with $0 < \alpha < 1$, describes a symmetric distribution, while a Cole-Davidson treatment, with $0 < \beta < 1$, describes a skewed distribution. Both Cole-Cole and Cole-Davidson treatments can be applied to cases that have either a single distribution of times or multiple distributions ($n = 1$ or $n > 1$, respectively).

6.4 Van Vleck-Weisskopf- Frölich Type Resonant Absorption

Debye-type relaxation functions are monotonically decaying because only such mechanisms act within the system, so making the system approach a thermal equilibrium state corresponding to an instantaneous value of the external force. In nature there are many cases where other mechanisms are built into the system, making it oscillate harmonically with certain characteristic frequencies. In such cases the relaxation function is of the damped oscillation type, and phenomena relating to resonance absorption of external energy are observed.

The resonance absorption of the Van Vleck-Weisskopf- Fröhlich type is described by an exponential type of relaxation function multiplied by the cosine function with a characteristic frequency ω_0

$$\psi(t) = (\varepsilon_s - \varepsilon_\infty)e^{-t/\tau}\cos\omega_0 t \quad (t > 0) \tag{6.20}$$

$$\phi(t) = \frac{\varepsilon_s - \varepsilon_\infty}{\tau}e^{-t/\tau}[\cos\omega_0 t + \omega_0\tau\sin\omega_0 t] \quad (t > 0) \tag{6.21}$$

From Equation 6.22,

$$\Phi_{\mu\nu}(t) = -\frac{d\Psi_{\mu\nu}}{dt} \tag{6.22}$$

and the complex dielectric function is given by Equation 6.23.

$$\varepsilon(\omega) = \varepsilon_\infty + \frac{\Delta\varepsilon}{2}\left(\frac{1 - i\omega\tau}{1 - i(\omega + \omega_0)\tau} + \frac{1 + i\omega\tau}{1 - i(\omega - \omega_0)\tau}\right) \tag{6.23}$$

$$\Delta\varepsilon = \varepsilon_s - \varepsilon_\infty$$

The reason why we write $\Delta\varepsilon$ in place of is to indicate that the real part of the complex dielectric function $\varepsilon'(\omega)$ decreases by $\Delta\varepsilon$, as that of the Debye type does by $\varepsilon_s - \varepsilon_\infty$, when the angular frequency increases from zero to infinity. Here ε_∞ denotes the value $\varepsilon'(\omega)$ of at ω sufficiently far from the resonance point. Therefore, the value of $\varepsilon'(\omega)$ on the low-frequency side becomes $\varepsilon_\infty + \Delta\varepsilon$. Separating the function 6.23 into its real and imaginary parts gives

$$\varepsilon'(\omega) - \varepsilon_\infty = \frac{\Delta\varepsilon}{2}\left(\frac{1 + \omega_0(\omega + \omega_0)\tau^2}{1 + (\omega + \omega_0)^2\tau^2} + \frac{1 - \omega_0(\omega - \omega_0)\tau^2}{1 + (\omega - \omega_0)^2\tau^2}\right) \tag{6.24}$$

$$\varepsilon''(\omega) = \frac{\Delta\varepsilon}{2}\left(\frac{\omega\tau}{1 + (\omega + \omega_0)^2\tau^2} + \frac{\omega\tau}{1 + (\omega - \omega_0)^2\tau^2}\right) \tag{6.25}$$

The imaginary part $\varepsilon''(\omega)$ related to the energy absorption has its maximum value $\sqrt{1 + (\omega_0\tau)^2}(\Delta\varepsilon/2)$ at the frequency $\omega = \sqrt{1 + (\omega_0\tau)^2}/\tau$ which is larger than ω_0 and $1/\tau$.

6.5 Liquid Water

6.5.1 Introduction

Water is a typical polar molecule and because of its role in biomolecule dynamics has attracted much interest over the past decade. Many types of water molecule vibrations existed in various different phases. In the case of the liquid states, the librations are considered as a kind of restricted relaxations since hydrogen bonds are formed due to the weak inter-molecular interactions. Relaxation is a reactive process that may involve translational and rotational diffusion, hydrogen bond rearrangement and structural rearrangement depending on the time scale in such processes. As a result, this process can be modeled as oscillators using Debye theory, as described in an earlier investigation [151]. Its importance is related to the fact that it is a macroscopic property that brings information on the microscopic nature of the water.

Recently, there has been significant progress in the study of spectra of liquid water in the far-infrared (FIR) region of the spectrum which bridges the region between bulk dielectric relaxation and intermolecular motions. The frequency dielectric response of liquid water has been extensively studied [152, 153]. Van Exter *et al.* [154] firstly published the spectrum of water in the THz regime [155], where the 9 strongest water vapour lines from 0.2-1.45 THz were measured in their work. Thrane *et al.* (1995) reported THz optical properties of liquid water measured at 292 K. Kindt and Schmuttenmaer [29] investigated the frequency-dependent THz optical properties of water and more recently a study was published by Ronne *et* *al.* [104] investigating the T-ray spectra of liquid water as a function of temperature. According to the further research, two reorientational relaxation processes have been suggested to occur in liquid water [156]. Describing it briefly, water molecules form a tetrahedral structure, and so in order to reorient, four hydrogen bonds need to be broken which is a slow process τ_1. Subsequently after approximately 1, the single water molecule will reorient and move to a new tetrahedral site in a fast process τ_2 [104]; consequently a double Debye relaxation model can be adopted to reproduce this process well. Additionally, temperature dependent effects for the water were investigated by Kristensen *et al.* They developed a generalized model for estimating the heating effect which easily can be applied to other liquids and solids by changing the material constants [157].

6.5.2 Water Fitting

Apart from its extended use in chemistry as solvent, water plays a significant role in biological processes. Here, we describe the dielectric function measured for water and compare our results with the data already published, which is step towards obtaining valuable information about the dynamics of another polar liquids and protein solutions in the next section.

In previous dielectric relaxation studies described in Section 6.1.1, a single Debye relaxation can be found to be a good agreement between experimental data and the model of the polarization for frequencies up to 100 GHz ($\varepsilon = 78.36$, $\tau = 8.27$ ps, $\varepsilon_\infty = 5.16$) [158]. However, when the single Debye model is adopted into the far-infrared or to higher frequencies (into the THz range), it fails to reproduce the experimental findings [159]. In the later paper [159] it was suggested that an additional second relaxation process ($\tau_2 = 1.02$ ps) is needed at THz frequencies in order to adequately fit the data; namely that the double Debye model of polarization response of the water was able to account for the observed experimental data [38, 147, 159]. This process was described by Equation 6.26, τ_D (slow) and

τ_2 (fast) are two relaxation times, ε_s is the static dielectric constant, ε_1 and ε_∞ are parameters that indicate the size of the coupling between the relaxation mode and the electric field. The differences $\varepsilon_s - \varepsilon_1$ and $\varepsilon_1 - \varepsilon_\infty$ are accordingly relative measures of the contribution to the macroscopic polarization from the two relaxation processes [104].

$$\varepsilon(\omega) = \varepsilon_\infty + \frac{\varepsilon_s - \varepsilon_2}{1 + i\omega\tau_D} + \frac{\varepsilon_2 - \varepsilon_\infty}{1 + i\omega\tau_2} \tag{6.26}$$

Figure 6.2 presents the frequency-dependent absorption coefficient and refractive index as well as a Cole-Cole plot (an Argand diagram of $\varepsilon'(\omega)$ vs $-\varepsilon''(\omega)$ for water at room temperature using a transmission setup shown as Figure 5.3. The real and imaginary parts of the dielectric function are defined as $\varepsilon'(\omega) - i\varepsilon''(\omega) = (n(\omega) - i\kappa(\omega))^2$ (details described in Section 6.2.) The red curves in Figure 6.2(a) & (b) are the data measured by TeraView using a reflective system for comparison. The fitted curve (black solid line in Figure 6.2(c)) compared the experimental data to the double Debye relaxation model. In Table 6.1 we compare the fitting parameters obtained using our data and data from the literature [29, 104, 147–149].

	This work	Ronne [104]	Kindt [29]	Barthel [149]	Peter [148]	Pickwell [147]
ε_s	79.2	80.58	78.36	78.36	78.36	78.8
ε_2	5.3	5.2±0.1	4.93±0.54	6.18	5.16±0.06	6.6
ε_∞	3.3	3.3±0.3	3.48±0.70	4.49	3.49±0.07	4.1
τ_D(ps)	8.6	8.5±0.4	8.24±0.40	8.32	7.89±0.06	10.6
τ_2(ps)	0.17	0.170±0.04	0.180±0.014	1.02	0.181±0.014	0.18

Table 6.1: Comparing parameters from this work with previously published for water

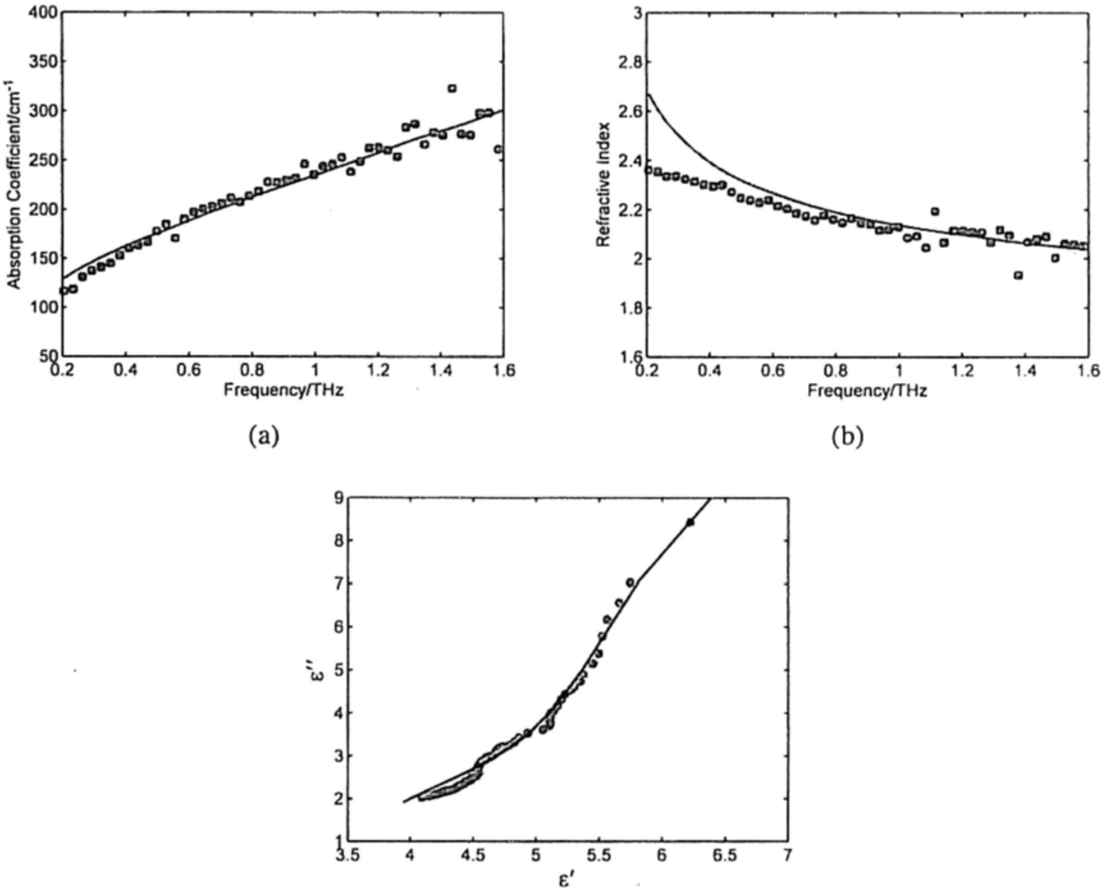

(a)

(b)

(c)

Figure 6.2: THz spectrum of (a) Absorption coefficient; (b) Refractive index; (c) Cole-Cole plot for water from 0.2 to 1.6 THz presented by blue dot (transmission system). The red curve in (a) & (b) is the measured data by TeraView for comparison (reflection system). Black solid curve in (c) compared the experimental data to the double Debye relaxation model. The corresponding parameters for this fit are shown in Table 6.1.

6.6 Polar and Non-polar Liquids

6.6.1 Introduction

All types of liquids can be classified in to polar and non-polar due to whether or not molecular are able to possess a permanent electric dipole moment and can also be distinguished by whether or not molecules are able to form hydrogen bonds (protic or aprotic solvent). As for a polar liquid, the significant stabilizing force in macromolecules is supported by the hydrogen bond [19], since the bond energy usually ranges from 1 kcal/mol to 5 kcal/mol [160] which is smaller than the covalent bond energy, but greater than the thermal energy (0.6 kcal/mol) at room temperature. Certainly, the strength of hydrogen bonds depends on the donor and acceptor as well as their environment.

According to a simple model proposed by Debye [161, 162], a macroscopic polarization is created to explain a microscopic alignment of the molecular dipole moments when an external electric field is applied to a polar liquid. Kindt and Schmuttenmaer [29] reported the multiple-Debye behavior of polar liquids such as methanol, ethanol, 1-propanol and liquid ammonia. Asaki *et al.* (2002) studied the solvation dynamics of lithium salts in water, methanol, and propylene carbonate and verified the results using the Debye relaxation models. In an investigation conducted by Jepsen *et al.* [148], the alcohol content of an aqueous solution has been characterised. In the THz regime [29, 163] alcohol, which consists of an OH group attached to a hydrocarbon chain, may be fitted by Debye theory with three relaxation processes.

On the other hand, Pedersen and Keiding [164] reported the absorption of non-polar liquids is due to transient dipole moments (temporary dipole moments) induced via collisions in the liquid. For this reason, non-polar liquids have absorption coefficients 100 times smaller than polar liquids [164]. In another study conducted by Yu *et al.* [165], the dielectric relaxation properties of non-polar solvent have been investigated and fitted with a single Debye relaxation model.

6.6.2 Polar and Non-polar Liquids Fitting

The fundamental questions about how to understand the reorientational dynamics of liquid state system can be probed by dielectric relaxation experiments [166]. The relaxation time τ and the dielectric dispersion amplitudes $\Delta\varepsilon$ of the underlying relaxation processes can be extracted based on this theoretical treatment, which provide a wealth of information on equilibrium systems of pure liquids [167].

The modeling of the dielectric relaxation question is still a matter of discussion [149]. Earlier time-resolved solvation studies [168, 169] clearly evidence the inadequate data of the liquid dielectric relaxation by a simple exponential with time constant . There are a number of permittivity data available in the microwave range up to 50 GHz, and similarly (although to a lesser extent) into the far-infrared for simple liquids. According to the pioneering work of Garg and Smyth [170], three distinct dispersion processes existed to satisfactorily account for the dielectric properties of 1-propanol and its higher homologues. A similar behavior expected for methanol and ethanol, and indeed, it was evidenced later, but data were still scarce at THz frequencies. The objective of this section is to shift the maximum frequency accessible by our system to 1.2 THz to the dielectric relaxations in polar liquids (ethanol, methanol, iso-propanol, acetone, glycerol and glycerol/water mixture) and subsequently to report the best reproduction of the complex permittivity spectrum of these polar liquids in order to develop a concept of the microscopic nature of dipole orientations in the terahertz frequency range.

The liquid samples (ethanol, methanol, iso-propanol and acetone) were supported by the Adelaide THz laboratory and were purchased from Sigma-Aldrich (USA). The dielectric spectra presented were determined at 25°C in the frequency 0.2-1.2 THz using a THz time-domain transmission system; the schematic diagram of which was shown in Figure 4.6. The glycerol was also purchased from Sigma-Aldrich (USA). The details about the sample preparation and measurement can be found in Chapter 4 and Chapter 5.

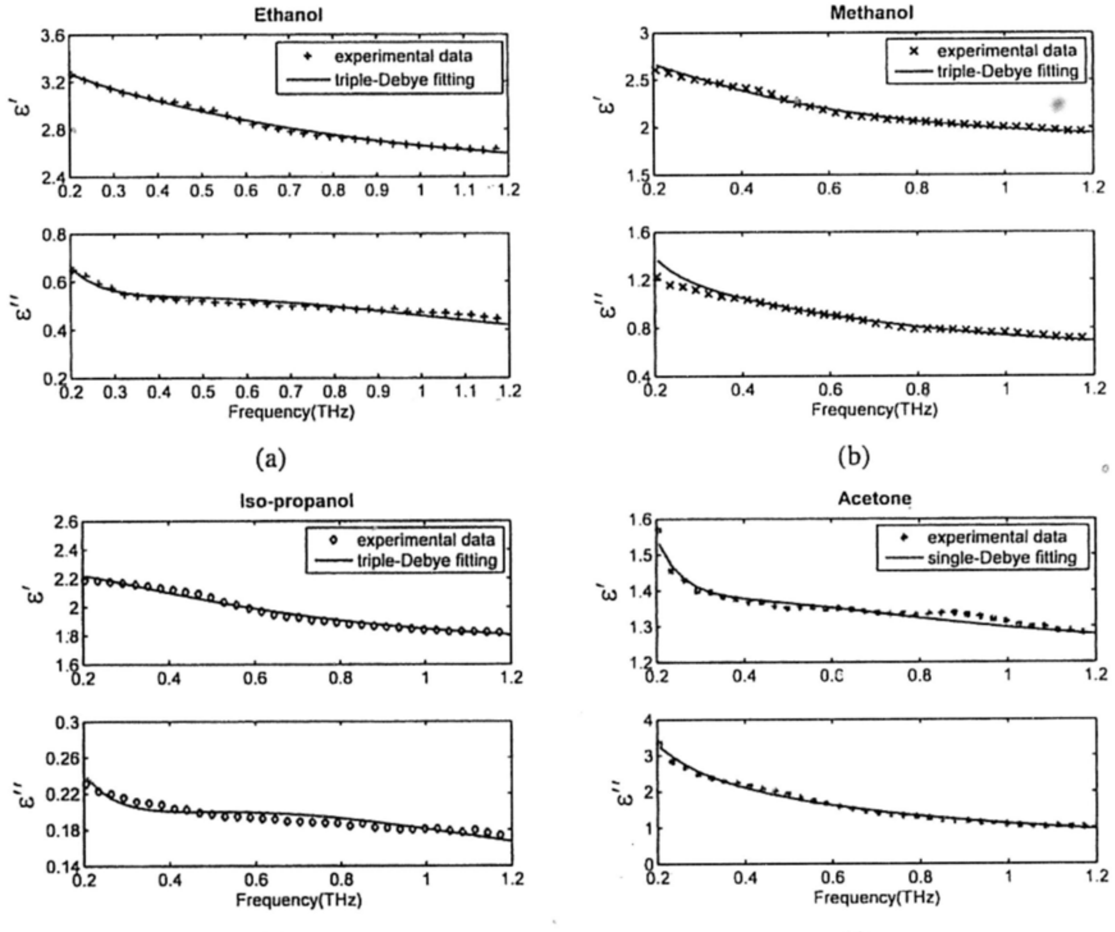

(a) (b)

(c) (d)

Figure 6.3: Dielectric dispersion $\varepsilon'(\omega)$ and loss spectrum $\varepsilon''(\omega)$ of polar liquids (a) Ethanol; (b) Methanol; (c) Iso-propanol and non-polar liquid (d) Acetone at room temperature.

Figure 6.3 shows the frequency-dependent dielectric parameters of both polar liquids (ethanol, methanol, iso-propanol) and a non-polar liquid (acetone) fitting by triple Debye (Equation 6.27) and single Debye model (Equation 6.27) respectively. The solid lines are calculated with the Debye relaxation model using the parameters of Table 6.2. For data fitting a non-linear least squares routine is applied. The static dielectric constant of liquids, ε_s, was determined by conventional low frequency measurements. We kept the same value of the static dielectric constant for ethanol and methanol as that defined by Barthel *et al.* [149].

$$\varepsilon(\omega) = \varepsilon_\infty + \frac{\varepsilon_s - \varepsilon_2}{1 + i\omega\tau_1} + \frac{\varepsilon_2 - \varepsilon_3}{1 + i\omega\tau_2} + \frac{\varepsilon_3 - \varepsilon_\infty}{1 + i\omega\tau_3} \qquad (6.27)$$

All polar liquids in Table 6.2 show a dielectric behavior characterized by three separate relaxation steps. The fastest relaxation rate τ_3 is connected to the dynamic hydrogen bonding, since it is close to the fast relaxation time of hydrogen bonding in water ($\tau_2 = 0.17$ ps) determined previously. The amplitude $\Delta\varepsilon_3(\Delta\varepsilon_3 = \varepsilon_3 - \varepsilon_\infty)$ which markedly exceeds $\Delta\varepsilon_2(\Delta\varepsilon_2 = \varepsilon_2 - \varepsilon_3)$ does not support the relaxation mechanism but only the OH group rotation suggested in the hydrogen-bonded liquids by Garg and Smyth [170]. The intermediate dispersion $\Delta\varepsilon_2$ is dominated by the interaction of the liquid molecules. The step τ_1 and $\Delta\varepsilon_1(\Delta\varepsilon_1 = \varepsilon_s - \varepsilon_2)$ is related to the single molecule reorientation evidenced by J. Barthel [149].

In contrast to the other hydrogen-bonded liquids, acetone is a non-hydrogen-bonded liquid (aprotic liquid). Namely there are no polar hydroxyl groups in the molecule. We found that, with some exceptions, the dielectric dispersion $\varepsilon'(\omega)$ value, which is related to the static dielectric constant ε_s of hydrogen-bonded liquids (ethanol, methanol, iso-propanol and glycerol) is generally larger than a non-hydrogen-bonded liquid (acetone), mainly due to the regular alignment of the dipolar molecule in the hydrogen-bonded cluster. Another typical phenomenon associate with the dielectric properties is that the dominant relaxation time τ_1 for hydrogen-bonded liquids is larger than that observed for acetone.

Glycerol has been used as a solvent in the protein studies of Chapter 5, since

	ε_s	ε_∞	ε_2	ε_3	ε_1(ps)	ε_2(ps)	ε_3(ps)
Ethanol	24.35	2.37	3.8	3.09	163	1.17	0.19
	(24.35)	(1.93)	(4.15)	(2.72)	(161)	(3.3)	(0.22)
	[24.32]	[2.69]	[4.49]	[3.82]	[163]	[8.79]	[1.81]
	24.35^*	1.949^*	4.49^*	2.91^*	163^*	3.21^*	0.235^*
Methanol	32.63	1.51	5.64	4.62	51	3.12	0.18
	(32.63)	(2.1)	(5.35)	(3.37)	(48)	(1.25)	(0.16)
	[32.50]	[2.79]	[5.91]	[4.90]	[51.5]	[7.09]	[1.12]
	$33.64^\dagger$	$5.7^\dagger$			$53^\dagger$		
Iso-propanol	18.3	1.67	2.28	2.11	68.4	0.34	0.23
	$29^\dagger$	$3.2^\dagger$			$292^\dagger$		
Acetone	22.52	1.14			3.98		
	$21.2^\dagger$	$1.9^\dagger$			$3.34^\dagger$		

Values in parentheses are reported by Kindt *et al.* [29] at the frequency about from 2 to 35 cm^{-1}. Values in square brackets are the parameters reported by Barthel *et al.* [149] based on data extending to 293 GHz for methanol, and 89 GHz for ethanol. Values marked with * symbol are reported by Jepsen *et al.* [148] for ethanol from 0.15 to 1.0 THz. Values marked with † symbol are reported by Buckley *et al.* [171] with Debye model applied at 20°C.

Table 6.2: Comparing dielectric parameters from this work with previously published for ethanol, methanol, iso-propanol and acetone

it was able to stabilize the activity of the native structure of proteins. Glycerol is a low-molecular weight hydrogen-bonded liquid, whose molecule contains three polar hydroxyl groups (-OH). As outlined above, one of the most commonly used models to describe dielectric relaxation of aqueous solutions is the triple-Debye model. However, the dielectric relaxation of pure glycerol does not simply fit into the universal trend. As one of the features of the glycerol is to stabilize the structure of protein in frozen situation, therefore for the earlier investigation of pure glycerol at a supercooled liquid state [172], the ubiquitous empirical Havriliak-Negami equation [173,174] model was adopted, which is shown in Equation 6.28

$$\varepsilon(\omega) = \varepsilon_\infty + \frac{\Delta\varepsilon}{(1 + (i\omega\tau)^\alpha)^\beta}, \quad \Delta\varepsilon = \varepsilon_s - \varepsilon_\infty \qquad (6.28).$$

Parameter $\Delta\varepsilon$ describes the relaxation strength, which is proportional to the dipole moment of the electric dipole and to the dipole concentration; the relaxation time τ shows the time scale of the relaxation (position of the relaxation peak on the frequency axis); parameter α is a measure for the width of the relaxation and lower α means that dipoles are more strongly bonded between each other; β describes the symmetry of the relaxation peak which is related to steric hindrances opposing the dipole motions [175].

At room temperature, the relaxation mechanism of pure glycerol has been found to follow a Davidson-Cole-type process at microwave frequencies (1 MHz - 40 GHz). This model treatment with $\alpha = 1$ is the simplest case that reveals an unsymmetric relaxation time distribution. However, the Davidson-Cole model was also reported to fit glycerol data well in reference [176]. Here we attempt to use this model to fit the dielectric response in the terahertz range (0.2-1.2 THz) that has been reported in this work. Furthermore, a glycerol/water (1:1, vol/vol) mixture is also investigated. Because the more water was added in comparing the pure glycerol which resulting in the higher polarization in the glycerol solution, we considered the double Debye model should be described this process exactly.

Figure 6.4 shows the frequency dependence of the relaxation spectrum (dielectric dispersion $\varepsilon'(\omega)$ and loss $\varepsilon''(\omega)$) of both pure glycerol and glycerol/water mixtures at room temperature. Table 6.3 gives the comparison of the model in this work and the published model parameters for glycerol under different temperatures. Fitting parameters for the glycerol/water solution are given in Table 6.5.

	This work	Davidson *et al.* [175]	Holcman *et al.* [172]
model	Davidson-Cole	Davidson-Cole	HavriliakCNegami
t(°c)	25	-60	203
ε_s	42.1*	67.4	$\Delta\varepsilon$=8.94
ε_∞	1.74	4.16	
τ(s)	1.98×10-7		7.89×10-5
α			0.49
β	0.25	0.593	2.02

Table 6.3: Comparison fitting parameters for glycerol including published model

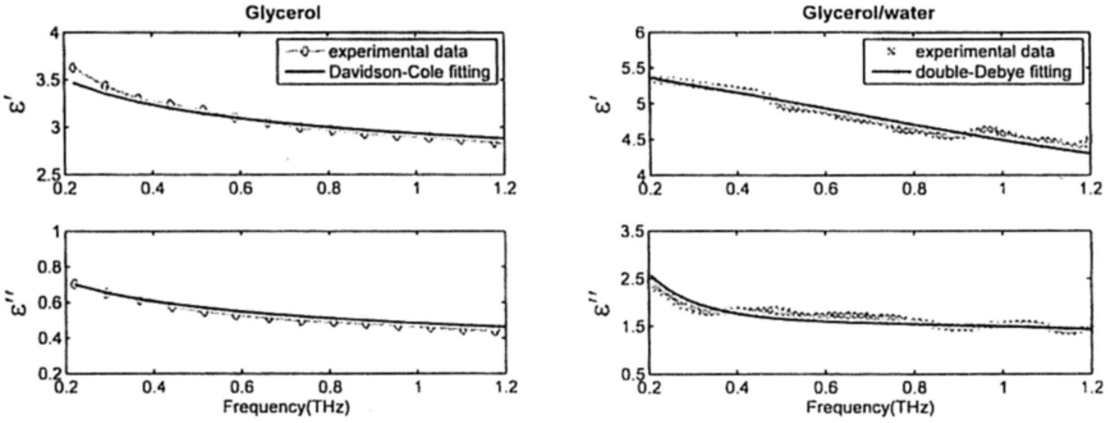

(a) (b)

Figure 6.4: (a) Dielectric dispersion and loss spectrum of glycerol fitted by a Davidson-Cole relaxation model. (b) Dielectric dispersion and loss spectrum of glycerol/water solution fitted by a double Debye relaxation model.

6.7 Biomolecules in Aqueous Phase

6.7.1 Introduction

Lately, there has been a considerable interest in both the experimental and theoretical investigations of biomolecules in aqueous solutions. Jing Xu *et al.* [109] measured the collective dynamics of lysozyme in water. In their work, the low-frequency vibrational modes of proteins in biologically relevant water environments, rather than previously explored dry or slightly hydrated phase, have been demonstrated. They have shown that a broadband terahertz spectrometer can be suitable for the investigation of strongly attenuating protein solutions. Furthermore, Globus *et al.* [177] measured T-ray spectra of DNA in the liquid phase (gel). In their study, they have demonstrated reproducible spectra that show multiple resonances. These resonances are produced by the low frequency vibrational modes within the biological macromolecules in solutions. Moreover, Zhang and Durbin [178] conducted a study on myoglobin (Mb)-water mixtures at various concentrations.

6.7.2 Protein in Solutions

Even though the prior investigations of protein dynamics were always focused on the folding of the protein framework and the movements of the side chains, experimental evidence clearly shows that the vibrations of proteins change as a result of the response of the solvent networks in the vicinity of the protein [151]. With the development of high-performance laser sources, the interaction between protein and its solvent networks can be studied in the terahertz range. Based on the analysis in above section, we have known that the dielectric properties of a solution can be determined as the sum of contributions from individual components (single or multi-Debye relaxation model). Here, we assume that the precise dielectric relaxation data covering the complete time scale of protein molecular reorientations dynamics in the solution system are needed to further develop the present theories on solvent dynamic reactions model.

In the THz range, the interaction between an oscillating electric field and the protein solution system is caused by both relaxation effects and resonant absorption effects [40]. The former is due to transitions of charges or dipoles between equilibrium positions which can be described by a relaxation time τ. The resonant absorption effect is due to displacement of charges bound elastically to an equilibrium position which depends on the nature of dielectrics [179]. According to our assumption, this process can be described by two parts, one is the dielectric relaxation based on the solvent model and the other is the resonant absorption process. The total polarization is then given by

$$\varepsilon = \varepsilon_{\text{resonant}} + \varepsilon_{\text{relaxation}} \quad (6.29).$$

According to Debye theory, the polarization of the background $\varepsilon_{\text{relaxation}}$ resulting from permanent dipole moments of molecules decays exponentially, which can be further expressed by Equation 6.18. A general feature of $\varepsilon_{\text{resonant}}$ has been shown by Equation 6.23. Considering the several different relaxation process and different resonance frequencies, the formula of complex permittivity is given as below:

$$\begin{aligned}\varepsilon(\omega) =& \varepsilon_\infty + \sum_{j=1}^{n} \frac{\varepsilon_j - \varepsilon_{j+1}}{[1 + (i\omega\tau_j)^{1-\alpha_j}]^{\beta_j}} + \varepsilon_\infty \\ &+ \frac{1}{2} \sum_{k=1}^{m} \Delta\varepsilon_k \left[\frac{1 + i\omega_{0k}\tau_k}{1 + i(\omega - \omega_{0k})\tau_k} + \frac{1 - i\omega_{0k}\tau_k}{1 + i(\omega + \omega_{0k})\tau_k} \right]\end{aligned} \qquad (6.30).$$

In Chapter 4, HER2 and HELW dissolved in distill water at different concentration were investigated using THz-TDS transmission system. For data fitting, we determined the first part of Equation 6.30 as a double Debye model because it has been shown previously that the dielectric relaxation of water was able to be fitted adequately using a double Debye model. For the second part, we just consider a single resonance absorption frequency in the simple case which denotes the resonant absorption frequency of oscillation in the system, $\omega_0/2\pi$, due to displacement of bound charges from their equilibrium positions, which further indicates the power loss in the system will be expected to have a maximum near this frequency [180]. The formula is re-written as:

$$\begin{aligned}\varepsilon(\omega) =& 2\varepsilon_\infty + \frac{\varepsilon_s - \varepsilon_2}{1 + i\omega\tau_1} + \frac{\varepsilon_2 - \varepsilon_\infty}{1 + i\omega\tau_2} \\ &+ \frac{1}{2} (\varepsilon_s - \varepsilon_\infty) \left[\frac{1 + i\omega_0\tau}{1 + i(\omega - \omega_0)\tau} + \frac{1 - i\omega_0\tau}{1 + i(\omega + \omega_0)\tau} \right]\end{aligned} \qquad (6.31).$$

Equation 6.31 is termed as the double Debye resonant absorption (DDRA) model. Figure 6.5 shows the frequency variation of dielectric dispersion and loss spectrum of HER2 and HEWL in aqueous solution and the fitting results using Equation 6.31. Table 6.4 gives the fitting parameters in detail. The concentration of HER2 and HEWL used for the data of Figure 6.5 was 5 mg/ml. From previous work by Grant *et al.* [181], since a substantial proportion of the water is, on average, many molecules away from the nearest protein molecule these could be assigned the relaxation time of bulk water. Actually, this process can be described by τ_1 which has a very similar value when compared to that of bulk water (τ_1 = 8.6 ps). Considering that the molecular size of the protein is very large when compared to water, the value τ can be clearly assigned to the rotational relaxation of the protein molecules

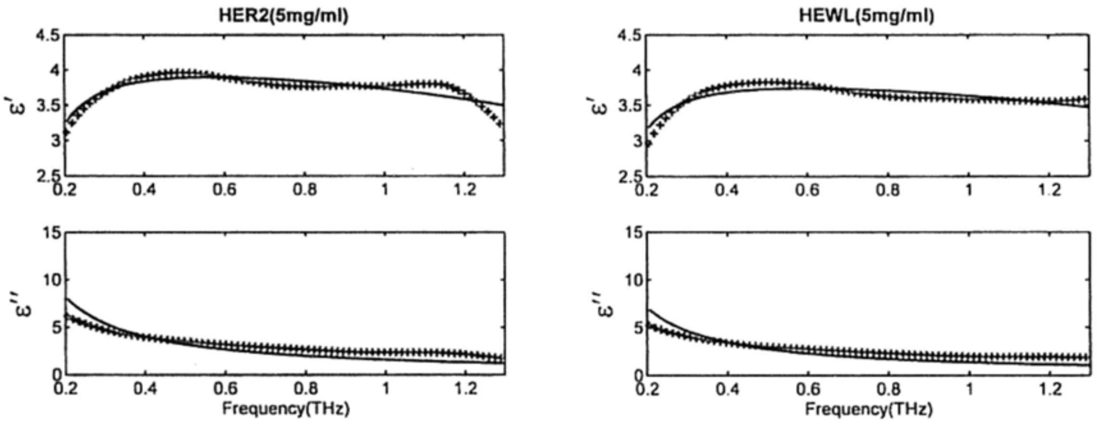

(a) (b)

Figure 6.5: Dielectric dispersion, $\varepsilon'(\omega)$, and loss spectrum, $\varepsilon''(\omega)$, of HER2 and HEWL at 5 mg/ml fitted by Equation 6.31.

themselves, as it is of the order of nanoseconds which far more than the relaxation time of the hydrogen bond in water (τ_{HB}=0.54 ps) which has been determined by Conde and Teixeira [182]. The intermediate relaxation process τ_2 can also be interpreted in terms of the so-called δ-dispersion, characterized for the interaction in the protein solutions [183].

Furthermore, the fitting parameters for HER2 and HEWL at 2.5 mg/ml were also determined in this study. When compared to the higher concentration (5 mg/ml), we found that the dispersion of the whole system $\Delta\varepsilon(\Delta\varepsilon = \varepsilon_s - \varepsilon_\infty)$ increased and the resonant frequencies shift to the higher frequencies with the fraction of water increased, the shifting rate for HER2 is larger than HEWL. Considering the relaxation process separately, the dispersion $\Delta\varepsilon_1(\Delta\varepsilon_1 = \varepsilon_s - \varepsilon_2)$ increased from 108.6 to 253.7 for HER2 and from 113.9 to 143.2 for HEWL. However, $\Delta\varepsilon_2(\Delta\varepsilon_2 = \varepsilon_s - \varepsilon_\infty)$ has decreased which suggests that the intermediate relaxation process has been shortened because more hydrogen-bonds have been added in.

Figure 6.6 shows the frequency dependent dielectric dispersion for two kinds of IgG protein solution system (PX-IgG and FITC-IgG in Chapter 5 in details). The solid black curves are fits using Equation 6.31 and the fitting parameters are shown in Table 6.5.

	ε_s	ε_∞	ε_2	$\varepsilon_1(ps)$	$\varepsilon_2(ps)$	ω_0	$\tau(ns)$
HER2(5mg/ml)	471.2	237.9	362.6	8.3	7.4	26.2	10.77
HER2(2.5mg/ml)	558.4	281.3	304.7	8.4	7.1	30.4	10.59
HEWL(5mg/ml)	424.6	215.1	310.7	8.2	6.8	29.1	14.28
HEWL(2.5mg/ml)	455.1	230.2	311.9	8.4	6.1	30.2	10.59

Table 6.4: Dielectric parameters of HER2 and HEWL in aqueous solutions at the concentration by 2.5 and 5 mg/ml fitting based on Equation 6.6.

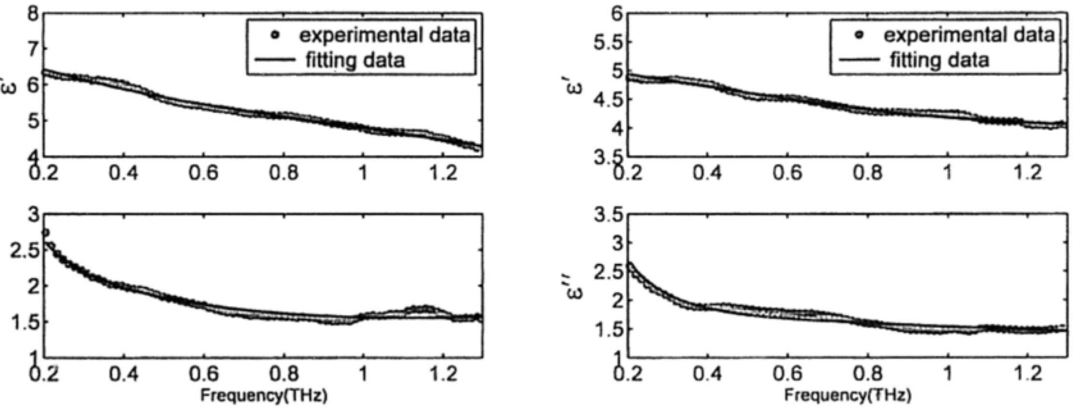

(a) (b)

Figure 6.6: Dielectric dispersion, $\varepsilon'(\omega)$, and loss spectrum, $\varepsilon''(\omega)$, of (a) PX-IgG and (b) FITC-IgG fitted by Equation 6.31.

Here we have observed that the interpretation of fitting parameters from protein liquids has traditionally relied on a frequency separation between relaxation and resonant absorption regimes. Spectral features in the low-frequency, relaxation or oscillatory motion of a molecule (or group of molecules) yields information about the "relaxation" or exponential decay of correlation at shorter times. The onset of relaxation behavior is not necessarily well defined but is expected to fall in the *ps* range, suitable for probing by the 0.1-3 THz bandwidth of the fs THz spectrometer. Resonant absorption occurs slowly enough, which reflects the changes in the environment, yields at the higher frequency.

	ε_s	ε_∞	ε_2	$\varepsilon_1(ps)$	$\varepsilon_2(ps)$	ω_0	$\tau(ns)$
Water/glycerol	65	3.22	5.34	20.78	0.13		
PX-IgG	119	61.5	63.9	21.14	0.20	16.6	9.59
FITC-IgG	142	72.6	74.8	20.49	0.10	282.3	5.13

Table 6.5: Dielectric parameters of PX-IgG and FITC-IgG in glycerol/water solutions at the concentration by 0.8 mg/ml fitting based on Equation 6.6, and the best fits for glycerol/water mixtures using double Debye relaxation model.

6.8 Summary

In this chapter, we have demonstrated the dielectric theories on solutions which have been derived from the general dielectric theory. Also, Debye relaxation models were introduced in order to fit the dielectric properties of liquid samples. The results presented show the application of three dielectric relaxation models (single Debye, multi-Debye and Davidson-Cole model) which have long been known to describe dielectric behavior below 100 GHz, for water, polar and non-polar liquids up to at least 1.2 THz. Furthermore, we have introduced a novel DDRA model to describe the interaction between the protein and its solvent molecule which provide good fits to the experimentally determined complex dielectric constant. It should be noted that TDS-THz pulses are ideally suited to probe picosecond and subpicosecond transient behavior of protein molecules in the liquid phase in the FIR region.

Chapter 7

Conclusions and Further Work

This thesis covers both theoretical and experimental studies on the interaction of THz radiation with biomolecular systems. The experimental samples, from macroscopic tissues to microscopic proteins, were investigated using both reflection and transmission geometry systems. Furthermore, modeling techniques implemented using the Debye relaxation model provide further insight into the interaction mechanisms between THz waves and protein-water systems. The proteins of interest presented in this work are some which may be used to determine and indicate the cause of organic damage. Our aim is to understand the THz properties of these proteins to determine whether THz technology can be deployed in various clinical applications in the further.

7.1 Contributions

1. We proposed that the terahertz properties were affected by the formalin fixing as it displaced water molecules and introduced new intermolecular interactions between the samples and the formalin.

2. We proposed that the dielectric properties of each solution containing an antibody were sensitive to the conjugation of the antibody added and denoted that charged protein solution hydrogen-bonded networks play an important role in determining the dielectric properties detected by terahertz spectroscopy.

3. We evaluated the depth of the hydrogen shell for each antibody which presented the hydrogen dynamic effects of the antibody in the terahertz frequency.

4. We performed the observation of distinct differences at low as well as at room temperature demonstrate that terahertz spectroscopy can be used to distinguish the anharmonicity of the vibrational potential which relates to the strength of the reset force of the oscillating system in the HER2 molecule.

5. Finally, we developed a novel model (DDRA model) to describe the interaction between the protein and its solvent molecule which provide good fits to the experimentally determined complex dielectric constant.

7.2 Discussion

In Chapter 3, a controlled study to investigate the effects of formalin fixing on the terahertz properties of two different tissue types (porcine adipose tissue and muscle) was presented. The optical properties of fresh and formalin fixed samples in the terahertz frequency range were measured using THz reflection spectroscopy. The terahertz properties were affected by the formalin fixing as it displaced water molecules and introduced new intermolecular interactions between the sample and the formalin. It is well known that terahertz radiation is sensitive to hydrogen bonding and thus water content changes. Additionally we infer that the newly introduced intermolecular interactions may also have contributed to the terahertz response. In our example study of adipose tissue and muscle the fixing process reduced the differences between the absorption coefficient and refractive index. However in this case there were still significant enough differences between the parameters for the two tissue types to be distinguished. In cases where the differences between tissues are more subtle, this may not be the case, and formalin fixing may prevent terahertz imaging from being able to distinguish the samples.

After investigating the ability to distinguish the different samples at the tissue level using THz reflection spectroscopy, two types of antibodies, which only differ in their molecular conformation in the conjugation pattern; namely whether it is peroxidase or fluorescein conjugated, have been determined in Chapter 4. A modified hand-held reflective geometry THz-TDS system was adopted. In this chapter, a general introduction for the glycerol solution was given in order to explain what the role it played in the antibody solution in this study. Then, as a step toward the exploration of the interaction between the proteins (antibodies) with their solvent (glycerol) molecules, absorption coefficients of antibody-glycerol solution in various concentrations were probed. The results clearly indicated that the absorption coefficient was not consistent with the linear changes in the glycerol solution based on the assumption of Beer's law. Thus, we compared the THz absorption coefficient with the effect of various concentration of glycerol solution on the protein refolding reaction which was published by *Roman V. Rariy* at 1997 and got the proof that refolding reaction of solute (antibody) happened in the ternary glycerol-water-protein system.

In addition, the complex permittivity responses of the solvent and the proteins in solution have been measured as a function of frequency. The response is strongly associated with the polarization arising from the polar liquids' network of hydrogen bonding. The presence of different antibodies affected the solution uniquely such that the dielectric properties of each solution containing an antibody were sensitive to the conjugation of the antibody added. This highlights that charged protein solutions' hydrogen-bonded networks play an important role in determining the dielectric properties detected by terahertz spectroscopy.

A transmission THz-TDS system was used in Chapter 5 to investigate another cancer marker protein (HER2/neu). In the aqueous phase, the terahertz response is mainly determined by relaxational response of side chains within the protein and the energy barriers for these motions are hydration dependent which can be denoted by temperature; in solid phase, some vibration features can be probed in THz range and the synchrotron spectrum was compared as an substance.

For model selection in Chapter 6, we represented the application of three dielectric relaxation models (single Debye, multi-Debye and Davidson-Cole model) for water, polar and non-polar liquids up to at least 1.2 THz. Furthermore, we have deduced a novel model which combined relaxation process and resonance absorption effects to describe the interaction between the protein and its solvent molecule which provide good fits to the experimentally determined complex dielectric constant.

7.3 Further work

The work described in the thesis can be extended in a number of ways, and several interesting problems are worthy of investigation. Our feeling is that some details of the vibrational behavior of proteins is still unexplored, mainly because of the narrow frequency bandwidth used in the investigation. In some aspects the Debye dielectric function may be more general and useful in the analysis of various relaxation phenomena, in particular, in the study of dielectric dispersion and absorption, but one of the open problems is that the Debye dielectric function $\varepsilon(\omega)$ does not decrease quickly enough with frequency ω to satisfy the sum rule. Namely the unphysical short-time behavior is related to the Debye model. So that is why we have introduced the resonant absorption effects into the understanding of the complex protein solution system. In further work we will also investigate different dielectric relaxation models of liquids and distribution functions for more complex protein-liquid systems, so as to understand and relate the measurements to the molecular changes occurring.

Author's Publications

Journal Papers

- **Y.W. Sun**, B. M. Fischer and E. Pickwell-MacPherson, "Effects of Formalin Fixing on the Terahertz Properties of Biological Tissues," *J. Biomed. Opt.*, 14, 064017(1-7), 2009.
- **Y.W. Sun**, Y. T. Zhang and E. Pickwell-MacPherson, "Investigating antibody interactions with a polar liquid using terahertz pulsed spectroscopy," *Biophys. J.*, 2010, (Submitted).
- E. Pickwell-MacPherson, S.Y. Huang, K. Kan, **Y.W. Sun** and Y.T. Zhang, "Recent Developments of Terahertz Technology in Biomedicine," *Journal of Innovation in Optical Health Sciences*, 1, 29-44, 2008.
- Y. Chen, **Y.W. Sun**, K. Kan and E. Pickwell-MacPherson, "Total Variation Deconvolution for Terahertz Pulsed Imaging," *Inverse Problems In Science & Engineering*, 2009 (Accepted).

Conference Papers

- **Y.W. Sun,** Y. T. Zhang, E. Pickwell-MacPherson, "Probing Dielectric Relaxation Models of Polar Liquids using Terahertz Time-domain Pulsed Spectroscopy," *The 35th International Conference on Infrared, Millimeter, and*

Terahertz Waves, Roman, September 2010.

- **Y.W. Sun**, Y. T. Zhang, E. Pickwell-MacPherson, "Terahertz Dielectric Properties of Monoclonal Antibodies to Influenza," *The 6th International School and Symposium on Medical Devices and Biosensors, in conjunction with The 4th International School and Symposium on Biomedical and Health Engineering*, Shenzhen, December 2009.

- **Y.W. Sun**, E. Pickwell-MacPherson, "Probing Antibody Interactions with Polar Liquids using Terahertz Pulsed Spectroscopy," *The 34th International Conference on Infrared, Millimeter, and Terahertz Waves*, Busan, September 2009.

- **Y.W. Sun**, E. Pickwell-MacPherson, "The Effects of Formalin Fixing on Terahertz Properties of Biological Samples," *The 33rd International Conference on Infrared, Millimeter, and Terahertz Waves, California*, September 2008.

- **Y.W. Sun**, E. Pickwell-MacPherson, "Non-invasive Tablet Inspection Using Terahertz Pulsed Imaging," *Proceedings of the 5th International Workshop on Wearable and Implantable Body Sensor Networks (BSN 2008)*, 217-219, June 2008.

- E. MacPherson, S.Y. Huang, **Y.W. Sun**, K. Kan and Y.T. Zhang, "Terahertz image processing methods for biomedical applications," *The 30th Annual International IEEE EMBS Conference*, British Columbia, Canada, August 2008.

Bibliography

[1] D. H. Auston, "Picosecond optoelectronic switching and gating in silicon," *Appl. Phys. Lett.*, vol. 26, pp. 101–103, 1975.

[2] P. H. Siegel, "Terahertz technology in biology and medicine," *IEEE Trans. Microwave. Theory Tech.*, vol. 52, pp. 2438–2447, 2004.

[3] S. W. Smye, J. M. Chamberlain, A. J. Fitzgerald, and E. Berry, "The interaction between Terahertz radiation and biological tissue," *Phys. Med. Biol.*, vol. 46, pp. R101–R112, 2001.

[4] C. M. Ciesla, D. D. Arnone, A. Corchia, D. Crawley, C. Longbottom, and E. H. Linfield, "Biomedical applications of terahertz pulse imaging commer," *Biomed. Appl. Ultrafast Lasers II*, vol. 3934, pp. 73–81, 2000.

[5] K. Kawase, Y. Ogawa, Y. Watanabe, and H. Inoue, "Non-destructive terahertz imaging of illicit drugs using spectral fingerprints," *Opt. Exp.*, vol. 11, pp. 2549–2554, 2003.

[6] L. Ning, S. Jingling, S. Jinhai, L. Laishun, X. Xiaoyu, L. Meihong, and J. Yan, "Study on the THz spectrum of methamphetamine," *Opt. Exp.*, vol. 13, pp. 6750–6755, 2005.

[7] S. Svanberg, *Atomic Molecular Spectroscopy.* Springer, Berlin, 1992.

[8] B. M. Fischer, "A comprehensive study of the dielectric properties of biomaterials in the far-infrared," Ph.D. dissertation, University of Freiburg, 2005.

[9] Y. C. Shen, T. Lo, P. F. Taday, B. E. Cole, W. R. Tribe, and M. C. Kemp, "Detection and identification of explosives using terahertz pulsed spectroscopic imaging," *Appl. Phys. Lett.*, vol. 86, art. no. 24116, 2005.

[10] M. C. Beard, G. M. Turner, and C. A. Schmuttenmaer, "Terahertz spectroscopy," *J. Phys. Chem. B*, vol. 106, pp. 7146–7159, 2002.

[11] R. H. Clothier and N. Bourne, "Effects of THz exposure on human primary keratinocyte differentiation and viability," *J. Biol. Phys.*, vol. 29, pp. 179–185, 2003.

[12] R. M. Woodward, B. E. Cole, and V. P. Wallace, "Terahertz pulse imaging of in vitro basal cell carcinoma samples," *In: Technical Digest-Postconference (ed.) Conference on Lasers and Electro-Optics (CLEO) TOPS*, vol. 56, pp. 329–330, 2001.

[13] R. M. Woodward, "Terahertz pulse imaging in reflection geometry of human skin cancer and skin tissue," *Phys. Med. Biol.*, vol. 47, pp. 3853–3863, 2002.

[14] R. M. Woodward, V. P. Wallace, and R. J. Pye, "Terahertz pulse imaging in reflection geometry of skin tissue using time domain analysis techniques," *In: Clinical Diagnostic Systems: Technology and Instrumentation, Proc. SPIE*, vol. 4625, no. 28, pp. 160–169, 2002.

[15] V. P. Wallace, D. Arnone, R. M. Woodward, and R. J. Pye, "Biomedical applications of terahertz pulsed imaging," *In Proc. 2nd Joint EMBS/BMES Conf., Houston, TX*, vol. 3, pp. 2333–2334, 2002.

[16] J. A. Fitzgerald, V. P. Wallace, M. Jimenez-Linan, L. Bobrow, R. J. Pye, A. D. Purushotham, and D. D. Arnone, "Terahertz pulsed imaging of human breast tumors," *Radiology*, vol. 239, pp. 533–540, 2006.

[17] P. Knobloch, C. Schildknecht, T. Kleine-Ostmann, M. Koch, S. Hoffmann, M. Hofmann, E. Rehberg, M. Sperling, K. Donhuijsen, G. Hein, and K. Pierz,

"Medical THz imaging: an investigation of histo-pathological samples," *Phys. Med. Biol.*, vol. 47, pp. 3875–3884, 2002.

[18] D. A. Crawley, C. Lonbottom, V. P. Wallace, B. E. Cole, D. D. Arnone, and M. Pepper, "Three-dimensional terahertz pulse imaging of dental tissue," *J. Biomed. Opt.*, vol. 8, pp. 303–307, 2003.

[19] E. Pickwell, "Biological applications of terahertz pulsed imaging and spectroscopy," Ph.D. dissertation, University of Cambridge, 2005.

[20] L. Ho, R. Muller, M. Romer, K. C. Godon, J. Heinamaki, P. Kleinebudde, M. Pepper, T. Rades, Y. C. Shen, C. J. Strachan, P. F. Taday, and J. A. Zeitler, "Analysis of sustained-release tablet film coats using terahertz pulsed imaging," *J. Contr. Rel.*, vol. 119, pp. 253–261, 2007.

[21] C. J. Strachan, T. Rades, D. A. Newnham, K. C. Gordon, M. Pepper, and P. F.Taday, "Using terahertz pulsed spectroscopy to study crystallinity of pharmaceutical materials," *Chem. Phys. Lett.*, vol. 390, pp. 20–24, 2004.

[22] P. F. Taday, I. V. Bradley, D. D. Arnone, and M. Pepper, "Using terahertz pulse spectroscopy to study the crystalline structure of a drug: a case study of the polymorphs of ranitidine hydrochloride," *J. Pharm. Sci.*, vol. 92, pp. 831–838, 2003.

[23] C. J. Strachan, P. F. Taday, D. A. Newnham, K. C. Gordon, J. A. Zeitler, M. Pepper, and T. Rades, "Using terahertz pulsed spectroscopy to quantify pharmaceutical polymorphism and crystallinity," *J. Pharm. Sci.*, vol. 94, pp. 837–846, 2005.

[24] J. A. Zeitler, D. A. Newnham, P. F. Taday, C. J. Strachan, M. Pepper, K. C. Gordon, and T. Rades, "Temperature dependent terahertz pulsed spectroscopy of carbamazepine," *Thermochim. Acta.*, vol. 436, pp. 71–77, 2005.

[25] J. A. Zeitler, D. A. Newnham, P. F. Taday, T. L. Threlfall, R. W. Lancaster, R. W. Berg, C. J. Strachan, K. C. Gordon, M. Pepper, and T. Rades, "Characterisation of temperature induced phase transitions in the five polymorphic forms of sulfathiazole by terahertz pulsed spectroscopy and differential scanning calorimetry," *J. Pharm. Sci.*, vol. 95, pp. 2486–2498, 2006.

[26] J. A. Zeitler, K. Kogermann, J. Rantanen, T. Rades, P. F. Taday, M. Pepper, J. Aaltonen, and C. J. Strachan, "Drug hydrate systems and dehydration process studied by terahertz pulsed spectroscopy," *Int. J. Phytorem.*, vol. 334, pp. 78–84, 2007.

[27] Y. C. Shen, P. F. Taday, D. A. Newnham, and M. Pepper, "Chemical mapping using reflection terahertz pulsed imaging," *Semicond. Sci. Technol.*, vol. 20, pp. S254–S257, 2005.

[28] M. C. Beard, G. Turner, and C. A. Schmuttenmaer, "Sub-picosecond carrier dynamics in low-temperature grown gaas as measured by time-resolved THz spectroscopy," *J. App. Phys.*, vol. 90, pp. 5915–5923, 2001.

[29] J. T. Kindt and C. A. Schmuttenmaer, "Far-infrared dielectric properties of polar liquids probed by femtosecond terahertz pulse spectroscopy," *J. Phys. Chem.*, vol. 100, pp. 10 373–10 379, 1996.

[30] K. J. Tielrooij, R. L. A. Timmer, H. J. Bakker, and M. Bonn, "Structure dynamics of the proton in liquid water probed with terahertz time-domain spectroscopy," *Phys. Rev. Lett.*, vol. 102, art. no. 198303, 2009.

[31] W. Withayachumnankul, G. M. Png, X. X. Yin, S. Atakaramians, I. Jones, H. Lin, B. S. Y. Ung, J. Balakrishnan, B. W. H. Ng, B. Ferguson, S. P. Mickan, B. M. Fischer, and D. Abbott, "T-Ray sensing and imaging," *Proc. IEEE*, vol. 95, pp. 1528–1558, 2007.

[32] C. J. Strachan, P. F. Taday, D. A. Newnham, K. C. Gordon, J. A. Zeitler, M. Pepper, and T. Rades, "Using terahertz pulsed spectroscopy to quantify pharmaceutical polymorphism and crystallinity," *J. Pharm. Sci.*, vol. 94, pp. 837–846, 2005.

[33] D. M. Mittleman, M. C. Nuss, and V. L. Colvin, "Terahertz spectroscopy of water in inverse micelles," *Chem. Phys. Lett.*, vol. 275, pp. 332–338, 1997.

[34] M. Walther, B. M. Fischer, M. Schall, H. Helm, and P. U. Jepsen, "Far-infrared vibrational spectra of all-trans 9-cis and 13-cis retinal measured by THz time-domain spectroscopy," *Chem. Phys. Lett.*, vol. 332, pp. 389–395, 2000.

[35] B. M. Fischer, M. Hoffmann, H. Helm, R. Wilk, F. Rutz, T. Kleine-Ostmann, M. Koch, and P. U. Jepsen, "Terahertz time-domain spectroscopy and imaging of artificial RNA," *Opt. Exp.*, vol. 13, pp. 5205–5215, 2005.

[36] B. M. Fischer, H. Helm, and P. U. Jepsen, "Chemical recognition with broadband THz spectroscopy," *Proc. IEEE*, vol. 95, pp. S246–S253, 2007.

[37] R. M. Woodward, V. P. Wallace, D. D. Arnone, E. H. Linfield, and M. Pepper, "Terahertz pulsed imaging of skin cancer in the time and frequency domain," *J. Biol. Phys.*, vol. 29, pp. 257–261, 2003.

[38] R. Pethig, "Protein-water interactions determined by dielectric methods," *Annu. Rev. Phys. Chem.*, vol. 43, pp. 177–205, 1992.

[39] M. Walther, "Modern spectroscopy on biological molecules: Structure and bonding investigated by THz time-domain and transient phase-grating spectroscopy," Ph.D. dissertation, University of Freiburg, 2003.

[40] D. M. Mittleman, *Sensing with Terahertz Radiation.* Springer, Berlin, 2003.

[41] E. Pickwell, B. E. Cole, A. J. Fitzgerald, M. Pepper, and V. P. Wallace, "In vivo study of human skin using pulsed terahertz radiation," *Phys. Med. Biol.*, vol. 49, pp. 1595–1607, 2004.

[42] S. Y. Huang, E. Pickwell-Macpherson, and Y. T. Zhang, "A new data processing approach to reduce variations in terahertz pulsed imaging," *Proc. Int. Workshop on Wearable and Implantable Body Sensor Networks (BSN 2008),in conjunction with the 5th Int. Summer School and Symposium on Medical Devices and Biosensors*, pp. 236–239, 2008.

[43] L. Duvillaret, F. Garet, and J. Coutaz, "Highly precise determination of optical constants and sample thickness in terahertz time-domain spectroscopy," *Appl. Opt.*, vol. 39, pp. 409–415, 1999.

[44] E. Pickwell, V. P. Wallace, A. J. Fitzgerald, B. E. Cole, R. J. Pye, T. Ha, and M. Pepper, "Simulating the response of terahertz radiation to human skin using ex vivo spectroscopy measurements," *J. Biomed. Opt.*, vol. 10, art. no. 064021, 2005.

[45] V. P. Wallace, A. J. Fitzgerald, E. Pickwell, R. J. Pye, P. F. Taday, N. Flanagan, and T. Ha, "Terahertz pulsed spectroscopy of human basal cell carcinoma," *Appl. Spectrosc.*, vol. 60, pp. 1127–1133, 2006.

[46] S. Y. Huang, Y. X. J. Wang, D. K. W. Yeung, A. T. Ahuja, Y. T. Zhang, and E. Pickwell-MacPherson, "Tissue characterisation using terahertz pulsed imaging in reflection geometry," *Phys. Med. Biol.*, vol. 54, pp. 149–160, 2009.

[47] G. M. Png, J. W. Choi, B. W.-H. Ng, S. P. Mickan, D. Abbott, and X.-C. Zhang, "The impact of hydration changes in fresh bio-tissue on THz spectroscopic measurements," *Phys.Med. Biol.*, vol. 53, pp. 3501–3517, 2008.

[48] H. Hoshina, A. Hayashi, N. Miyoshi, F. Miyamaru, and C. Otani, "Terahertz pulsed imaging of frozen biological tissues," *Appl. Phys. Lett.*, vol. 94, art. no. 123901, 2009.

[49] R. C. Grafstrom, A. Fornace, Jr., and C. C. Harris, "Repair of DNA damage caused by formaldehyde in human cells," *Cancer Res.*, vol. 44, pp. 4323–4327, 1984.

[50] P. Knobloch, K. Schmalstieg, M. Koch, E. Rehberg, F. Vauti, and K. Donhuijsend, "THz imaging of histo-pathological samples," *Proc. SPIE*, vol. 4434, pp. 239–245, 2001.

[51] S. Y. Huang, Y. X. J. Wang, D. K. W. Yeung, A. T. Ahuja, Y. T. Zhang, and E. Pickwell-MacPherson, "Tissue characterization using terahertz pulsed imaging in reflection geometry," *Phys.Med. Biol.*, vol. 54, pp. 149–160, 2009.

[52] B. E. Cole, R. Woodward, D. Crawley, V. P. Wallace, D. D. Arnone, and M. Pepper, "Terahertz imaging and spectroscopy of human skin, in-vivo," *Proc. SPIE-Int. Soc.Opt. Eng.*, vol. 4276, pp. 1–10, 2001.

[53] M. H. Hofker and J. V. Deursen, *Methods in Molecular Biology.* Humana Press, New Jersey, 2002.

[54] L. C. Junqueira, *Basic Histology: Text & Atlas.* McGraw-Hill, New York, 2005.

[55] D. W. Cromey, *Formaldehyde Fixatives.* University of Arizona, 2004.

[56] L. Johannes and V. H. Robert, *Applied Statistics for Engineers and Physical Scientists.* Prentice Hall, New Jersey, 2009.

[57] M. R. Stringer, D. N. Lund, A. P. Foulds, A. Uddin, E. Berry, R. E. Miles1, and A. G. Davies, "The analysis of human cortical bone by terahertz time-domain spectroscopy," *Phys. Med. Biol.*, vol. 50, pp. 3211–3219, 2005.

[58] C. L. Nie, W. Zhang, D. Zhang, and R. Q. He, "Changes in conformation of human neuronal tau during denaturation in formaldehyde solution," *Protein Peptide Lett.*, vol. 12, pp. 75–78, 2005.

[59] J. F. Walker, *Formaldehyde*. Reinhold, New York, 1964.

[60] C. H. Fox, F. B. Johnson, J. Whiting, and P. P. Roller, "Formaldehyde fixation," *J. Histochem. Cytochem.*, vol. 33, pp. 845–853, 1985.

[61] A. Younge, C. F. V. Niekerk, and S. Mogotlane, *Juta's Manual of Nursing*. Juta & Company, South Africa, 2003.

[62] A. Markelz, A. Roitberg, and E. J. Heilweil, "Pulsed terahertz spectroscopy of DNA, bovine serum albumin and collagen between 0.06 to 2.00 THz," *Chem. Phys. Lett.*, vol. 320, pp. 42–48, 2000.

[63] A. Markelz, S. Whitmire, J. Hillebrecht, and R. Birge, "The time domain spectroscopy of biomolecular conformational modes," *Phys. Med. Biol.*, vol. 47, pp. 3797–3805, 2002.

[64] B. M. Fischer, M. Walther, and P. U. Jepsen, "Far-infrared vibrational modes of DNA components studied by terahertz time-domain spectroscopy," *Phys. Med. Biol.*, vol. 47, pp. 3807–3814, 2002.

[65] J. E. Yardley, D. Kell, J. Barrett, and C. L. Davey, "On-line, real-time measurements of cellular biomass using dieletric spectroscopy," *Biotechnol. Genet. Eng. Rev.*, vol. 17, pp. 3–35, 2000.

[66] K. C. Schuster, "Monitoring the physiological status in bioprocesses on the cellular level," *Adv. Biochem. Eng. Biotechnol.*, vol. 66, pp. 185–208, 2000.

[67] K. Asami, "Characterization of heterogeneous systems by dielectric spectroscopy," *Progr. Polym. Sci.*, vol. 27, pp. 1617–1659, 2002.

[68] F. Pedone and A. Bonincontro, "Temperature dependence of DNA dielectric dispersion at radiofrequency," *Biochim. Biophys. Acta.*, vol. 1073, pp. 580–584, 1991.

[69] J. Laudat and F. Laudat, "Dielectric study of charge motion in DNA," *Eur. Biophys. J.*, vol. 21, pp. 233–239, 1992.

[70] V. Degouys, I. Cerckel, A. Garcia, J. Harfeld, D. Dubois, L. Fabry, and A. O. Miller, "Dielectric spectroscopy of mammalian cells - 2. simultaneous in situ evaluation by aperture impedance pulse spectroscopy and low frequency dielectric spectroscopy of the biomass of HTC cells on cytodex 3," *Cytotechnology.*, vol. 13, pp. 195–202, 1993.

[71] A. Bonincontro, G. Melucci-Vigo, and G. Risuleo, "Mouse polyomavirus mediated effects on the infected cell membrane studied by dielectric spectroscopy," *Biosci. Rep.*, vol. 13, pp. 259–263, 1993.

[72] M. P. Gretel, R. J. Falconer, B. M. Fischer, H. A. Zakaria, S. P. Mickan, A. P. J. Middelberg, and D. Abbott, "Terahertz spectroscopic differentiation of microstructures in protein gels," *Opt. Express.*, vol. 17, pp. 13 102–1115, 2009.

[73] M. R. Kutteruf, C. M. Brown, L. K. Iwaki, M. B. Campbell, T. M. Korter, and E. J. Heilweil, "Terahertz spectroscopy of short-chain polypeptides," *Chem. Phys. Lett.*, vol. 375, pp. 337–343, 2003.

[74] K. Joseph, J. Y. Chen, and A. Markelz, "Hydration dependence of conformational dielectric relaxation of lysozyme," *Biophys. J.*, vol. 90, pp. 2576–2581, 2006.

[75] R. A. Rhoades and R. Pflanzer, *Human Physiology*. Pacific Grove, California, 2002.

[76] K. M. Boberg, E. Aadland, J. Jahnsen, N. Raknerud, M. Stiris, and H. Bell, "Incidence and prevalence of primary biliary cirrhosis, primary sclerosing cholangitis, and autoimmune hepatitis in a norwegian population," *Scand. J. Gastroentero.*, vol. 33, pp. 99–103, 1998.

[77] L. Stryer, *Biochemistry*. W. H. Freeman, New York, 1998.

[78] A. Bruce, A. Johnson, J. Lewis, M. Raff, K. Roberts, and P. Walters, *The Shape and Structure of Proteins, Molecular Biology of the Cell*. New York and London, Garland Science, 2002.

[79] L. M. Gierasch and J. King, *Protein Folding*. Am. Assoc. Adv. Sci., Washington, DC, 1990.

[80] T. E. Creighton, *Protein Folding*. W. H. Freeman, New York, 1992.

[81] P. S. Kim and R. L. Baldwin, "Intermediates in the folding reactions of small proteins," *Annu. Rev. Biochem.*, pp. 631–660, 1990.

[82] B. K. Nall and K. A. Dill, *Conformations and Forces in Protein Folding*. Am. Assoc. Adv. Sci., Washington, DC, 1991.

[83] K. M. Merz and L. S. M. Grand, *The Protein Folding Problem and Tertiary Structure Prediction*. Birkhauser, Boston, 1994.

[84] K. A. Dill, S. Bromberg, K. Z. Yue, K. M. Fiebig, D. P. Yee, P. D. Thomas, and H. S. Chan, "Principles of protein folding: A perspective from simple exact models," *Protein Sci.*, vol. 4, pp. 561–602, 1995.

[85] http://en.wikivisual.com/index.php/Glycerol.

[86] F. G. Meng, Y. D. Park, and H. M. Zhou, "Role of proline, glycerol, and heparin as protein folding aids during refolding of rabbit muscle creatine kinase," *Int. J. Biochem. Cell. B.*, vol. 33, pp. 701–709, 2001.

[87] R. V. Rariy and A. M. Klibanov, "Correct protein folding in glycerol," *Proc. Natl. Acad. Sci. USA.*, vol. 94, pp. 13 520–13 523, 1997.

[88] K. Gekko and S. N. Timasheff, "Mechanism of protein stabilization by glycerol: preferential hydration in glycerol-water mixtures," *Biochemistry*, vol. 20, pp. 4667–4676, 1981.

[89] M. S. Lehmann and G. Zaccai, "Neutron small-angle scattering studies of ribonuclease in mixed aqueous solutions and determination of the preferentially bound water," *Biochemistry*, vol. 23, pp. 1939–1942, 1984.

[90] H. Tachibana, K. Ohta, H. Sawano, Koumoto, and S. Segawa, "Relationship between the optimal temperature for oxidative refolding and the thermal stability," *Biochemistry*, vol. 33, pp. 15 008–15 016, 1994.

[91] R. V. Rariy and A. M. Klibanov, "Correct protein folding in glycerol," *Proc Natl Acad Sci USA*, vol. 94, pp. 13 520–13 523, 1997.

[92] T. Knubovets, J. J. Osterhout, P. J. Connolly, and A. M. Klibanov, "Structure, thermostability, and conformational flexibility of hen egg-white lysozyme dissolved in glycerol," *Proc. Natl. Acad. Sci. USA*, vol. 96, pp. 1262–1267, 1999.

[93] J. D. Bryngelson, J. N. Onuchic, N. D. Socci, and P. G. Wolynes, "Funnels, pathways, and the energy landscape of protein folding: A synthesis," *Proteins: Struct., Funct., Genet.*, vol. 21, pp. 167–195, 1995.

[94] J. N. Onuchic, Z. Luthey-Schulten, and P. G. Wolynes, "Theory of protein folding: The energy landscape perspective," *Annu. Rev. Phys. Chem.*, vol. 48, pp. 545–600, 1997.

[95] D. L. Nelson and M. M. Cox, *Lehninger Principles of Biochemistry.* W.H. Freeman, San Francisco, 2004.

[96] A. Markelz, S. Whitmire, J. Hillebrecht, and R. Birge, "THz time domain spectroscopy of biomolecular conformational modes," *Phys. Med. Biol.*, vol. 47, pp. 3797–3805, 2002.

[97] S. M. Smye, J. M. Chamberlain, A. J. Fitzgerald, and E. Berry, "The interaction between terahertz radiation and biological tissue," *Phys. Med. Biol.*, vol. 46, pp. R101–R112, 2001.

[98] E. W. Prohofsky, L. L. V. Zandt, M. Kohli, K. C. Lu, M. N. Mei, and B. Putnam, "Phonons in the DNA double helix," *J. de Physique*, vol. 42, pp. C6–560, 1981.

[99] J. A. McCammon and S. C. Harvey, *Dynamics of Proteins and Nucleic Acids*. Cambridge University Press, Cambridge, 1987.

[100] S. M. Lindsay, S. A. Lee, T. Weidlich, C. Demarco, G. D. Lewen, N. J. Tao, and A. Rupprecht, "The origin of the A to B transition in DNA fibers and films," *Biopolymers.*, vol. 27, pp. 1015–1043, 1988.

[101] P. W. Fenimore, H. Frauenfelder, B. H. McMahon, and F. G. Parak, "Slaving: Solvent fluctuations dominate protein dynamics and functions," *Proc. Nat. Acad. Sci. USA*, vol. 99, pp. 16 047–16 051, 2002.

[102] A. Ansari, J. Berendzen, S. F. Bowne, H. Frauenfelder, I. E. T. Iben, T. B. Sauke, E. Shyamsunder, and R. D. Young, "Protein states and protein quakes," *Proc. Nat. Acad. Sci. USA*, vol. 82, pp. 5000–5004, 1985.

[103] F. Despa, A. Fernández, and R. Berry, "Dielectric modulation of biological water," *Phys. Rev. Lett.*, vol. 93, art. no. 228104, 2004.

[104] C. Rønne, L. Thrane, P. Astrand, A. Wallqvist, K. V. Mikkelsen, and S. R. Keiding, "Investigation of the temperature dependence of dielectric relaxation in liquid water by THz reflection spectroscopy and molecular dynamics simulation," *J. Chem. Phys.*, vol. 107, pp. 5319–5330, 1997.

[105] M. C. Beard, G. M. Turner, and C. A. Schmuttenmaer, "Terahertz spectroscopy," *J. Phys. Chem. B*, vol. 106, pp. 7146–7159, 2002.

[106] A. Bergner, U. Heugen, E. Brundermann, G. Schwaab, M. Havenith, D. R. Chamberlin, and E. E. Haller, "New p-Ge THz laser spectrometer for the study of solutions: THz absorption spectroscopy of water," *Rev. Sci. Inst.*, vol. 76, art. no. 063110, 2005.

[107] S. Ebbinghaus, S. J. Kim, M. Heyden, X. Yu, U. Heugen, M. Gruebele, D. Leitner, and M. Havenith, "An extended dynamical hydration shell around proteins," *Proc. Nat. Acad. Sci. USA*, vol. 104, pp. 20 749–20 752, 2007.

[108] J. Y. Chen, , J. R. Knab, J. Cerne, and A. G. Markelz, "Large oxidation dependence observed in terahertz dielectric response for cytochrome c," *Phys. Rev. E.*, vol. 72, pp. 040 901(1–4), 2005.

[109] J. Xu, K. W. Plaxco, and S. J. Allen, "Probing the collective vibrational dynamics of a protein in liquid water by terahertz absorption spectroscopy," *Prot. Sci.*, vol. 15, pp. 1175–1181, 2006.

[110] D. M. Leitner, M. Havenith, and M. Gruebele, "Biomolecule large-amplitude motion and solvation dynamics: modeling and probes from THz to X-rays," *Int. Rev. Phys. Chem.*, vol. 25, pp. 553–582, 2006.

[111] D. V. Matyushov, "Terahertz response of dipolar impurities in polar liquids: On anomalous dielectric absorption of protein solutions," *Phys. Rev. E*, vol. 81, art. no. 021914, 2010.

[112] T. Tassaing, Y. Danten, M. Besnard, E. Zoidis, and J. Yarwood, "A far infrared study of benzene-fluorinated benzene binary mixtures," *Chem. Phys.*, vol. 184, pp. 225–231, 1994.

[113] J. K. Seung, "Studies of protein-protein and protein-water interactions by small angle x-ray scattering, terahertz spectroscopy, asmos, and computer

simulation," Ph.D. dissertation, University of Illinois at Urbana-Champaign, Illinois, 2008.

[114] http://en.wikipedia.org/wiki/Immunoglobulin_G.

[115] R. Sinibaldi, M. G. Ortore, F. Spinozzi, F. Carsughi, H. Frielinghaus, S. Cinelli, G. Onori, and P. Mariani, "Preferential hydration of lysozyme in waterglycerol mixtures: a small angle neutron scattering study," *J. Chem. Phys.*, vol. 126, pp. 35 101–235 119, 2007.

[116] U. Heugen, G. Schwaab, E. Brundermann, M. Heyden, X. Yu, D. M. Leitner, and M. Havenith, "Solute induced retardation of water dynamics probed directly by THz spectroscopy," *Proc. Natl. Acad. Sci. USA.*, vol. 103, pp. 12 301–12 306, 2006.

[117] E. H. Grant, R. J. Sheppard, and G. P. South, *Dielectric Behaviour of Biological Molecules in Solution*. Oxford: Clarendon, 1978.

[118] P. F. Taday, I. V. Bradley, and D. D. Arnone, "Terahertz pulse spectroscopy of biological materials: L-glutamic acid," *J. Biol. Phys.*, vol. 29, pp. 109–115, 2003.

[119] P. F. Taday, I. V. Bradley, D. D. Arnone, and M. Pepper, "Using terahertz pulse spectroscopy to study the crystalline structure of a drug: A case study of the polymorphs of ranitidine hydrochloride," *J. Pharm. Sci.*, vol. 94, pp. 831–838, 2003.

[120] M. Walther, B. M. Fischer, and P. U. Jepsen, "Noncovalent intermolecular forces in polycrystalline and amorphous saccharides in the far infrared," *Chem. Phys.*, vol. 288, pp. 261–268, 2003.

[121] S. N. Vinogradov and R. H. Linnell, *Hydrogen Bonding*. Van Nostrand-Reinhold, New York, 1971.

[122] A. D'Aprano, D. I. Donato, and E. Caponetti, "The static dielectric constant of solutions of water in n-alcohols at 15, 25, 35, and 45°C," *J.Sol.Chem.*, vol. 8, pp. 135–146, 1979.

[123] R. Buchner, G. T. Hefter, and P. M. May, "Dielectric relaxation of aqueous NaCl solutions," *J. Phys. Chem. A.*, vol. 103, pp. 1–9, 1999.

[124] J. B. Hubbard, L. Onsager, W. van Beek, and M. Mandel, "Kinetic polarization deficiency in electrolyte solutions," *Proc. Natl. Acad. Sci. USA.*, vol. 74, pp. 401–404, 1977.

[125] R. C. Mellors, "The application of labeled antibody technics in studying cell antigens," *Cancer. Res.*, vol. 28, pp. 1372–1381, 1968.

[126] J. E. Herrmann, S. A. Morse, and M. F. Collins, "Comparison of techniques and immunoreagents used for indirect immunofluorescence and immunoperoxidase identification of enteroviruses," *Infect Immun.*, vol. 10, pp. 220–226, 1974.

[127] M. Levitt, C. Sander, and P. S. Stern, "Protein normal-mode dynamics: trypsin inhibitor, crambin, ribonuclease and lysozyme," *J. Mol. Biol.*, vol. 181, pp. 423–427, 1985.

[128] http://www.piercenet.com/Objects/view.cfm?type=Page&ID = 412BAC2E-F0BC-4ABA-A79B-887E413910AB.

[129] H. Betting, M. H. ckel, H.-J. Hinz, and M. Stockhausen, "Spectroscopic evidence for the referential hydration of RNase A in glycerol/water mixtures: Dielectric relaxation studies," *Phys. Chem. Chem. Phys.*, vol. 3, pp. 1688–1692, 2001.

[130] B. Brooks and M. Karplus, "Normal modes for specific motions of macromolecules: Application to the hinge bending mode of lysozyme," *Proc. Nat. Acad. Sci. USA*, vol. 82, pp. 4995–4999, 1985.

[131] Y. Seno and N. Go, "Deoxymyoglobin studied by the conformational normal mode analysis," *J. Mol. Biol.*, vol. 216, pp. 111–126, 1990.

[132] M. Walther, B. Fischer, M. Schall, H. Helm, and P. U. Jepsen, "Far-infrared vibrational spectra of all-trans, 9-cis and 13-cis retinal measured by THz time-domain spectroscopy," *Chem. Phys. Lett.*, vol. 332, pp. 389–395, 2000.

[133] T. M. Korter and D. F. Plusquellic, "Continuous-wave terahertz spectroscopy of biotin: Vibrational anharmonicity in the far-infrared," *Chem. Phys. Lett.*, vol. 385, pp. 45–51, 2004.

[134] M. R. Kutteruf, C. M. Brown, L. K. Iwaki, M. B. Campbell, T. M. Korter, and E. J. Heilweil, "Terahertz spectroscopy of short-chain polypeptides," *Chem. Phys. Lett.*, vol. 375, pp. 337–343, 2003.

[135] H. J. S. Dawkins, P. D. Robbins, K. L. Smith, M. Sarna, J. M. Harvey, G. F. Sterrett, and J. M. Papadimitriou, "What's new in breast cancer? molecular perspectives of cancer development and the role of the oncogene c-erbB-2 in prognosis and disease," *Pathol. Res. Pract.*, vol. 189, pp. 1233–1252, 1993.

[136] http://lysozyme.co.uk/lysozyme structure.php.

[137] http://en.wikipedia.org/wiki/Lysozyme.

[138] R. K. Joseph, J. Y. Chen, Y. F. He, and A. G. Markelz, "Terahertz measurements of protein relaxational dynamics," *Proc. IEEE*, vol. 95, pp. 1605–1610, 2007.

[139] P. Debye, *Polar Molecules*. New York, Chern. Cat. Co., 1929.

[140] T. D. Kuntz, "Tertiary structure in carboxypeptidase," *J. Am. Chem. Soc.*, vol. 94, pp. 11–19, 1972.

[141] T. J. Buchanan, G. H. Haggis, J. B. Hasted, and B. G. .Robinson, "The dielectric estimation of protein hydration," *Proc. R. Soc. London*, vol. A213, pp. 379–391, 1952.

[142] J. Knab, J. Y. Chen, and A. Markelz, "Hydration dependence of conformational dielectric relaxation of lysozyme," *Biophys. J.*, vol. 90, pp. 2576–2581, 2006.

[143] V. A. Berstein and V. A. Ryzhov, "Far infrared spectroscopy of polymers," *Adv. Polym. Sci.*, vol. 114, pp. 45–119, 1994.

[144] S. Krimm and M. Bank, "Assignment of 71-cm^{-1} band in polyethylene," *J. Chem. Phys.*, vol. 42, pp. 4059–4060, 1965.

[145] http://www.lls.cells.es/AboutUs/WhatIs.

[146] M. Schall and P. U. Jepsen, "Photoexcited GaAs surfaces studied by transient THz time-domain spectroscopy," *Opt. Lett.*, vol. 25, pp. 13–15, 2000.

[147] E. Pickwell, B. E. Cole, A. J. Fitzgerald, V. P. Wallace, and M. Pepper, "In vivo study of human skin using pulsed terahertz radiation," *J. Phys. Med. Biol.*, vol. 49, pp. 1595–1607, 2004.

[148] P. U. Jepsen, U. Moller, and H. Merbold, "Investigation of aqueous alcohol and sugar solutions with reflection terahertz time-domain spectroscopy," *Optics Express.*, vol. 15, pp. 14 717–14 737, 2007.

[149] J. Barthel, K. Bachhuber, R. Buchner, and H. Hetzenauer, "Dielectric spectra of some common solvents in the microwave region. warer and lower alcohols," *Chem. Phys. Lett.*, vol. 165, pp. 369–373, 1990.

[150] http://hyperphysics.phy astr.gsu.edu/hbase/electric/dielec.html.

[151] R. Ronne, P. Astrand, and S. Keiding, "THz spectroscopy of liquid H_2O and D_2O," *Physical Review Letters*, vol. 82, no. 14, pp. 2888–2891, 1999.

[152] P. Debye, *Collected Papers of Peter J. W. Debye.* Interscience, New York, 1954.

[153] P. Debye, *Polar Molecules.* Chemical Catalog, New York, 1929.

[154] M. V. Exter, C. Fattinger, and D. Grischkowsky, "Terahertz time-domain spectroscopy of water vapor," *Opt. Lett.*, vol. 14, pp. 1128–1130, 1989.

[155] J. M. Flaud, C. Camy-Peyret, and R. A. Toth, Water Vapour Line Parameters from Microwave to Medium Infrared. Pergamon, Oxford, 1981.

[156] C. Ronne and S. R. Keiding, "Low frquency spectroscopy of liquid water using THz-time domain spectroscopy," *J. Molecular Liquids*, vol. 101, no. 1-3, pp. 199–218, 2002.

[157] T. T. L. Kristensen, W. Withayachumnankul, P. U. Jepsen, and D. Abbott, "Modeling terahertz heating effects on water," *Opt. Express*, vol. 18, pp. 4727–4739, 2010.

[158] H. J. Liebe, G. A. Hufford, and T. Manabe, "A model for the complex permittivity of water at frequencies below 1 THz," *Int. J. Infrared. Milimetre. Waves.*, vol. 12, pp. 659–674, 1991.

[159] E. H. Grant and T. J. Buchanan, "Dielectric behavior of water at microwave frequencies," *J. Chem. Phys.*, vol. 26, pp. 156–161, 1957.

[160] Http://www.web-books.com/MoBio/Free/Ch2C3.htm.

[161] J. B. Hasted, *In Water: A Comprehensive Treatise.* Plenum, New York, 1972.

[162] J. Barthel and R. Buchner, "High frequency permittivity and its use in the investigation of solution properties," *Pure. Appl. Chem*, vol. 63, pp. 1473–1482, 1991.

[163] G. C. Walker, E. Berry, S. W. Smye, N. N. Zinov'er, A. J. Fitzgerald, R. E. Miles, M. Chamberlain, and M. A. Smith, "Modelling the propagation of terahertz radiation through a tissue simulating phantom," *Physics in Medicine and Biology*, vol. 49, pp. 1853–1864, 2004.

[164] J. E. Pedersen and S. R. Keiding, "THz time-domain spectroscopy of nonpolar liquids," *IEEE J. Quantum. Electron.*, vol. 28, pp. 2518–2522, 1992.

[165] B. L. Yu, F. Zeng, Q. Xing, and R. R. Alfano, "Probing dielectric relaxation properties of liquid $cs2$ with terahertz time-domain spectroscopy," *Appl. Phys. Lett.*, vol. 82, pp. 4633–4635, 2009.

[166] C. F. J. Bottcher and P. Bordewijk, *Theory of Dielectric Polarization.* Elsevier, Amsterdam, 1978.

[167] M. Evans, G. J. Evans, W. T. Coffey, and P. Grigolini, *Molecular Dynamics and Theory of Broad Band Spectroscopy.* Wiley, New York, 1982.

[168] J. D. Simon, "Time-resolved studies of solvation in polar media," *Accounts. Chem. Res.*, vol. 21, pp. 128–134, 1988.

[169] M. Marconelli, E. W. C. Jr., B. Bagchi, and G. R. Fleming, "Faraday discussions," *Chem. Soc.*, vol. 85, pp. 199–210, 1988.

[170] S. K. Garg and C. P. Smyth, "Microwave absorption and molecular structure in liquids. LXII. the three dielectric dispersion regions of the normal primary alcohols," *J. Phys. Chem.*, vol. 69, pp. 1294–1301, 1965.

[171] F. Buckley and A. A. Maryott, *Table of Dielectric Dispersion Data for Pure Liquids and Dilute Solutions.* Bureau of Standards Circular: Washington, DC, USA, 1958.

[172] V. Holcman and A. Andreev, "Dielectric relaxation in glycerol at long-time exposure to low temperatures," *IEEE ISSE '08. 31st International Spring Seminar on Electronics Technology*, pp. 86–90, 2008.

[173] S. Havriliak and S. Negami, "A complex plane representation of dielectric and mechanical relaxation processes in some polymers," *Polymer.*, vol. 8, pp. 161–210, 1967.

[174] E. Ikada and T. Watanabe, "Dielectric relaxation of acrylonitrile-butadiene copolymers," *J. Poly. Sci. Poly. Chem.*, vol. 10, pp. 3457–3467, 1972.

[175] D. W. Davidson and R. H. Cole, "Dielectric relaxation in glycerol, propylene, and n-propanol," *J. Chem. Phys.*, vol. 19, pp. 1484–1490, 1951.

[176] E. Ikada, K. Yamamoto, and M. Ashida, "Dielectric properties of the hydrogen-bonded liquids. steric effects on dielectric properities in glycerol and acetylated glycerols," *Bull. Chem. Soc. Jpn.*, vol. 53, pp. 865–868, 1980.

[177] T. Globus, T. Khromova, B. Gelmont, D. Woolard, and L. K. Tamm, "Terahertz characterization of diluted DNA solutions," *Proc. SPIE Photonics West 2006 'Biomedical Vibrational Spectroscopy III: Advances in Research and Industry,' Biomed. Opt. Symp., San Jose, CA*, vol. 6093, pp. 50–61, 2006.

[178] C. F. Zhang, E. Tarhan, A. K. Ramdas, A. M. Weiner, and S. M. Durbin, "Broadened far-infrared absorption spectra for hydrated and dehydrated myoglobin," *J. Phys. Chem. B*, vol. 108, pp. 10 077–10 082, 2004.

[179] H. Frohlich, *Theory of Dielectrics*. Oxford University Press, London, 1958.

[180] W. Zhu, C. Li, G. Zhang, and G. Fang, "The calculation of dielectric dispersive models in THz range with GA," *Microw. Opt. Tech. Lett.*, vol. 49, pp. 2540–2545, 2007.

[181] E. H. Grant, V. E. R. McLean, N. R. V. Nightingale, R. J. Sheppard, and M. J. Chapman, "Dielectric behavior of water in biological solutions: Studies on myoglobin, human low-density lipoprotein, and polyvinylpyrrolidone," *Bioelectromagnetics*, vol. 7, pp. 151–152, 1986.

[182] O. Conde and J. L. Teixrira, "Hydrogen bond dynamics in water studied by depolarized rayleigh scattering," *J. Phys.*, vol. 44, pp. 525–529, 1983.

[183] E. H. Grant, B. G. R. Mitton, G. P. South, and R. J. Sheppard, "An investigation by dielectric methods of hydration in myoglobin solutions," *Biochem. J.*, vol. 139, pp. 375–380, 1974.